Non-Gaussian Analysis Of Diffusion-Weighted Magnetic Resonance Imaging

Inaugural-Dissertation

Zur Erlangung des Doktorgrades
der Mathematisch-Naturwissenschaftlichen Fakultät
der Heinrich-Heine-Universität Düsseldorf

vorgelegt von

MSc. Gael Nadege Pentang

aus Douala

Düsseldorf, den 23.01.2017.

aus dem Institut für Diagnostische und Interventionelle Radiologie
und dem Institut für Experimentalphysik
der Heinrich-Heine-Universität Düsseldorf

Gedruckt mit der Genehmigung der
Mathematisch-Naturwissenschaftlichen Fakultät der
Heinrich-Heine-Universität Düsseldorf

Referent:	Prof. Dr. rer. nat. Hans-Jörg Wittsack
Korreferent:	Prof. Dr. rer. nat. Axel Görlitz

Tag der mündlichen Prüfung:

Eidesstattliche Versicherung

"Ich versichere an Eides Statt, dass die Dissertation von mir selbständig und ohne unzulässige fremde Hilfe unter Beachtung der "Grundsätze zur Sicherung guter wissenschaftlicher Praxis an der Heinrich-Heine-Universität Düsseldorf" erstellt worden ist."

Acknowledgment

Magnetic resonance imaging is a fascinating research field and I am glad that I had the privilege to give my contribution to it as a PhD student at the institute of diagnostic and interventional radiology of the Heinrich-Heine University of Dusseldorf. Therefore, I thank all the people who made this dissertation possible and my post-graduate studies' experience a cherishable one.
First of all, I express my sincere gratitude to my supervisor Prof. Wittsack for the continuous support of my doctoral study and related research, for patience and motivation. His guidance helped me in all the time of research and writing of this thesis. I also thank Prof. Görlitz for assisting me as a mentor.
My sincere thanks also go to Prof. Antoch and Prof. Mödder, for giving me the opportunity to join their team and access to the laboratory and research facilities, and to Prof. Lanzman for interest and remarks on my work.

Thanks to my colleagues at the institute of diagnostic and interventional radiology of the Heinrich-Heine University of Dusseldorf for providing a wonderful atmosphere and to all my friends.

My deepest gratitude to my family and especially to my sister Christelle, and my brother, Armand, for support and encouragement with best wishes.

Finally, I thank my husband, Steve who has endured all my stressful days, who always cheered me up and helped me regain my confidence. I thank God for the privilege of being able to study and for creating an interesting world to research.

Abstract

Diffusion Tensor Imaging (DTI), as conventional extension of Diffusion-Weighted Imaging (DWI), is based on Magnetic Resonance Imaging (MRI). This technique renders *in vivo* information about biological tissue microstructure non-invasively according to the characteristics of water diffusion. With the novel approach of Diffusion Kurtosis Imaging (DKI), also referred to as non-Gaussian DWI, a more exact analysis of the diffusion characteristics in terms of probability distribution and their variation (Gaussian distribution, kurtosis) is possible. DKI can better model the water molecules movement and provide a better characterisation of tissue microstructure compared to DTI. The purpose of this thesis is the development and optimisation of image reconstruction pre-processing tools and the necessary imaging protocols for practical use of DKI in the clinical routine. Additionally, it aims to explore the additional value of DKI, as a newly introduced medical imaging technique, in characterising biological tissue microstructures in the healthy human brain and kidneys.

However, the practical use of DKI in the clinical routine is associated with some challenges: (a) An increased measurement time due to the higher number of measurements necessary to estimate the more complex non-Gaussian model that introduce motion artefacts and, (b) errors that derivate from fitting the low signal-to-noise ratio (SNR) of highly diffusion-weighted (DW) images. Therefore, the first part of this dissertation focusses on developing a robust motion correction method to align DW images prior to DKI computation. A basic concept of information theory called mutual information that better performs than conventional motion correction techniques based on grey values comparison is used as similarity measure. A jointly anisotropic linear minimum mean squared error (jaLMMSE) filter and a non-linear anisotropic diffusion filter (ADF) are implemented and compared, in order to improve the DKI results. Simulations with synthetic and real DKI brain data from healthy volunteers show that the mean structural similarity index (MSSIM) and the peak-signal-to-noise ratio (PSNR) are significantly lower with ADF compared to jaLMMSE. Furthermore, the resulting pre-processing methods for motion and noise correction are applied for neuroimaging and the variability of the diffusion kurtosis measures is evaluated in 80 healthy human brains. The resulting DKI metrics are mapped to the existing well-established anatomical Montreal Neurology Institute (MNI) space to construct the first age- and gender-dependent MRI whole human brain atlas. In the second part of this thesis, DKI is applied for the first time to healthy human kidneys using respiratory triggered acquisitions at 3T showing cortico-medullary differentiation in mean kurtosis images. In addition, experiments are performed to find optimal acquisition parameters (b-value = 0; 500; 1000 s/mm^2 and 20 diffusion directions) for renal DKI.

Kurzfassung

Diffusion Kurtosis-Bildgebung (DKI) dient als Erweiterung der Diffusions-Tensor-Bildgebung (DTI). Durch die exakte Analyse der Diffusionseigenschaften im Sinne von Wahrscheinlichkeitsverteilungen und deren Abweichungen (Gaußverteilung, Kurtosis) soll die Molekülbeweglichkeit mit DKI besser modelliert werden. Hierdurch können neuartige diagnostische Informationen aus den diffusionsgewichteten (DW) Untersuchungen gewonnen werden, die zu einer verbesserten Differenzierung von pathologischem Gewebe beitragen können. Das Ziel dieser Arbeit ist die Entwicklung und Optimierung der erforderlichen Bildvorverarbeitungstechniken und Bildgebungsprotokolle für die praktische Anwendung von DKI in der klinischen Routine. Zusätzlich soll das Potenzial von DKI, als neulich entwickelte Bildgebungstechnik, für die Charakterisierung von biologischer Gewebemikrostruktur im gesunden menschlichen Gehirn und in Nieren untersucht werden.

Die Ergebnisse dieser Arbeit zeigen neue Erkenntnisse für die Diffusionsgewichtete Bildgebung (DWI). Der erste Teil konzentriert sich auf die Entwicklung einer Technik zur Bewegungskorrektur von DW Bildern. Die Grundidee ist es, *Mutual Information* (MI) - ein grundlegendes Konzept aus der Informationstheorie - als Ähnlichkeitsmaß zu verwenden. Im Vergleich zur herkömmlichen Bewegungskorrekturtechniken, in denen die Grauwerte verglichen werden, erfordert MI keine Angabe über die Geometrie zwischen den beiden Bildern, und eignet sich gut als Kriterium zur Registrierung von Bildern mit unterschiedlichen Kontrasten wie DW Bilder. Zwei Rauschreduktionsverfahren werden zur Verbesserung der DKI-Ergebnisse implementiert und verglichen. Die Anwendung der entwickelten Vorverarbeitungstechniken auf Neuro-Bildgebung dient zur Untersuchung der Variabilität der Diffusionsergebnisse in 80 gesunden menschlichen Gehirnen. Die resultierenden DKI Werte abgebildet auf die gut etablierten anatomischen Montreal Neurologie Institute (MNI) Templates werden zur Erstellung menschlicher DKI-Atlanten des Gehirns in Abhängigkeit von Alter und Geschlecht benutzt.

Im zweiten Teil werden gesunde menschliche Niere zum ersten Mal mittels des Verfahrens DKI untersucht. Die Ergebnisse zeigen eine signifikante kortiko-medulläre Differenzierung in Kurtosis-Metriken. Anschließend wird DKI mit optimalen Aufhnahmeparametern (b = 0; 500; 1000 s/mm^2 und 20 Diffusionsrichtungen) in der menschnlichen Niere angewendet.

Parts of this work were published previously: the first section of Chapter 4 is an extension of [5]. Chapter 5 uses parts of [1] and [3]. Chapter 6 is based on [2] and [4].

Full articles

[1] Gael Pentang, Rotem Shlomo Lanzman, Philipp Heusch, Anja Müller-Lutz, Bernd Turowski, Gerald Antoch, Hans-Jörg Wittsack. *A brain atlas based on diffusion tensor (DTI) and diffusion kurtosis imaging (DKI).* Submitted for publication in Eur. J. Neurosci, 2016.

[2] Gael Pentang, Rotem Shlomo Lanzman, Philipp Heusch, Anja Müller-Lutz, Dirk Blondin, Gerald Antoch, Hans-Jörg Wittsack. *Diffusion Kurtosis Imaging of the Human Kidney: Feasibility Study.* Magn. Reson. Imaging 2014; 32: 413-420.

Conference proceedings

[3] Gael Pentang, René Bastkowski, Rotem Shlomo Lanzman, Philipp Heusch, Anja Müller-Lutz, Georg Öltzschner, Dirk Blondin, Gerald Antoch, Hans-Jörg Wittsack. *MR Whole Brain Atlas on the Basis of Diffusion Tensor and Diffusion Kurtosis Data at 3T.* European Society of Magnetic Resonance in Medicine and Biology (ESMRMB), Lisbon, Portugal; october 2012.

[4] Gael Pentang, Philipp Heusch, Rotem Shlomo Lanzman, Anja Müller-Lutz, Dirk Blondin, Gerald Antoch, Hans-Jörg Wittsack. *Diffusion Kurtosis Imaging of the Human Kidney.* European Society of Magnetic Resonance in Medicine and Biology(ESMRMB), Lisbon, Portugal; october 2012.

[5] Gael Pentang, Christian Mathys, Bernd Turowski, Gerald Antoch, Hans-Jörg Wittsack. *Evaluation of Mutual Information Based Motion Correction Techniques in DTI.* European Society of Magnetic Resonance in Medicine and Biology, Leipzig, Germany; october 2011.

Contents

Chapter 1

Introduction

1.1. Problem statement

Magnetic Resonance Imaging (MRI) is a non-invasive medical imaging technique that uses the magnetic properties of spinning hydrogen atoms to produce images. Compared to other imaging applications, its good spatial resolution and the excellent soft tissue contrast make it the method of choice for neurological and genitourinary examinations. Perhaps most importantly, because it does not rely on ionising radiation, MRI is safe for serial examinations, dynamic (time-resolved) imaging studies and screening in asymptomatic subjects [1]. Moreover, it allows for both 2-dimensional (2D) and 3-dimensional (3D) representations of the inner structure of the living human body.

In biological tissue, random and constant diffusion of water molecules is influenced by the interaction with the molecular, cellular and sub-cellular environment. This means that as a consequence of their diffusion movement, the water molecules probe the biological tissues on a microscopical scale well below the millimetre scale of conventional MRI images. Therefore, it is extremely important to notice that differences in microstructures within the tissue or changes in the micro-architecture of living tissues that appear after injury or pathology can be detected.

Clinical Diffusion-Weighted Magnetic Resonance Imaging (DWI or DW-MRI) focusses on the movement of water molecules. It measures the diffusion of water in the brain and kidney tissue that faces a complex and varied microstructure composed of multiple compartments. The diffusion of molecules that is free depending on the composition of the underlying environment can be hindered by a cell membrane or even systematically restricted when the molecule collides with an inner surface or at collision with macro-molecules.
For example in the brain, three types of diffusion processes can be observed. In the cerebrospinal fluid (CSF), diffusion tends to be free measured with a scalar coefficient of diffusion D that is almost identical to that of water. In the grey matter, D is isotropic but can be restricted in the presence of cell barriers. Finally, in the white matter where diffusion is anisotropic - oriented by the fibre nerves, diffusion is measured by a diffusion ellipsoid (a 3×3 tensor) based on the Diffusion Tensor Magnetic Resonance Imaging (DTI or DT-MRI) technique.

Despite the great benefits of DWI and DTI, their clinical application still faces a major challenge based on two assumptions with a limited validity. First, in DWI the simple underlying mathematical model assuming an overall isotropic diffusion displacement with a Gaussian distribution does not not hold for all the types of diffusion mentioned above. In fact, when higher

diffusion-weighting factors are used, the diffusion-weighted (DW) signal deviates significantly from the mono-exponential behaviour that is assumed with the Gaussian distribution in the DWI and DTI model. Secondly, DTI has a limited sensitivity as it assumes that each voxel contains a single directional diffusivity maximum. This is observed at very high weighting of the diffusion that increases the sensitivity of the water molecules signal to any heterogeneous diffusion distances that might be present in complex micro-architectures [2]. As a result, the DWI model fails to provide an accurate quantification of the true diffusion process. There are several models to characterise more complex tissue micro-structural changes in diffusion MRI. They vary from the easiest and commonly used techniques - that map apparent diffusion coefficient values - to the more complex methods based on the q-space theory [3, 4, 5].

1.2. Research Goals and Approach

This thesis builds up on a novel method that extends conventional DWI / DTI using a non-Gaussian analysis of the DW signal - the kurtosis model [6]. This new method is more effective because it does not rely on limited assumptions (multi-compartment techniques) such as other methods initially published [7, 8] and is easily applicable for clinical studies on current MR scanners [9].
DKI improves the DWI signal because it considers both the Gaussian and the non-Gaussian components of the diffusion process. This is achieved by the so-called kurtosis parameter K, that measures the deviation of the probability distribution from a Gaussian process. At the time of writing this thesis, only very few articles have been published on the use of DKI. They demonstrate the superiority of DKI over DWI in the characterisation of the microscopic structure of the healthy [9, 10] as well as the pathological [11, 12] biological tissue. In addition, since current studies have focussed more on the brain micro-architecture, it is relevant to use DKI to explore other human organs.

DKI requires the use of more than one diffusion-weighting strength and a higher number of diffusion-weighting directions compared to DTI. This lengthens the scan time and makes the DKI acquisitions more prone to motion artefacts. In addition, the resulting DW images have a very low signal-to-noise ratio (SNR) due to the necessary stronger diffusion-weighting. Thus, the first aims of this dissertation were to study how motion affects DW-derived parameters and to develop a robust image registration routine prior to DKI signal fitting. State-of-the art noise reduction techniques were also examined for diffusion-weighted image filtering prior to diffusional kurtosis estimation. Then DKI was applied to normal human brains to see if additional relevant information can be extracted from DKI compared to the widely-used DWI and DTI methods regarding age and gender related changes. Besides the brain applications, DKI was also applied to healthy human kidneys. First, the feasibility of renal DKI was investigated. Then the acquisition parameters were optimised in terms of range and number of b-values as well as number of diffusion directions used for the calculation of robust and reliable kurtosis maps in the kidneys. The methodologies developed here are designed to facilitate the clinical application of DKI and of course, to achieve reliable and more stable kurtosis maps in feasible acquisition times.

1.3. Thesis Outline

This thesis is organised in four parts: the state-of-the art, the methodological contribution, the clinical contribution and a conclusion part.

The **State of the art part** (Chapters 2 - 3) describes the anatomy of the human brain and kidneys in Chapter 2. Chapter 3 introduces the mathematical models and parameters used to measure water diffusivity for non-invasive imaging of biological tissue microstructure. It also reviews the challenges with artefacts in DWI and highlights the clinical value of DWI in the human brain and kidneys. The **Methodological contribution part** in chapter 4 describes the theoretical and methodological contributions of the thesis. It analyses how image motion and noise affect the accuracy and variability of DKI derived parameters. Here the experiments are carried out on both simulated and real image data of the brain and robust motion and noise correction procedures for non-Gaussian DW images are established. Details of the architecture of a whole processing pipeline designed for calculation of the diffusion kurtosis maps are given. The **Clinical contribution part** (Chapters 5 - 7) highlights the contributions for specifics neurological and genitourinary applications. Chapter 5 focusses on the construction of an age- and gender-related human brain atlas based on DTI and DKI measures of healthy volunteers. The resulting atlases may serve in the future as reference values for comparison with changes associated with development, aging and pathologies. Chapter 6 answers the question of which additional information is revealed by DKI on the cortico-medullary differentiation in healthy human kidneys. Chapter 7 investigates the influence of the choice of number and range of b-values together with the number of diffusion directions on DKI maps in healthy human kidneys. Here the acquisition parameters are optimised for reliable and more stable renal DKI parameters in clinically feasible acquisition time. Finally, the **Conclusion** in chapter 8 summarises the main findings of this dissertation and proposes future directions.

Chapter 2

The human brain and kidneys

In this thesis, the analysed and developed methods were applied to the human brain (see Chapters 4 and 5) and kidneys (see Chapters 6 and 7) to understand their underlying tissue microstructure. Therefore, the aim of this chapter is to present the basic concepts of cerebral and renal anatomy necessary for the understanding of this work. In general, this background chapter is inspired from reviews, articles, books and thesis chapters [13, 14, 15, 16, 17, 18, 19] that give a good structured overview of the cerebral and renal anatomy.

2.1. Cerebral anatomy

In the human body, the nervous system is a complex system [13] that controls all the functions of the organism. It consists of the central nervous system (CNS) with the brain and the spinal cord which is responsible for receiving, integrating and transmitting information [16] and the peripheral nervous system (PNS) that contains the spinal and the cranial nerves which is responsible for transmitting this information from the CNS to the dedicated organs [16].

2.1.1. Macroscopic architecture

The human adult brain is well-known to weigh approximately 1.3 - 1.5 kg with a volume of 1100 cm^3 in females and 1400 cm^3 in males [19].

At the structural level, the major structures of the brain reported in the literature are:

- the cerebrum that represents the biggest part of the brain and is divided into two hemispheres linked by the corpus callosum [16].
- the cerebellum also referred to as "little brain" positioned under the cerebrum and composed of grey and white matter (more details about these tissues are given in the next sections).
- the brainstem that is the connecting structure between the cerebrum, the cerebellum and the spinal cord [16].

The three main tissue classes present in the brain are: the cerebrospinal fluid (CSF), the grey matter (GM) and the white matter (WM). This classification is important because each of these tissues has a different contrast on MRI images. At the cerebrum surface, with its folded

appearance, the tissue class found there is often referred to as cortex. The cortex contains millions of nerve cells whose cell bodies colour is responsible for its dark grey-brown appearance, explaining the name grey matter attributed to it [16]. Under the cortex, long fibres called axons connects the neurons to each other and constitute the white matter. The white matter is the main component of the CNS and contains myelinated as well as non-myelinated axons. The name "white" is associated with the lighter colour of the axons related to the myelin sheath [16]. With the folded structure of the cortex, many neurons can fit in the skull; a bony structure that protects the brain against injuries. In the brain, the cerebrospinal fluid (CSF) is a colourless substance that is present within empty cavities of the brain, around the brain and spinal cord. The CSF circulates and is constantly being produced and reabsorbed and also helps to protect the brain from injuries [16].

2.1.2. Microscopic architecture

At the cellular level, two types of cells can be found in the brain: the nerve cells (often called neurons) and the glia cells.

Although the size and the shapes of the neurons are often different, their structure is almost the same. A neuron is composed of a cell body, dendrites and an axon [16]. Neurons receive and transmit information. Axons are often referred to as nerve fibres and many axons together form a fibre tract. The size of an axon is generally between 0.2 μm and 10 μm. Axons with a diameter greater than 10 μm are packed in an electric insulin layer called a myelin sheath. Myelinated axons are faster in information transmission compared to non-myelinated axons [16]. The glia cells nourish, protect and support the nerve cells and are 10 to 50 times more abundant in the brain than neurons [16]. The glia cells are the nerve type that is mostly involved in brain tumours. There are various types of glia cells in the CNS: astroglia or astrocytes, oligodendroglia cells or oligodendrocytes, ependymal cells also called ependymocytes and microglia cells.

2.2. Renal anatomy

The kidneys are a pair of bean-shaped organs found in the human body. Each kidney has a concave surface called renal hilum, where the renal vein, nerve and artery enter and exit the kidney, and a convex surface. The kidneys are located in the posterior part of the abdomen meaning they are positioned retro-peritoneal [17]. Although each kidney is generally 4 cm thick, 6 cm wide and about 11 - 14 cm long, a female kidney (115 - 155 g) weighs less than a male kidney (125 - 175 g) [17]. In its primary function, the kidney filters blood in such a way that the whole blood inside our body goes through the kidneys several times within a day.

The kidney itself is enveloped with tree layers of tissue. The outer layer is called renal fascia *of Gerota* and it has a fibrous structure. As middle layer, follows the adipose capsule - *perinephric fat* and the inner layer called renal capsule also has a fibrous structure.

2.2.1. Structural architecture

In the coronal view of the kidney, one can distinguish between the cortex region and the medulla region. These two parts of the kidney are linked through a fibrous area: the renal column to the renal papillae and the renal pyramids. The renal papillae is a stack of nerves that is responsible to transfer the urine produced by the nephrons of the renal pelvis to the calyces of the kidneys for evacuation. The renal column is not only a connective structure, but it allows through its

subdivision in 6 to 8 lobes an interface to penetrate and exit the cortical region. A kidney lobe consists of of some renal pyramids and the renal column.

2.2.2. Cellular architecture

At the microscopic level in a kidney, the nephrons are the most important units of function as they are responsible of the urine production. About 1 million nephrons are present in each kidney and each nephron is made of a corpuscle and a tubule.

While the nephrons are responsible for urine production, the blood filtering takes place in the renal corpuscle. In the corpuscle, the capillaries of the glomerulus are surrounded by the glomerular capsule (also called the Bowman's capsule).

Chapter 3

Diffusion-Weighted-Imaging (DWI)

This chapter reviews the basics of Magnetic Resonance Imaging (MRI) and Diffusion-Weighted MRI (DWI), introduces the artefacts associated to the application of diffusion MRI and give details on the clinical application of DWI in the human brain and kidneys. For a more detailed review, one may refer to Johansen and Berg [20].

3.1. Conventional Magnetic Resonance Imaging (MRI)

MRI[1] is a non-invasive medical imaging technique to visualise the structure of biological tissues *in vivo*. It provides excellent soft tissue contrast with high resolution without ionising radiation. In clinical MRI, the nuclei of hydrogen atoms (^{1}H) is the most frequently imaged nucleus because of its great abundance in biological tissues [21]. About 60 % of the adult human body weight consists of water [18]. ^{1}H produces the strongest Magnetic Resonance Imaging signal compared to other nuclei as ^{13}C, ^{19}F, ^{31}P and ^{23}Na that are also used in MRI.

A typical MRI experiment starts with the exposition of the patient to a strong static magnetic field B_0 in the MR scanner. The spins within the patient's body tend to align in a direction either parallel or anti-parallel to the B_0 field and start to precess at the Lamor frequency that is proportional to the B_0 field and is given by the Lamor equation [20]:

$$\omega = \gamma B_0 \tag{3.1}$$

where ω is the precession frequency in MHz, B_0 is the magnetic field in Tesla and γ is the gyromagnetic ratio in MHz/T - a constant specific to the nuclei that is being examined. In case of water, the hydrogen nucleus has a gyromagnetic ratio $\frac{\gamma}{2\pi}$ of 42,58 MHz/T or $\gamma = 2.68 \times 10^8$ rad/s/T. With the application of a 90 $^\circ$ radio frequency (RF) pulse using a magnetic coil, the net magnetisation vector is projected to the transverse plane (see figure 3.1a). The spins that were initially coherent after the 90 $^\circ$ RF pulse excitation begin to dephase due to magnetic field inhomogeneities [20] (see figure 3.1b). Considering the spin echo pulse sequence based on the works of Edwin Hahn in 1952 and Carr and Purcell in 1954, the dephasing due to the inhomogeneities of the magnetic field are reversible through a 180 $^\circ$ RF pulse (see figure 3.1c, d) to reproduce the signal . The echo time (TE) is used to denote the time elapsed after the first

[1] also MR, or MRT *Magnetic Resonance Tomography*.

3. *Diffusion-Weighted-Imaging (DWI)*

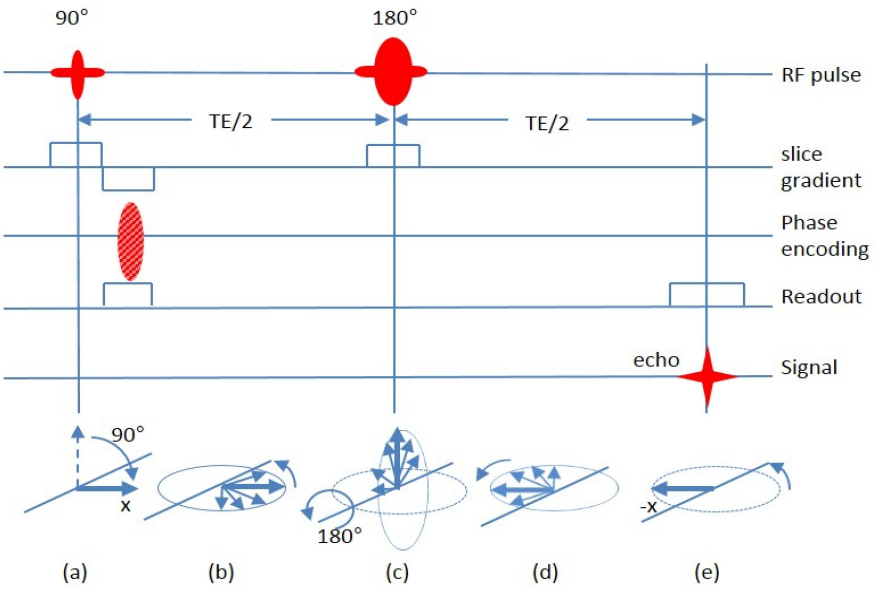

Figure 3.1.: Spin echo pulse diagram for Magnetic Resonance Imaging (MRI). Image acquisition with illustrated phase evolution at different stages. (a) excitation ($t = 0$); (b) dephasing; (c) refocussing ($t = \mathrm{TE}/2$); (d) rephasing and (e) echo ($t = \mathrm{TE}$). Figure is adapted from Laun et al., 2011 [22].

RF pulse is produced until generation of the echo (see figure 3.1e).
To get an MRI image, three field gradients are used as shown on figure 3.1: one for slice selection,

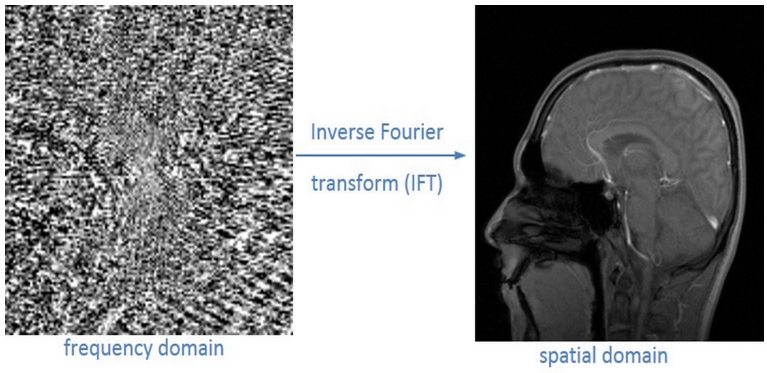

Figure 3.2.: Acquired images in the frequency domain are converted to the spatial domain by inverse Fourier Transform (IFT).

one for frequency coding and one for phase encoding. Thus, an image is acquired in the frequency domain (or Fourier domain). After inverse Fourier transform (FT), the MRI image is obtained as a 3D matrix which relates each point in space, called voxel, to an intensity (see figure 3.2).
In conventional MRI, the structural image contrast observed can be a function of the tissue density (proton-weighted image) or the tissue relaxation properties (T_1- and T_2-weighted images) depending on the acquisition parameters. Additionally to structural details, unconventional MRI techniques provide other types of information that are metabolic, functional or micro-structural. From the various MRI techniques developed in the last twenty years, DWI stands out because of its remarkable contribution in understanding many neurological and nephrological disorders

and abnormalities including stroke, multiple sclerosis, tumours, stenosis [23, 24, 25, 26, 27, 28]. In DWI, one does not concentrate on the movement of spins as in conventional MRI, but the focus is laid on the movement of water molecules in biological tissues to weigh the image by the diffusion process of the hydrogen micro-particles.

3.2. Diffusion-Weighted-Imaging (DWI)

3.2.1. Brownian motion and diffusion

Understanding the basic principle behind the DWI technique requires to have an insight into the details of the diffusion process. In the literature, the term diffusion is used to describe the random movement of molecules or microscopic particles from areas with high to areas with low concentrations [20, 29]. This is a natural process that originates from the random thermal motion, also called Brownian motion and is different from the convection or dispersion that rather results from bulk motion. The bulk motion has a predetermined direction, while in diffusion the directions of motion are randomly distributed and incoherent.
First attempts to establish the physical law behind the diffusion process resulted in the expression of the diffusive flux J also known as Fick's law [30]:

$$J = -D\nabla C. \tag{3.2}$$

Here C is the concentration gradient of the particle and D is the diffusion coefficient. Assuming that there is no diffusive flux when the temperature and particle concentration remain stable as at equilibrium, the Fick's law was contradictory to results published in 1828 by the botanist Robert Brown [31] who had demonstrated that particles move arbitrarily without any apparent cause. The relationship between the Fickian and the Brownian hypotheses is established with the introduction of the Einstein equation for diffusion (see Equation (3.3)) [20, 29, 22]. Using a probabilistic scheme based on a displacement distribution to quantify the number of molecules that will travel a certain distance within a particular time frame, the mean-squared displacement of the molecules, characterising its Brownian motion is related to the diffusion coefficient, D, present in the Fick's law by [32]:

$$\left\langle x^2 \right\rangle = 2Dt. \tag{3.3}$$

Here $\left\langle x^2 \right\rangle$ stands for the mean-squared displacement of particles during a diffusion time, t, and D is the diffusion coefficient introduced in the Fick's law.
It is well-known that the diffusion coefficient D is specific to the material under examination and that its value depends on the size of the molecules that diffuse, and the temperature and the microstructural features of the environment [20]. Taking advantage of the knowledge about this sensitivity and continuous random walk of water molecules in the human body, measures of the diffusion coefficient are used today in clinical MRI to probe the physical properties of biological tissues. In other words, through the diffusion movement, the water molecules probe the biological tissues at a microscopic scale well below the usual millimetre scale of conventional MR images.

3.2.2. Relating the diffusion process to MRI to obtain the DWI signal

The spin echo pulse diagram as described above in section 3.1 can be used to produce images in conventional MRI, but is not adequate to measure the diffusion movement of hydrogen

particles that occurs at microscopic scales. In the currently used pulse field gradient spin echo sequence (PGSE) based on the suggestions of Stejskal and Tanner in 1965 [33], two gradient pulses called diffusion-weighting gradients, produced by the magnetic gradient coils, are introduced before and after the refocussing pulse as illustrated on figure 3.3. During the diffusion gradient

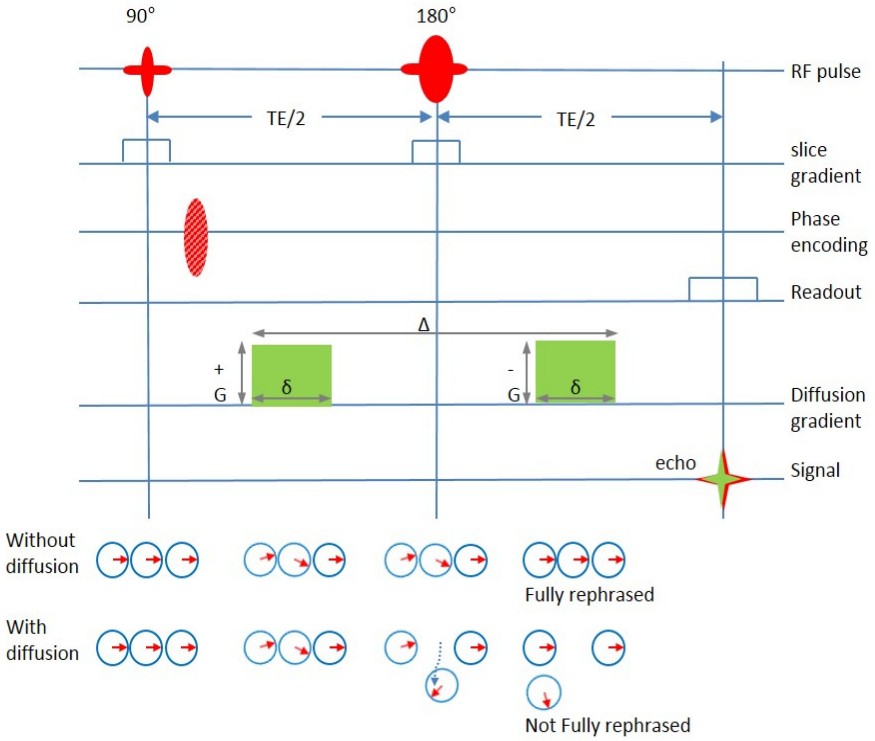

Figure 3.3.: A schematic representation of the pulse field gradient spin echo (PGSE) sequence of Stejskal and Tanner [33]. Δ is the time between the application of the two gradient pulses, δ is the gradient pulse duration and G is the strength of the gradient applied. Figure is adapted from Laun et al., 2011 [22].

application, a particle at position x encounters a magnetic field $B_0 + G\ x(t)$ at time t, where G is the magnitude of the gradient pulse. Depending on whether the particle spends a short time at this position or not, a phase shift can occur. This phase shift is given by $\phi_1 = -qx_1$ and $\phi_2 = -qx_2$ assuming that x_1 and x_2 are the particle's position respectively after applying the first and the second gradient pulse with $q = \gamma\delta G$, where δ is the duration of the gradient pulse. The 180 ° RF pulse applied in-between the two gradient pulses reverses the phase change that happened prior to it. In this way, the phase of the particles that were stationary are cancelled and only the particles that diffused are not completely refocussed. This phase change is given by $\phi_2 - \phi_1 = -q(x_2 - x_1)$.

During the DWI image acquisition, following steps are necessary in order to obtain the diffusion coefficients. A minimum of two signal measurements are required: one in the absence of any gradients, $S(0) = S_0$ and another one that is weighted by diffusion called $S(q)$ acquired along the 3 orthogonal axes (x, y and z) of the scanner. Next, the effect of the relaxation on the MRI signal attenuation is cancelled by dividing the DW signal $S(q)$ by the signal S_0 in absence of any gradients.

According to the Einstein's equation [20]:

$$E(q) = \frac{S(q)}{S_0} = \int \rho(x_1) \int p(x_1, x_2, t) e^{-iq(x_2 - x_1)} dx_2 dx_1 \tag{3.4}$$

with

$$p(x_1|x_2, t) = \frac{1}{\sqrt{4\pi D t}} \exp(-\frac{(x_2 - x_1)^2}{4Dt}), \tag{3.5}$$

where $\rho(x_1)$ is the spin density when the first gradient is applied. It stands for the likelihood of finding a spin at location x_1. $p(x_1, x_2, t)$ is the diffusion propagator whose second moment is the Einstein equation introduced in section 3.2.1. It is the probability that a particle initially at position x_1 diffuses after time t (the time elapsed between the application of the two gradients) to a position x_2. Details about the derivation of the diffusion propagator and its relationship to the Einstein's equation can be found in the book of Derek [29].

Referring to the Stejskal-Tanner relation, $E(q)$ can be rewritten in case of a free diffusion, where the diffusion propagator is Gaussian as [20]:

$$E(q) = e^{-q^2 D(\Delta - \delta/3)} \tag{3.6}$$

$$\frac{S(b)}{S_0} = e^{-bD}, \tag{3.7}$$

where the b-value

$$b = q^2(\Delta - \delta/3) = \gamma^2 \delta^2 G^2 (\Delta - \delta/3) \tag{3.8}$$

indicates how strong the signal is weighted by diffusion [20]. γ is the gyromagnetic ratio, δ is the duration of the gradient application, Δ is the time interval between the application of the two gradient pulses and G is the gradient strength. A higher b-value (strong weighting) leads to a more attenuated signal.
Since the interpretation of the resultant signal attenuated DW images is not intuitive, the diffusion coefficients D are often fitted from equation (3.7). D is calculated for each direction of a voxel and stored in a map as apparent diffusion coefficients (ADC) (see figure 3.4). The ADC values correspond to the averaged diffusion coefficients for each voxel over the (x, y, and z)-directions that can be displayed on an ADC map.

$$ADC = (D_x + D_y + D_z)/3 \tag{3.9}$$

For the sake of simplicity, ADC is often referred to as D in the literature. This convention is also used in the following sections.

If diffusion is free without restriction, the diffusion propagator follows a Gaussian distribution as reported by Le Bihan et al. [7] and the MR signal is given by equation (3.7). Although chemists and physicists have been probing molecular diffusion using Nuclear Magnetic Resonance (NMR) since the eighties [7], the first *in vivo* diffusion imaging studies were published only in the nineties by Moseley et al. [23]. While they could highlight the numerous useful applications of clinical DWI, they also noticed the strong contrast difference in ADC images measured along different axes (x, y, z) [27, 34]. They attributed these differences to the presence of water molecules moving along axonal fibres. If the diffusion is not always isotropic as in equation (3.7), but can be directed along fibres, then a scalar measure of the diffusion coefficient is not adequate to fully describe the diffusion process in biological tissues. The diffusion propagator can no more be assumed to follow

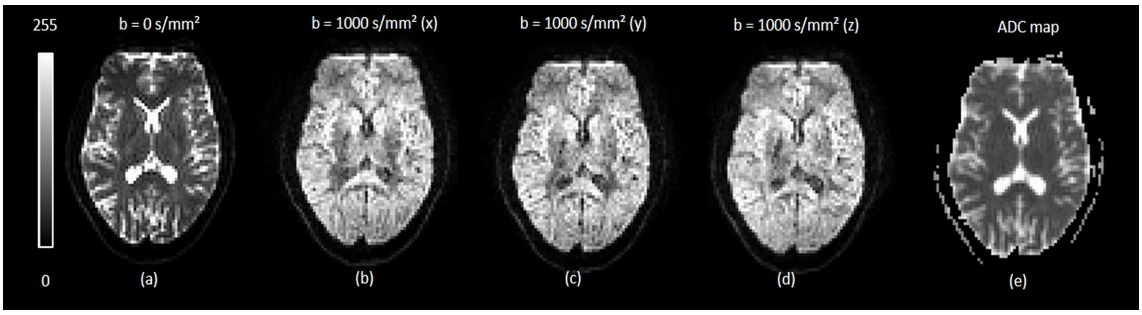

Figure 3.4.: Diffusion-weighted images at b-value = 0 (a) and b-value = 1000 s/mm^2 in x- (b), y- (c) and z-direction(d) together with the resulting ADC map. The DW images show high intensity in regions of slow diffusion (low ADC values) and low intensity in regions of fast diffusion (high ADC values).

a Gaussian distribution. This problem was already addressed in previous works and a summary of the solutions proposed are discussed in sections 3.3 and 3.4.

3.3. Diffusion Tensor Imaging (DTI)

Considering the microstructure of a biological tissue with the presence macromolecules, cells and oriented structures such as nerve fibres [13, 16], the diffusion trajectory of water molecules without restriction can happen, but it is rarely the case. Therefore, the shape of the diffusion distribution that is more spherical when water moves freely becomes more oval pointing to the direction of the oriented structure. In this case, using a scalar measure as the diffusion coefficient fails to fully characterise both the isotropic and the anisotropic diffusion. A solution to this problem is to use a new MRI imaging technique called Diffusion Tensor Imaging (DTI) [35].

3.3.1. Diffusion tensor

In DTI, instead of using a single diffusion coefficient, different diffusion coefficients along different directions are considered to describe the diffusion (see figure 3.5). To determine the shape and orientation of the diffusion ellipsoid, a second-order tensor called diffusion tensor denoted by $\mathbf{D_T}$ is calculated. Here the sub-index $\mathbf{_T}$ emphasises the fact that the diffusion is represented by a tensor. $\mathbf{D_T}$ is a 3×3 symmetric matrix ($D_{ij} = D_{ji}$, with $i, j = x, y, z$) that describes the 3D shape of the diffusion [35].

$$D_T = \begin{bmatrix} D_{xx} & D_{xy} & D_{xz} \\ D_{yx} & D_{yy} & D_{yz} \\ D_{zx} & D_{zy} & D_{zz} \end{bmatrix}. \tag{3.10}$$

In the $\mathbf{D_T}$ matrix, the diagonal elements D_{xx}, D_{yy}, D_{zz} represent the diffusion coefficient at the three orthogonal logical axes of the scanner and the off-diagonal elements $D_{xy}, D_{xz}, D_{yx}, D_{yz}, D_{zx}, D_{zy}$ represent the correlation between diffusion along these three orthogonal axes. Since $\mathbf{D_T}$ is a symmetric matrix, it has only 6 independent elements because the elements above the diagonal are equal to those under the diagonal. For isotropic diffusion, the ellipsoid in figure 3.5 is a sphere and the diffusion coefficients D are equal in all the directions. In the anisotropic diffusion case, the direction of highest diffusion is moedelled with an elongated ellipsoid.
To calculate the eigenvectors ($\mathbf{v}_1$, $\mathbf{v}_2$, $\mathbf{v}_3$) and eigenvalues ($\lambda_1, \lambda_2, \lambda_3$), $\mathbf{D_T}$ is diagonalised as

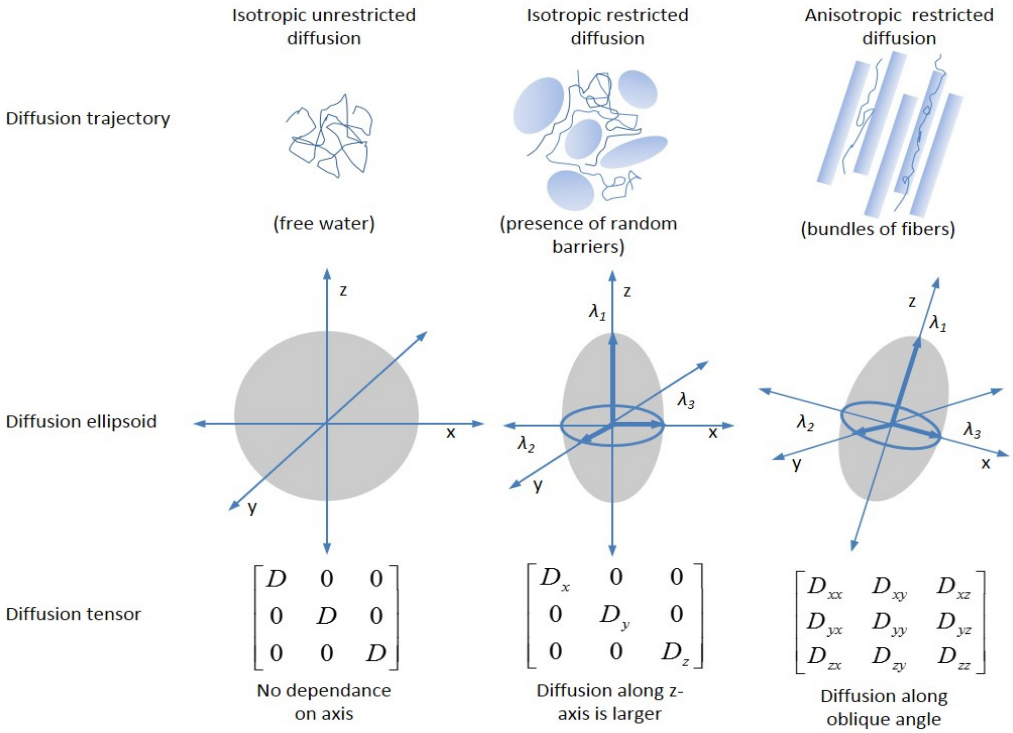

Figure 3.5.: Here the diffusion trajectory, the diffusion ellipsoid and the diffusion tensor are illustrated in cases of isotropic non restricted (1st column), isotropic restricted (2nd column) and anisotropic restricted diffusion (3rd column).

described below:

$$D_T = \begin{bmatrix} D_{xx} & D_{xy} & D_{xz} \\ D_{xy} & D_{yy} & D_{yz} \\ D_{xz} & D_{yz} & D_{zz} \end{bmatrix} \overset{\text{diagonalisation}}{\rightarrow} \begin{bmatrix} \lambda_1 & 0 & 0 \\ 0 & \lambda_2 & 0 \\ 0 & 0 & \lambda_3 \end{bmatrix} \cdot \begin{bmatrix} \mathbf{v}_1 & \mathbf{v}_2 & \mathbf{v}_3 \end{bmatrix}. \tag{3.11}$$

The eigenvalues are usually selected so that λ_1 points to the direction of highest diffusion and λ_2 and λ_3 are the radial diffusivities with $\lambda_1 > \lambda_2 > \lambda_3$. Finally, the DTI model is related to the DWI model of equation (3.7) as follows [35]:

$$S(b) = S_0 e^{-\sum_{i,j} b_{ij} Dij}, \tag{3.12}$$

where i, j are the directions of diffusion and b_{ij} are the elements of the b-matrix. Note that the b-matrix replaces the b-value.

To determine the 6 independent elements of the diffusion tensor, 7 signal acquisitions of an image are required: One with b = 0 s/mm^2 and a minimum of 6 additional DW images ($b \neq$ 0 s/mm^2) in 6 non-collinear diffusion encoding directions. But today in clinical research, the number of diffusion directions used is often higher. This issue will be discussed in the next sections. Equation (3.12) therefore corresponds to a system of 6 equations that can be solved via the least squares method at each voxel. An example of a DTI human brain acquisition with b = 0 s/mm^2 and b = 1000 s/mm^2 considering 6 diffusion directions is shown on figure 3.6. Different signal encoding directions show different diffusion patterns.

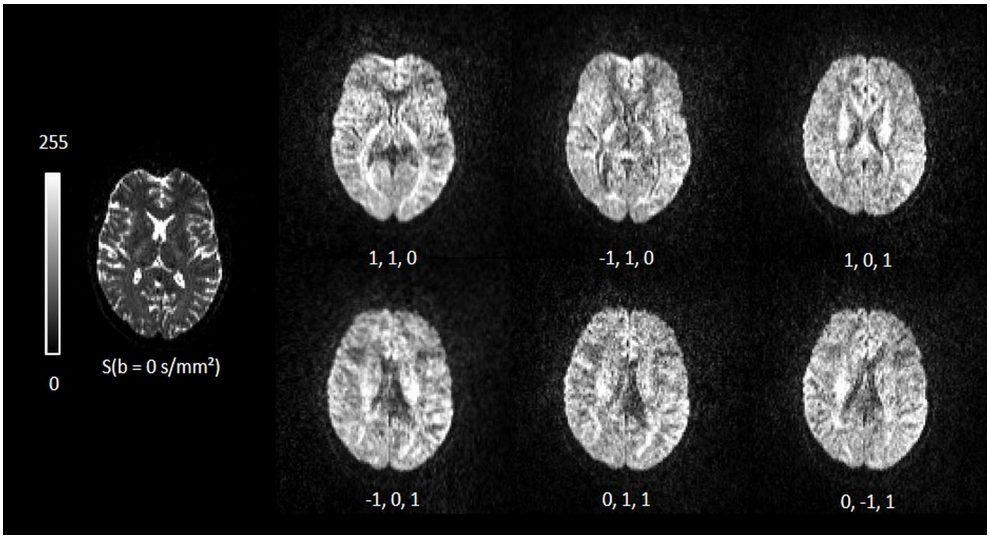

Figure 3.6.: Measured non diffusion-weighted image b= 0 s/mm^2 with six diffusion-weighted images (b= 1000 s/mm^2) in 6 non-collinear directions (DTI requires a minimum of 6 directions). Due to anisotropic diffusion, the resulting pattern differs with the considered direction.

3.3.2. Quantitative parameters derived from DTI

Although the diffusion tensor can fully characterise the diffusion pattern in biological tissue taking the orientation in consideration, it cannot be visualised easily. There exist a number of rotationally invariant diffusion metrics computed from the $\mathbf{D_T}$ in the literature [20] as presented below.

- Trace is the averaged diffusion that is expressed as sum of the eigenvalues or the diagonal elements of $\mathbf{D_T}$. It does not contain any information about the orientation of the water diffusion.

$$\text{Trace} = \lambda_1 + \lambda_2 + \lambda_3 = D_{xx} + D_{yy} + D_{zz}. \tag{3.13}$$

- Mean diffusivity (MD) characterises the average diffusivity as trace measurement divided by 3.

$$\text{MD} = \frac{\lambda_1 + \lambda_2 + \lambda_3}{3}. \tag{3.14}$$

- Fractional anisotropy (FA) is one of the most used metric in clinical DWI. It indicates how anisotropic the diffusion is. FA values always range between 0 (for isotropic water movement, $\lambda_1 = \lambda_2 = \lambda_3$) and 1 (to indicate that there is a preferred direction of diffusion, $\lambda_1 >> \lambda_2 \approx \lambda_3$). FA can be expressed as:

$$\text{FA} = \sqrt{\frac{3}{2}} \frac{\sqrt{(\lambda_1 - \text{MD})^2 + (\lambda_2 - \text{MD})^2 + (\lambda_3 - \text{MD})^2)}}{\sqrt{\lambda_1^2 + \lambda_2^2 + \lambda_3^2}}, \tag{3.15}$$

or

$$\text{FA} = \sqrt{\frac{1}{2}} \frac{\sqrt{(\lambda_1 - \lambda_2)^2 + (\lambda_2 - \lambda_3)^2 + (\lambda_3 - \lambda_1)^2)}}{\sqrt{\lambda_1^2 + \lambda_2^2 + \lambda_3^2}}. \tag{3.16}$$

- Axial diffusivity (D_{AX}) is the diffusivity measured along the direction of highest diffusion.

$$D_{AX} = \lambda_1. \tag{3.17}$$

- Radial diffusivity (D_{RAD}) is the measure of the mean directional diffusivity perpendicular to the direction of highest diffusion.

$$D_{RAD} = \frac{\lambda_2 + \lambda_3}{2}. \tag{3.18}$$

3.3.3. Coloured derived DTI

An additional type of image that can be derived from DTI is the so-called coloured fractional anisotropy (coloured-FA). Such an image uses a mapping of colours to represent the orientation of eigenvectors fields. Conventionally, red stands for left to right, green is for anterior to posterior, and blue is for superior to inferior. An example of a coloured-FA map is shown on figure 3.7 for the coronal (a), sagittal (b) and axial view (c).

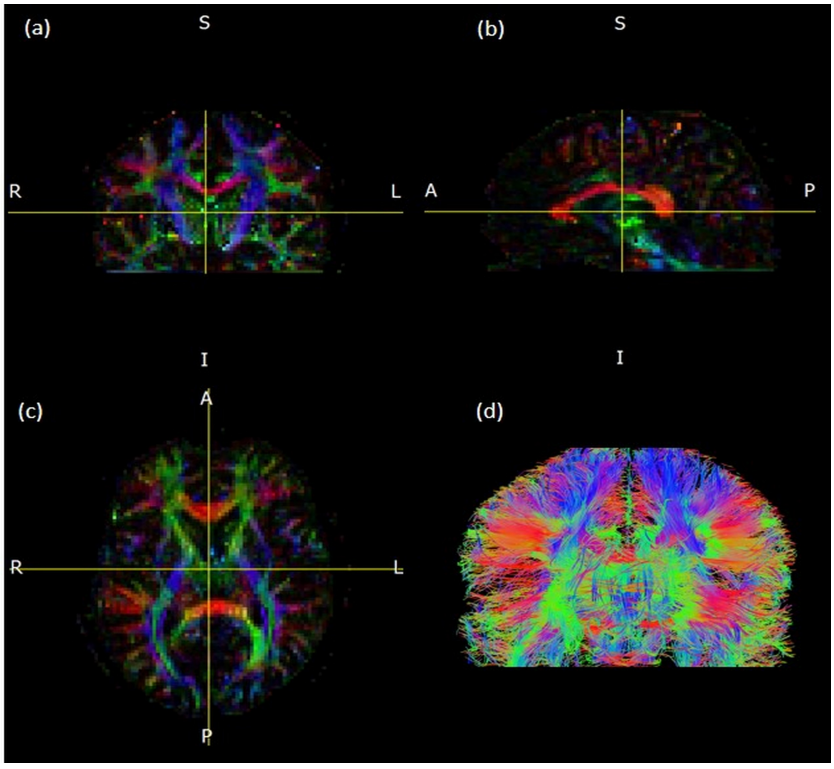

Figure 3.7.: FA-coloured maps: coronal (a), sagittal (b), axial (c). Red stands for left to right, green is for anterior to posterior, and blue is for superior to inferior. Resulting whole brain DTI visualisation in a tractography image (d).

3.3.4. Tractography

This is a technique that is used in DTI to estimate the trajectory of the fibre tracts using tensor information. Tractography results (see figure 3.7 (d)) can support the visualisation of various neurological pathologies [36, 37]. There exist different fibre propagation algorithms (for example

interpolated streamlines, fibre assignment per continuous tracking, 2nd-order Runge Kutta, and tensorline) for DTI in the literature [38].

3.4. Mathematical modelling of the DWI signal - Non-Gaussian behaviour of water diffusion

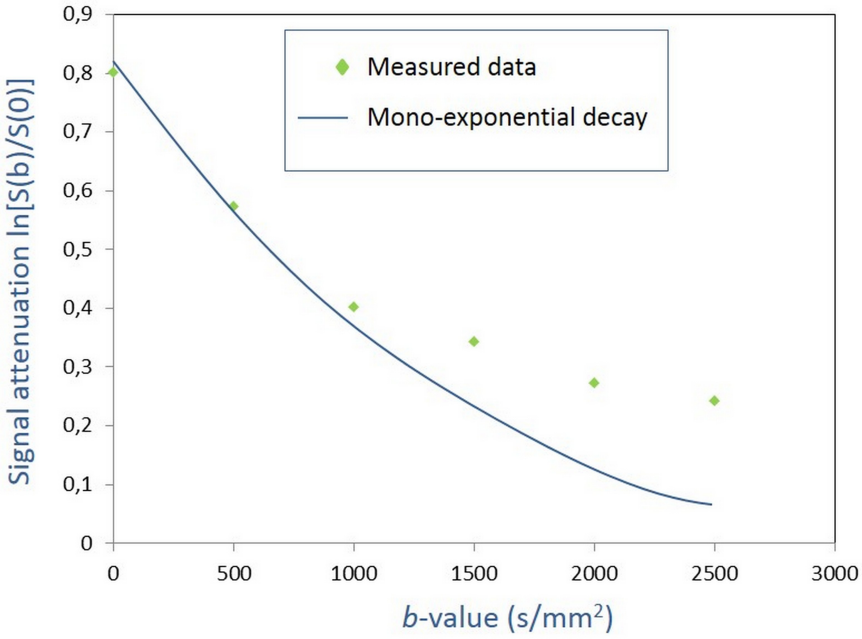

Figure 3.8.: Measured diffusion-weighted signal attenuation $S(b)/S(0)$ (green points) at b-values ranging from 0 to 2500 s/mm^2.

Although DTI takes the diffusion orientation in consideration and consequently improves the equation (3.7), the assumption that the DWI signal decay is a mono-exponential process is invalid. Water molecules can be restricted in their movement and the typical ranges of cell structures that lie in the μm-size cannot be visualised in DTI that works at resolutions of $2 \times 2 \times 2$ mm^3 [39]. In DTI, water molecules that diffuse over long distances dominate the measurement of diffusion at shorter distances making the DWI signal insensible at microscopic scales [2]. The displacement distribution is a non-Gaussian process. At high diffusion-weighting with b-values greater than 1000 s/mm^2, higher models of diffusion imaging can be used to provide a better characterisation of the biological tissue microstructure than DWI and DTI [40, 41]. This is obvious in the DWI signal attenuation $S(b)/S(0)$ (green points) that are illustrated on figure 3.8. The mono-exponential decay (blue line) deviation can be observed for b-values beyond 1000 s/mm^2.
A number of models to analyse the non-Gaussian behaviour of diffusion resulting from increasingly complex acquisitions techniques are briefly introduced in the next sections and classified according to the nature of the model. For a more complete state-of-the art review, please refer to the thesis of Maxime Descoteaux [14].

3.4.1. Models based on the mapping of apparent diffusion coefficients

In addition to the diffusion tensor representation introduced in section 3.3, a more complex modelling of the ADC can be performed under different assumptions. Here we concentrate on two different models that result from two assumptions: the multi compartment models and the generalised DTI models.

3.4.1.1. Multi compartment models

These models assume that many compartments contribute to the diffusion process. For example in the bi-exponential model developed by Le Bihan et al. [7], the author assumes that additionally to the pure molecular diffusion of water, another process that contributes to the DWI signal is the micro circulation of blood in the capillaries (called perfusion). He models the DWI signal decay as follows:

$$S(b) = S_0 \left(f e^{(-bD_p)} + (1-f)\, e^{(-bD_d)} \right). \tag{3.19}$$

The subset $_p$ is for pseudo diffusion influenced by perfusion and $_d$ is the pure diffusion. Here f is the incoherent flowing blood that increases when the contribution of perfusion to the diffusion signal is high. f tends to be zero in case of pure diffusion.
Although the method could be used successfully to measure the DWI signal decay in the human and rat brain [42], as reported by Minati et al. [43], values of $f \approx 2$ were found incompatible with the anatomy where $f \approx 8$. The multi-exponential decay of DWI signal was already demonstrated in an isolated compartment [44]. Other relevant reports on models with more than two compartments contributing to the diffusion process were published by [3] and [4].

3.4.1.2. Generalised DTI models

This multi-tensor model simply generalises the DTI model (see section 3.3). It replaces the Gaussian model with a series of n Gaussian densities. With this model, one assumes that the voxel contains n different groups of fibres and that the molecules are diffusing only within one group (without exchange between the groups). As shown in equation (3.12), the anisotropic diffusion can be generalised to

$$\ln\left[\frac{S(b)}{S(0)}\right] = -\sum_{i_1=1}^{3}\sum_{i_2=1}^{3}\cdots\sum_{i_n=1}^{3} b_{i_1 i_2 \ldots i_n} D_{i_1 i_2 \ldots i_n}, \tag{3.20}$$

where $i, j, \ldots, n$ are the diffusion directions (see [20, chap. 1]). This model is rather unstable because a higher number of tensors is associated with a large number of parameters to estimate [20]. Later published works on this model use constraints to reduce its complexity [3, 45]. Additionally, as mentioned by Van et al. [46], the multi-tensor model becomes less accurate in cases where the number of fibres in the underlying structure in study differ from the number of tensors assumed in the model.

3.4.2. Models based on the orientation of the distribution function

The parametric models introduced in the previous sections require a high number of diffusion measurements that is proportional to the number of parameters of the model [20]. For example for DTI, six independent measurements are necessary. These so-called non-parametric models of

diffusion on the q-space theory make no assumption about the displacement distribution of the water molecules. Instead of using the b-value to define the weight of the diffusion, a parameter q is introduced. Compared to b, q is not a function of time t, but depends on the duration of the phase-encoding period δ expressed as [47]:

$$q = \frac{1}{2\pi}\gamma G\delta, \tag{3.21}$$

where G is the gradient pulse. Although this model could gain consideration in previous studies [48, 5], it is limited by the high acquisition time necessary (standard protocols acquire 500 - 1000 measurements). Such protocols also increase the demands on the hardware since b-values in the order of 30000 s/mm^2 and more are required [20, 2]. This constraint makes the q-space model difficult to apply in clinical settings.

There exist many other models in the literature that were proposed to address the non-Gaussianity of the water diffusion process in biological tissue. For example the stretched-exponential model of Bennett et al. [49] or even the statistical model [8]. These models are not explained in details here because there are only few reports on their application. This thesis is therefore restricted to, and concentrates on, a more novel approach called *Diffusion Kurtosis Imaging* that can be use in clinical settings.

3.4.3. Non-Gaussian modelling with Diffusion Kurtosis Imaging (DKI)

All the experiments that were carried out during this thesis are based on the Diffusion Kurtosis Imaging (DKI) technique. DKI does no more assume that the diffusion distribution function has a Gaussian shape. It estimates the kurtosis that can be seen as a measure to quantify the non-Gaussianity of the probability distribution in the following relationship [6, 50]:

$$K = \frac{\mu_4}{\mu_2^2} - 3, \tag{3.22}$$

with μ_4 and μ_2 that are the 2^{nd} and 4^{th} about the mean of the distribution. When the probability distribution describes a non-Gaussian process, $K > 0$ and in case of a Gaussian process, K is equal to 0.

The diffusion and kurtosis parameters can be estimated analogous to equation (3.7) [6]:

$$S(b) = S_0.e^{\left(-bD+\frac{1}{6}b^2D^2K\right)}, \tag{3.23}$$

where $S(b)$ is the signal intensity considering b, S_0 is the signal without diffusion-weighting, D is the diffusion coefficient and K is the kurtosis. A nalogous to $\mathbf{D_T}$ with 6 independent components, a 4^{th} order 3×3×3×3 fully symmetric kurtosis tensor $\mathbf{K_T}$ (also often referred to as W in the literature) with 15 independent components can be derived from equation (3.23). In order to fully estimate $\mathbf{D_T}$ and $\mathbf{K_T}$, a minimum of 2 different non zero b-values and a minimum of 15 diffusion directions are necessary [6].
The diffusion coefficient and diffusion kurtosis measured along a specific diffusion direction $n = [n_x, n_y, n_z]$ are usually referred to as $D(n)$ and $K(n)$. They are related to the $\mathbf{D_T}$ and $\mathbf{K_T}$

as follows [51]: $\mathbf{D_T}$ and kurtosis tensor $\mathbf{K_T}$ are:

$$D(\mathbf{n}) = \sum_{i=1}^{3}\sum_{j=1}^{3} n_i n_j D_{ij}, \tag{3.24}$$

$$K(\mathbf{n}) = \frac{\mathrm{MD}^2}{D(\mathbf{n})^2}\sum_{i=1}^{3}\sum_{j=1}^{3}\sum_{k=1}^{3}\sum_{l=1}^{3} n_i n_j n_k n_l W_{ijkl} \tag{3.25}$$

where D_{ij} are elements of $\mathbf{D_T}$, and W_{ijkl} are elements of $\mathbf{K_T}$.

Similar to DTI, many eigenvalues and eigenvectors are associated to $\mathbf{K_T}$ [52] and Cheung et al. [50]. To illustrate the physical relevance of DKI following metrics can be used.

- Mean kurtosis (MK) that describes the average kurtosis along all diffusion directions when N uniformly distributed diffusion directions exist:

$$\mathrm{MK} = \frac{1}{N}\sum_{i=1}^{N} K_i. \tag{3.26}$$

- Axial kurtosis (K_{AX}) and Radial Kurtosis (K_{RAD}) to compute the directional diffusion kurtosis along the axial and radial directions of the $\mathbf{K_T}$. The kurtosis tensor W is first transformed to the coordinate system defined by the three eigenvectors ($\mathbf{v}_1$, $\mathbf{v}_2$, $\mathbf{v}_3$) of $\mathbf{K_T}$ as [50]:

$$\hat{W}_{ijkl} = \sum_{i'=1}^{N}\sum_{j'=1}^{N}\sum_{k'=1}^{N}\sum_{l'=1}^{N} e_{i'i}e_{j'j}e_{k'k}e_{l'l}W_{i'j'k'l'}. \tag{3.27}$$

  Here e_{ij} are elements of the 3D rotation matrix P with $P = (\mathbf{v}_1, \mathbf{v}_2, \mathbf{v}_3)$. The diffusion kurtosis along each of the eigenvectors is related to the eigenvalues $\lambda_1, \lambda_2, \lambda_3$ of the diffusion tensor and the mean diffusivity MD by the following mathematical expression

$$K_i = \frac{\mathrm{MD}^2}{\lambda_i^2}\hat{W}_{iiii}, \quad i = 1, 2, 3. \tag{3.28}$$

$$K_{\mathrm{RAD}} = \frac{K_2 + K_3}{2} \qquad K_{\mathrm{AX}} = K_1. \tag{3.29}$$

- Kurtosis anisotropy (KA) is a measure of anisotropy of diffusion kurtosis can be defined as:

$$\mathrm{KA} = \frac{\sqrt{3(K_1 - \overline{K})^2 + (K_2 - \overline{K})^2 + (K_3 - \overline{K})^2}}{\sqrt{2(K_1^2 + K_2^2 + K_3^2)}}, \tag{3.30}$$

  where $\overline{K} = \frac{1}{3}\sum_{i=1}^{3} K_i$. Note that $\overline{K} \neq \mathrm{MK}$ because the 3D kurtosis distribution cannot be represented by a simple ellipsoid.

Some DTI and DKI derived parameters for a human brain acquisition are shown on figure 3.9. White matter regions with a high number of packed fibres as is the case in the corpus callosum exhibit similar patterns on the MK as on the FA map. Grey matter regions that appear dark

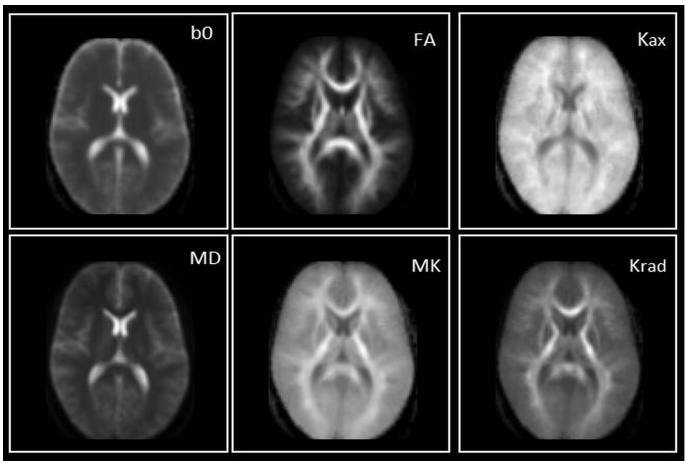

Figure 3.9.: Parameter maps in the human brain for DTI and DKI.

on the FA maps are reflected by higher MK values, indicating restricted non directed diffusion. Only the cerebrospinal fluid (CSF) region has lower values both on the FA as well as on the MK map. These observations depict the additional information contained in the kurtosis for a more comprehensive and sensitive description of tissue microstructure [50].

3.5. Artefacts in diffusion MRI

As with any other imaging modality, MRI suffers from motion and noise artefacts. During this thesis, experiments were carried out and strategies were proposed to reduce the effects of such errors in DKI results (see chapter 4). Therefore, a review of the origins and effects of motion and noise in DW images is the subject of the next sections.

3.5.1. Types of motion affecting DWI

3.5.1.1. Patient movement

Acquiring perfect medical images requires a patient that does not move during the whole image acquisition procedure. For conventional MRI examinations these are approximately 5 - 20 min. But this immobility is often rarely achieved because natural processes such as swallowing, respiration, or even blood flow pulsation are rather unavoidable and will cause errors in the images. If they are not corrected, these so-called motion artefacts could lead to blurred images with less resolution that can considerably reduce the diagnostic accuracy.

Motion often increases with the length of the scan process (even with very cooperative patients). This problem is emphasised in DTI and DKI because the image acquisition time is increased due to the use of many diffusion directions and diffusion-weighting factors as explained in sections 3.2 and 3.4.3.

3.5.1.2. Eddy currents and magnetic susceptibility effects

During a DWI acquisition, the gradient coils produce large magnetic field gradients that are constantly and rapidly switched. This introduces eddy current in the scanner electric resulting

into rapidly and slowly decaying magnetic fields that are not desired. In conventional MRI, this is not a problem, since the gradients are applied for a very short time and for pulse sequences, the eddy currents produced rather tend to self-cancel [53]. Whereas in diffusion imaging to acquire the desired b-value, the gradients are applied for variable long period of time so that the eddy currents do no self-cancel. This leads to the fact that the field gradients used to sample then differ from the field gradient planned for imaging perhaps, the b-matrices of the samples differ from the initial one planned [53, 20]. As the diffusion coefficients and diffusion tensors are calculated voxel wise, using false b-matrices leads to artefacts that shall be corrected.

In addition, if there are large discontinuities in the bulk magnetic susceptibilities, then local magnetic fields occur. Particularly in echo planar imaging (EPI), these local magnetic field gradients are responsible of image distortion. They behave like the diffusion gradients and modify the b-matrix making it spatially variant. A technique that partially solves this problem is when the ratio of the logarithm of the DW and the non-DW signal (see equation (3.7)) is used to cancel the effect of the susceptibility-induced gradients.

3.5.2. Sources of noise

3.5.2.1. Characterisation of noise in MRI

Noise can be described as the signal that is not issued from the physical process measured and that corrupts the true signal. Noise in MRI has several origins [20]. It can be a thermal noise (also called Johnson-Nyquist noise), which is due to random motion of charge carriers in electrical conductors of the MRI scanner system, as well as in the subject's body, which is also conductive. It can also come from the external environment (e.g. outside temperature changes) or signal amplification. Noise can also originate from quantisation errors due to analog-to-digital signal conversion. Despite the multiple sources of noise in MRI, reports in the literature claim that the major sources of noise are the random thermal noise from the patient together with some additional hardware errors [54]. Therefore, this thesis restrict to focus only on such errors.

3.5.2.2. Johnson-Nyquist Image noise in DWI

The logarithm of the signal attenuation in DWI decreases linearly with the b-value and the background noise has a Rician distribution [20].

In comparison to the unweighted signal, the noise level can reduce the signal attenuation leading to underestimation of the diffusion coefficient. For example, when estimating the diffusion tensor, one is effectively sampling a range of ADCs over different orientations and thus, in a given voxel, one may find the estimation of ADC corrupted in some directions (typically, the directions in which the ADC is highest), while not in others. This effect causes underestimation of the trace and anisotropy. The higher the anisotropy, the greater the underestimation of the mean diffusivity. Furthermore in low SNR data, it can also cause erroneous differential contrast between white and grey matter at higher b-values.

3.6. Applying diffusion MRI for neurological and renal tissue characterisation

Using diffusion MRI to study the structure or rather the microstructure of the human brain and kidney tissues as also performed in this thesis is motivated by current research interests in the

field. Many articles in the literature have already highlighted that these organs have properties that make them suitable to be studied with DWI [27, 55, 56, 57].

In the brain, for example, the microstructure of some tissues such as the grey matter (GM), the white matter (WM) and the cerebrospinal fluid (CSF) influences the contrast of the corresponding DW images [58]. In the GM that is mainly composed of neurons and glial cells, researchers have been able to establish the isotropic nature of the diffusion process reporting values of FA $<$ 0.2. In the WM, the presence of anisotropic diffusion due to directed structures such as myelinated axons leads to FA values up to about 0.8. In the CSF where the diffusion process is unrestricted as in water, FA values almost equal to 0 are observed.
Additionally, diffusion properties in the brain change according to the age. Moseley et al. [23] could demonstrate that FA increases with age and reaches its maximum value around the age of 60, then begins to decrease due to the demyelination process.
This sensitivity of DWI makes it to one of the powerful methods to assess several pathologies related to the destruction of tissue microstructure as usually observed in stroke [23] and brain tumours [25]. The FA, MD values will change in case of reduced extra-cellular space corresponding to cell swelling, increased cellularity or increased extra-cellular space when cells shrink, die or in case of membrane disruption. Clinical studies with DTI show its relevance in assessing pathologies that impact the white matter integrity as Alzheimer [59], the Parkinson disease [60] or even multiple sclerosis [24].
Although DKI is a relatively new method, some few articles [52, 9] could already highlight its superiority in characterising tissue microstructure compared to DWI / DTI.

Referring to the description of the renal anatomy in chapter 2, it is clear that the major process in the kidneys is the movement of water. This is explained by the fact that the main function of the kidney includes water re-absorption and concentration-dilution. These movements mainly occur in the tubules and are controlled either by active or passive mechanisms, depending on their location in the nephrons [61]. Therefore details about the diffusion characteristics of the kidney can provide useful insights into the mechanisms of various renal diseases, including chronic renal failure, renal artery stenosis, and even urethral obstruction [62]. In the kidney, the presence of radial structures such as tubules in the pyramids makes the diffusion process anisotropic. Ries et al. [61] found average FA of 0.22 $\pm$ 0.12 in the cortex and 0.39 $\pm$ 0.11 in the medulla clearly indicating the high anisotropy of the diffusion within such compartments of the kidney . The FA values of solid tumours were found significantly higher than that of simple cysts, but renal cell carcinoma showed a wide range of FA values [63]. Various studies in humans report that the diffusion signal might be influenced by blood flow since the kidney is a highly perfused organ. It could be demonstrated that the DW signal is affected by the tissue perfusion within the heart cycle [64]. When low b-values are used for DWI, there is no significant difference between the ADC values of the cortex and the medulla in healthy kidneys [65]; this result is attributed to the effect of higher perfusion effects. There is a significant difference among ADC values of the cortex and medulla in a high b-value approach [65]. With high b-values, the effect of perfusion is cancelled out, and the ADC value reflects mostly diffusion. This statement makes the application of DKI that uses higher b-values compared to DTI in kidneys very interesting and promising of new results.

Chapter 4

Optimisation of the image pre-processing methods for DKI

For fitting the Diffusion Tensor Imaging (DTI) or other higher order diffusion models as Diffusion Kurtosis Imaging (DKI), voxels in different successive diffusion-weighted (DW) images should match to the same anatomical location and additionally the signal level in DWI should not fall down to the noise level. But as explained in section 3.5, misregistration and noise violate these preconditions and typically, all the measured images need to be corrected before model fitting. This chapter reports on software-based correction schemes after data acquisition but prior to diffusional kurtosis estimation that were developed and analysed during this thesis to eliminate motion and reduce noise in DW images.

4.1. Motion correction in DKI images using mutual information

4.1.1. Current limitation of the actual motion correction methods

Most approaches that have been proposed in the literature to account for the problem of misregistration are based on improved diffusion acquisition techniques [66, 67, 68]. For example the use of bipolar gradient schemes reduces susceptibility to motion as well as to eddy currents (introduced in section 3.5.1.2) and is widely employed [69]. Another straightforward approach is to perform most diffusion scans using single-shot Spin Echo Planar Imaging EPI (SSEPI). But the major obstacle of such methods relies in the fact that they are not always applicable to all scanner types and are often unable to correct for larger motion in particular ranges. This thesis concentrates on motion correction techniques after image acquisition: the so-called image-based registration schemes.

4.1.1.1. Image-based registration

In an image-based registration scheme, a cost-function Q is used to measure the spatial alignment of the images [70]. In a first step, an image called the *target* or *reference* image is selected from the set of DW images acquired. This image is used later as reference to correct the other images in the DW series. Each image that is corrected according to the *reference* image is called the *source* or *moving image*. Usually in the literature, the first non-DW image - the b_0 image - is used as *reference*

image. The b_0 image is often used because it contains less distortions and its signal-to-noise ratio (SNR) is higher compared to the DW images [71]. In a second step, one aligns all other images of the DW series to the *reference image* using a transformation model and by optimising the so-called cost-function Q.
Referring to the work of Crum et al. [72], a software-based image registration process can be structured into three parts.

1. Transformation model:
   It defines the geometric transformation **T** between the coordinates needed to transform a *source image* X to match a *reference image* Y. There are many transformation types: rigid, affine and non-rigid transformations. Rigid transformations are characterised by 6 parameters: 3 translations and 3 rotations; affine transformations are characterised by 12 parameters: 6 of rigid plus 3 scaling and 3 shear. In case of more complex deformations, non-rigid transformations (for example the diffeomorphic transformation [73]) are required.

2. Similarity measure:
   It measures the degree of alignment between two images [74]. For this purpose, a cost function Q is defined to quantify the similarity between X and Y and search for the transformation T^* which maximises the similarity cost function.

$$T^* = \arg\min C(Y, T(X)), \tag{4.1}$$

   with $C(X, Y)$ representing the cost function, and $T(X)$ is the result of the transformation of X by T.
   In the literature, there are two classes of cost functions: the feature-based and the voxel-based similarity measures [75]. In the first class, features such as surfaces, lines or points are used and here the distance between these are minimised in the images. The great advantage of a feature-based cost function is that it can be used for mono- and multi-modality registration but the initial feature extraction step needed makes it computationally time consuming [74]. This is the case when features are extracted using landmark detection or segmentation methods. Another drawback is associated with the fact that errors in the feature extraction stage cannot be recovered later and will corrupt the whole registration. To avoid these errors, image intensities can be directly used without the need for feature extraction. The widely used intensity-based cost functions include the mean squared intensity difference (MSQ), the cross correlation (CC) and the mutual information (MI).
   In this thesis the mutual information metric is used to compare the two images. This metric stands out compared to MSQ and CC because it does not compare the grey level of the images but rather their entropies. This characteristic makes MI well-suited for comparison of DW images with changing contrast. MI can be calculated using the following equation [76]:

$$\mathrm{MI}(X, Y) = H(X) + H(Y) - H(X, Y). \tag{4.2}$$

   where $H(X) = -\sum_{\mathbf{x}} p(\mathbf{x}) \log p(\mathbf{x})$ and $H(Y) = -\sum_{\mathbf{y}} p(\mathbf{y}) \log p(\mathbf{y})$. $p(\mathbf{x})$ and $p(\mathbf{y})$ are respectively the probabilities that a voxel within image X, Y has intensity **x**, **y**. The joint entropy $H(X, Y)$, is defined as: $H(X, Y) = -\sum_{\mathbf{x}} \sum_{\mathbf{y}} p(\mathbf{x}, \mathbf{y}) \log p(\mathbf{x}, \mathbf{y})$ where $p(\mathbf{x}, \mathbf{y})$ denotes the joint probability.

An image that has many different intensities contains much information and consequently has a higher entropy than an image with a single intensity that has a low entropy value. Therefore a low joint entropy $(H(X,Y))$ along with high MI reveals that two images are similar. For registration schemes a plausible approach is to maximise MI between two images. Since MI can be affected by the level of overlap between two images, Studholme et al. [77] introduced a normalised mutual information (NMI) that can be written as:

$$\text{NMI}(X,Y) = \frac{H(X)+H(Y)}{H(X,Y)}. \tag{4.3}$$

3. Optimisation process:
   In the registration process, the parameters that maximise the similarity measure are calculated iteratively during the optimisation stage. The optimisation can become very numerically time consuming depending on whether the registration is rigid or not. For example, considering a rigid registration with landmark features comparison, a least square approach can be used to estimate the optimal transformation analytically [76]. But for non-rigid registration processes, where the intensity values of the image are considered, this is difficult to apply because the number of parameters and also the degree of freedom (DOF) is very high. Popular optimisation methods used in previous work are the gradient descent method [78], the conjugate gradient method [79], the Newton type method [80] and evolutionary strategy methods [81].

First applications of image-based registration to correct for distortions in echo planar images registered DW images (source images) using the undistorted T_2-weighted image as *reference image* [82]. The definition of the similarity measure was based on the CC. Unfortunately, registration schemes in which Q derives directly from the voxel values, as with CC or MSQ are inappropriate as measure of similarity for *source* and *reference* images with different contrasts as it is the case in DTI and DKI [83, 84]. These techniques assume that the underlying images derive from the same imaging modality, are perhaps images with the same contrast. Whereas DTI images have low SNR and the changing contrast due to different diffusion encoding directions and weightings will hamper a registration process based on direct grey value comparison [85].

Current approaches to the problem of inter-modality registration have been proposed, using MI, as a new matching criterion [86, 87]. Similarity metrics based on MI showed more robustness compared to metrics based on CC and MSQ [88, 70]. MI requires no specification on the geometry between the two images and is not based on the comparison of the grey values but looks at their entropy. This flexibility makes MI well suited as a criterion of registration of images with different contrast as DW images. Despite the successes of this similarity measure for multimodal medical image registration, its impact on the alignment of diffusion tensor and diffusion kurtosis images remains unclear. One goal of this thesis was to perform a qualitative and quantitative evaluation of the improvement of image quality of DTI results by the use of MI based motion correction techniques.

4.1.2. Algorithm description and implementation

In this thesis, the registration algorithms evaluated were implemented using C^{++} ITK-based libraries and integrated as *plug-ins* in the Digital Image Solutions (DIS) software STROKETOOL version 3.1 [89] that is briefly introduced in the next section. The correction algorithms developed and tested here differ with the choice of the similarity measures considering the 3D rigid body

transformation model together with the gradient descent optimiser. Details of the three MI based similarity measures considered are also discussed.

4.1.2.1. C++ Registration *plug-in* with the Stroketool software

STROKETOOL is an interactive software for evaluation, analysis and visualisation of DWI and Perfusion-Weighted Imaging (PWI) datasets in medical imaging on the Windows® platform. A plug-in technique enables developers to implement their own macros for image processing within the STROKETOOL software. This plug-in technique based here on Microsoft® Visual C++ 2003 - 2010 with the Microsoft Foundation Classes (MFC) was used and the registration algorithms were implemented (see figure 4.1).

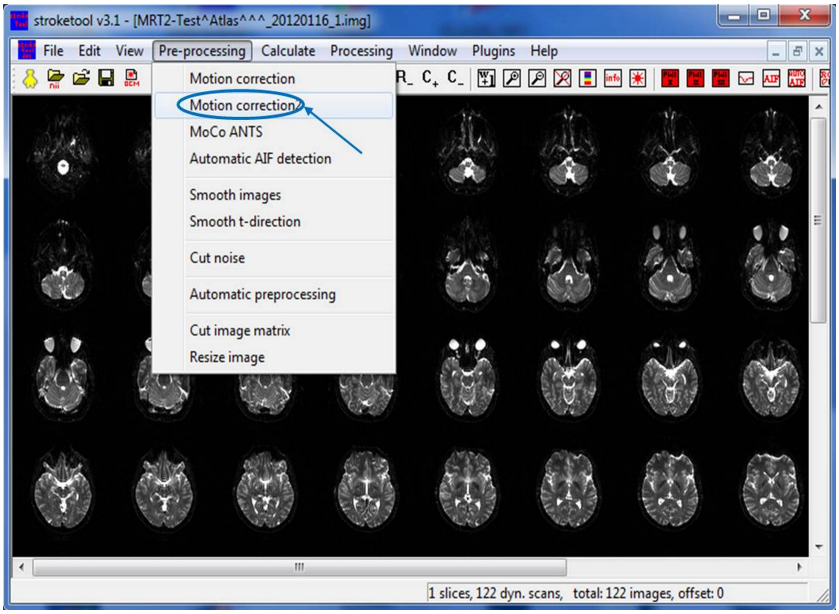

Figure 4.1.: Main interface of the plug-in in the STROKETOOL software.

As starting point for the development, the "MacroPlugin" Visual C++ project of the STROKETOOL based on MFCs was used to load image files as data structures. Then arrays of floats were created to store the image pixels. The processing with the motion correction algorithms described in the next section was executed considering Microsoft Visual Studio 2008 Version 9.0. An excerpt of the software code used is shown on Code 4.1.

Listing 4.1: Excerpt of the software code used for motion correction in Microsoft Visual Studio 2008 Version 9.0.

```
// imregMattes.cpp : Defines the entry point for the DLL application.
...
declspec(dllexport) int RegisterImage2to1(short *pixdata1, short *pixdata2, int xdim, int ydim,
                                          int zdim){
        double time1 = 0.0;
        double tstart;

        // define image dimension and data type
        const  unsigned intImageDimension = 3;
        typedef  float PixelType;
        // define fixed and moving image
        typedef  itk::Image<PixelType, ImageDimension> FixedImageType;
```

```
        typedef   itk::Image<PixelType, ImageDimension> MovingImageType;

        typedef   itk::VersorRigid3DTransform <double> TransformType;
        typedef   itk::VersorRigid3DTransformOptimizer OptimizerType;
        typedef   itk::MattesMutualInformationImageToImageMetric <FixedImageType,
                                                                  MovingImageType > MetricType;
        typedef itk:: LinearInterpolateImageFunction <MovingImageType, double> InterpolatorType;
        typedef itk::ImageRegistrationMethod <FixedImageType, MovingImageType > RegistrationType;
        typedef itk::CenteredTransformInitializer <TransformType, FixedImageType,
                                                   MovingImageType > TranformInitializerType;
...
```

4.1.2.2. Description and implementation of the different MI based motion correction algorithms

The first two algorithms are based on the MI similarity measures as published by Viola and Wells [87] (Viola-Wells implementation) and Mattes et al. [86] (Mattes implementation), respectively. The third algorithm is based on a modification of the algorithm presented in Mattes et al. [86] (Mattes-Smoothed implementation).

***1. Viola-Wells* algorithm** is implemented with a simplified computation of the MI by normalising the statistical distribution of the two input images [77]. In a first step, Gaussian density is used as a smoothing kernel and filtering is performed on the images prior to the registration process. This step helps increasing the robustness against noise. In a second step, two separate intensity samples S and R are retrieved from the image: the first sample is used to compute the density, and the second one to approximate the entropy as a sample mean, [90]. For this method, various smoothing parameters and number of spatial samples can be chosen that influence the results of the algorithm. Gaussian density was used as a smoothing kernel, where the standard deviation σ acts as the smoothing parameter. For the computation, simulations were done using different number of spatial samples N. For the brain data used here, $N = 50$ worked well as starting value and was updated at each iteration. Considering the *reference* image Y and the *moving* image X, the NMI is calculated according to equation (4.2). The quality of the density estimates are chosen according to the standard deviation of the Gaussian kernel. The optimal choice differs depending on the type of the image. For images that have been normalised to have a mean of zero and standard deviation of 1.0, the standard deviation that works well is 0.4 [90].

2. *Mattes* implementation required no filtering step as well as no pre-normalisation step as the metric internally rescales when calculating the discrete density functions. Only one spatial sample set was used for the whole registration process instead of using new samples at each iteration as with the Viola-Wells method. To compute the entropy, the histogram approach that is quick and simple to calculate was considered [90]. Here the entropy is approximated by constructing a histogram of the images and then calculating its discrete entropy that is the maximum-likelihood (ML) estimate of the discretised frequency distribution. Constructing a histogram requires in a first step to *bin* the range of values and count how many values fall into each interval. During this process, the whole range of values of the image is distributed into small intervals. In the resulting histogram the height of the rectangle is proportional to the counts and the width to the size of the bin. After performing some simulations with different number of bins, the optimal value of 24 bins was used in the registration. Using the sample set, the marginal and joint probability density function (PDF) are calculated at discrete positions. Entropy values result from the integral over the bins.

3. *Mattes-Smoothed* implementation was similar to the afore described Mattes method but

consisted of an additional filtering process with a discrete Gaussian kernel. For the data used, a variance of 2.0 prior to the registration worked well [90].

4.1.3. Experimental verification using brain images

To analyse the quality of the developed registration algorithms a study was carried out with real DWI data and artificial DWI data with simulated motion.

4.1.3.1. Input data

Data of sixteen healthy volunteers (7 males and 9 females, mean age 29.41 $\pm$ 6.89 years, range 22 years – 46 years) without any history of neurological disease were acquired using a clinical 3T MRI scanner (Magnetom Trio, A TIM system; Siemens Medical Systems, Erlangen, Germany) equipped with a 12-channel head coil.

For DTI, a single-shot Spin Echo Planar Imaging (SSEPI) sequence was applied in the axial plane. Volumes of 50 slices without gaps in 20 diffusion directions with b-values 0 s/mm^2 and 1000 s/mm^2 and 3 signal averages were acquired (see figure 4.2). Further imaging parameters were as follows: echo time (TE) = 112 ms, repetition time (TR) = 7700 ms, matrix = 128 $\times$ 128, field of view (FOV) = 256 mm, image resolution = 2.0 $\times$ 2.0 $\times$ 2.0 mm^3. GRAPPA (generalised auto-calibrating partially parallel acquisition) was applied with an acceleration factor of 2. The total acquisition time was 08:30 min.

Additionally, DTI data of one tumour patient (male, 40 years with a low-grade astrocytoma[2]) who had received an MRI scan for clinical reasons using the same protocol for acquisition of DTI were retrospectively evaluated.

The institutional review board approved the protocols and written informed consent was obtained from all volunteers before data acquisition.

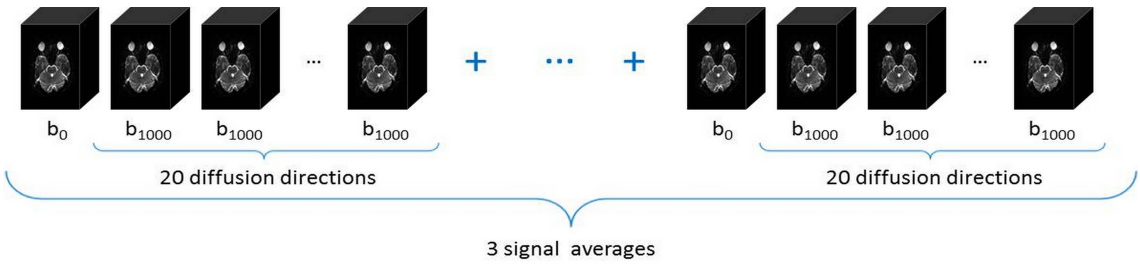

Figure 4.2.: DW Image acquisition of a brain volume with 50 slices at a diffusion-weighting of 1000 s/mm^2 considering 20 diffusion directions and 3 signal averages.

For each subject the 63 DWI volumes acquired were transferred to a workstation running under a Windows 7 platform (Intel® Core™ 2.66 GHz i5 processor, 8.00 GB RAM) for correction of subject motion using the described C++ routines (see section 4.1).

4.1.3.2. Motion correction accuracy

In the literature, different processing workflows for DWI motion correction exist. In a study of Tremblay et al. [91], only $b = 0$ images were registered and the resulting transformation

[2] is a malignant tumour of nervous tissues that is composed of astrocytes.

matrix was applied to the subsequent DW images, assuming constant motion between the subsequent $b = 0$ s/mm^2 images. Similarly, in a study of Haselgrove and Moore [82] with 5 b-values (0, 160, 360, 640, 1000 s/mm^2) the correction factor found by registering the b_0 to the $b = 160$ s/mm^2 image was used to correct the other DW images with the expectation that the transformation parameters were linearly related to the relative gradient. Since the required use of a higher number of directions together with multiple b-values lengthens the scan times, the probability for non-constant motion between images of the same measurements cycle becomes high. Therefore, two processing pipelines were evaluated (see figure 4.3). First, the first non-DW b_0 volume was picked from the DTI dataset and used as *reference volume*. Then all the other DW volumes were registered onto this volume (see figure 4.3 (a)). The second approach was set up analogue to prior studies [91] as reference. Here, the first b_0 volume was spatially mapped to the second b_0 volume then to third b_0 volume and the two resulting transformation matrices were respectively applied on the DW images in the second and third averages (see figure 4.3 (b)).

Tests were performed by Viola-wells, Mattes and by Mattes-Smoothed to find the best registration results (see section 4.1.2). The accuracy expressed as deviation in correcting induced motion together with processing times was analysed. Finally, the b-matrices were recalculated to take into account the effects of the spatial transformation [70].

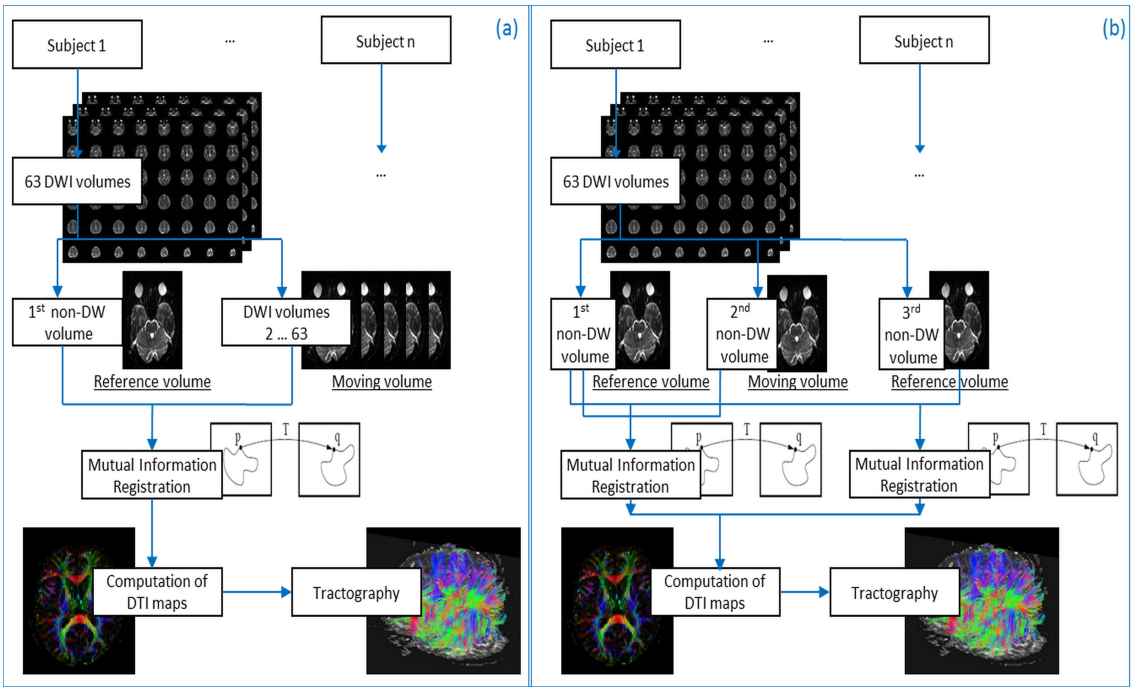

Figure 4.3.: Block diagram description of the processing pipelines tested. (a) The 1^{st} non-DW image was used as reference to align all the following volumes of the subject. (b) Only the b_0 images are registered and the resulting transformations are applied to the DWI volumes.

4.1.3.3. Quantitative evaluation

To validate the implementations and determine their accuracy, simulations on datasets with known deformations were performed (see figure 4.4). Data of a volunteer showing visually fewer motions were registered with SPM8 [92] software using a least square approach and a

6 parameter rigid body spatial transformation. Here all the 62 DWI volumes of the volunteer were registered to the first b_0 volume. The resulting data were again visually inspected for motion and used as our gold-standard dataset for evaluation implemented algorithms (4.1). Artificial misalignment was then induced by random rotation (from 0.01 ° to 0.20 °) and random translation (from 0.01 mm to 10 mm) in the 62 DWI volumes of our gold-standard dataset. These misalignment ranges are in a realistic magnitude of usual patient movement [82, 91]. This process was repeated to produce 6 distinct artificial motion-corrupted data sets that were used for further tests. The resulting datasets were then registered with the Viola-Wells, the Mattes and Mattes-Smoothed algorithms described in section 4.1.2.2. To assess the performance of the motion correction algorithms, the offset of the transformation parameters between the gold-standard data and the misaligned data was compared to the offset between the gold-standard data and the registered data.

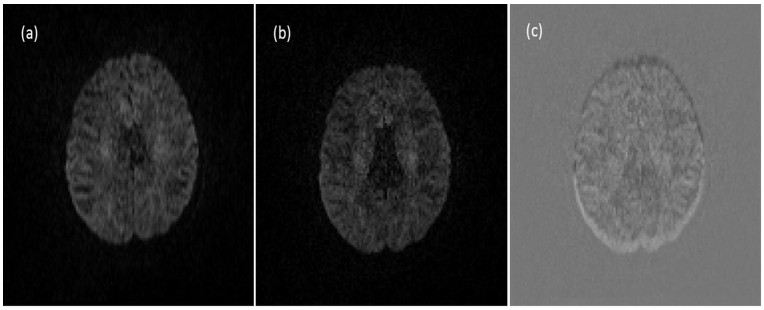

Figure 4.4.: Axial DWI images of a volunteer brain (a), intentionally misadjusted DWI image with known motion (b) and difference image between misaligned and original image (c).

Furthermore, from the gold-standard and motion-corrected DWI volumes (the datasets without induced artificial motion), the mean diffusivity (MD) and the fractional anisotropy (FA) metrics as statistics of DWI and DTI were calculated using the Diffusion Toolkit software [93] (trackvis.org/dtk, version 0.6). The resulting SNR in FA maps in the corpus callosum representing a region consisting of homogeneous tissue (see figure 4.9) was calculated according to equation (4.4).

$$\text{SNR} = \mu/\sigma \tag{4.4}$$

with μ as mean or expected value and σ as the standard deviation (SD) of the noise. To further analyse the impact of motion artefacts on DTI imaging, the WM fibre tracts were reconstructed in the Track Vis software [93]. The Track Vis program provides different fibre tracking algorithms to reconstruct the nerve fibres. As fibre propagation algorithm, the tensorline method [94] was employed (angle threshold = 35 °) with no FA-based threshold for fibre tracking. As an indicator of data quality, the minimum, maximum and mean fibre length and volume in the created tracks was calculated. The track count and voxel count involved were also reported.

4.1.3.4. Visual inspection with tumour data

For better visualisation, data of a tumour patient were registered with the motion correction technique that showed best performance in recovering translation and rotation misalignment to demonstrate how motion induced artefacts can impact on fibre tract changes in brain lesions.

4.1.3.5. Statistical analysis

All data are expressed as mean $\pm$ SD. Parameters were compared using sample t-tests. Statistical values of $p \leq 0.05$ were considered to indicate a statistically significant difference.

4.1.3.6. Results

From the 16 whole brain DTI datasets acquired for validation of the experiments, data of one subject who could not complete the acquisition process due to intense motion was discarded. Therefore, data of 15 volunteers were successfully registered.

Differences were found between the processing pipelines in figures 4.3a and 4.3b. Just registering the b_0 volumes could not outperform the processing configurations with a registration of all the DW volumes (see figure 4.5). As shown on the figure, considering the pipeline 4.3a, different motion experienced by the subsequent volumes of a dataset are corrected whereas the correction process in pipeline 4.3b does not account for all motion errors. Further investigations were made under consideration of the pipeline on figure 4.3a. Under best configuration of the algorithms for sixty-two DW volumes when each volume was registered, an average of 06 min : 57 s for Viola-Wells, 02 min : 41 s for Mattes and 02 min : 04 s for Mattes-Smoothed were required to register the 62 volumes.

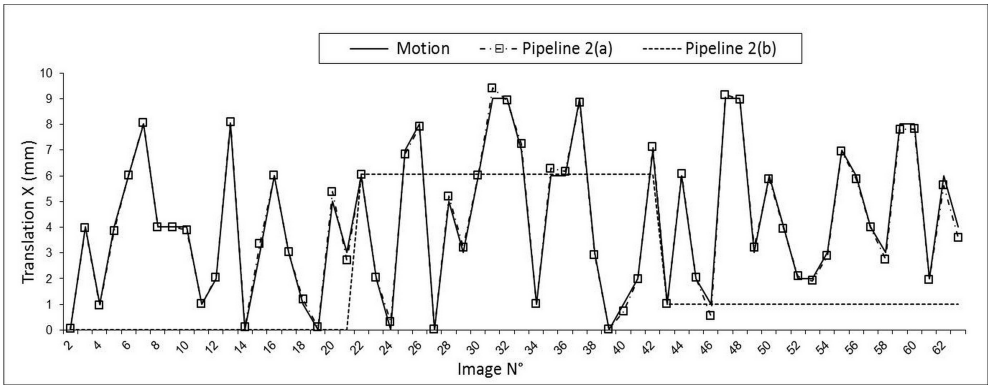

Figure 4.5.: Comparison of the two processing pipelines. Motion correction of all different DTI volumes is superior to correction schemes, where only b_0-images are aligned.

The graphs in figures 4.6 and 4.7 summarise the results of the simulation studies. Translation measures after registration of data with known induced artificial motion in x-, y-, z-direction with the best configurations of the different algorithms under consideration of the pipeline in 4.3a are shown for all the volunteers.

Considering translations up to 10 mm and rotations up to 0.20 ° respectively the ...

Scatterplots of the artificial induced motion and transformation parameters after registration are presented in figure 4.8. These analyses showed for translation and rotation measures respectively that Mattes ($R^2 > 0.99$; $R^2 > 0.99$) followed by Mattes-Smoothed ($R^2 > 0.96$; $R^2 > 0.93$) over performed Viola-Wells ($R^2 > 0.83$; $R^2 > 0.28$). All translations results before and after the registration correlated better compared to rotation measures.

The tractography results confirm the findings obtained with the translation and rotation parameter analysis. Example images from a registered dataset are shown in figure 4.9. Representative FA maps without correction demonstrates that motion corrupted datasets exhibit considerable blurring. FA maps with and without registration allowed a side-to-side comparison

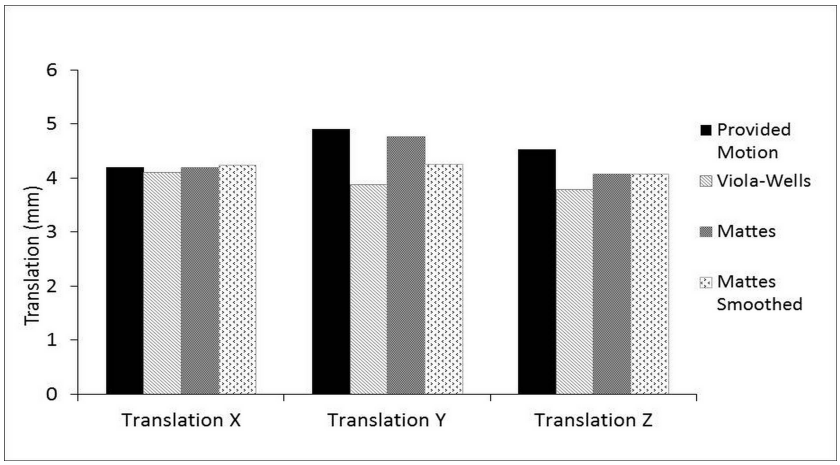

Figure 4.6.: Comparison of translation measures in the X, Y, Z directions after registration of data with known induced artificial motion for the six motion-corrupted datasets.

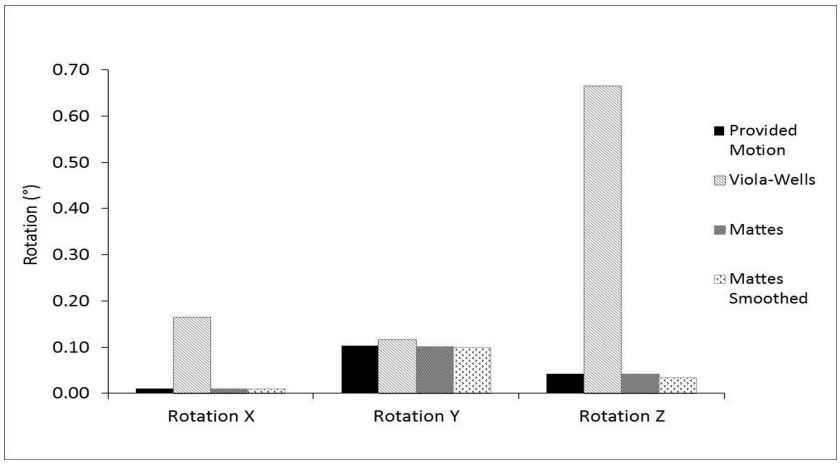

Figure 4.7.: Comparison of rotation measures in the X, Y, Z directions after registration of data with known induced artificial motion for the six motion-corrupted datasets.

demonstrating the potential of the mutual information registration technique by Mattes and its strengths in contrast to the Viola-Wells and Mattes-Smoothed methods. Unrealistically high diffusion anisotropy values at brain boundaries in FA maps without correction as typical indices of geometrical discrepancies were corrected after registration. SNR in corpus callosum measured in FA maps was improved by all registration methods from 6.17 in the non-corrected data to 16.82 ($p = 0.03$) in the data with Mattes mutual information correction (see table 4.2). A SNR of 16.75 ($p = 0.014$) showed that a smoothing process during the registration with Mattes does not render additional enhancement. Registration with Viola-Wells achieved the lowest result with SNR of 16.29 ($p = 0.03$).

The morphometric results of white matter tracts from all the subject brains are presented in table 4.3. Compared to the results from data with correction, the white matter tracts in the brain are greatly reduced in the motion-corrupted datasets. The mean length (meanL) of the reconstructed fibres of all the volunteers without correction significantly increased from 60.03 mm to 79.90 mm after registration with Mattes-Smoothed using tensorline as propagation

Table 4.1.: Result of the simulation studies considering translations up to 10 mm and rotations up to 0.20 °.

	X	Y	Z	X	Y	Z
Average deviation translation [mm]	0.73	0.64	1.15	0.06	0.34	0.43
Maximum deviation translation [mm]	< 1.34	<1.19	< 2.99	< 0.15	< 0.71	< 1.13
Average deviation rotation [°]	0.13	0.07	0.15	0.01	0.08	0.004
Maximum deviation rotation [°]	< 0.5	< 0.2	< 0.62	< 0.05	< 0.03	< 0.01

Table 4.2.: SNR in corpus callosum in FA parameter maps from all subjects using different motion correction techniques.

Method	*Uncorrected*	*Viola-Wells*	*Mattes*	*Mattes Smoothed*
SNR	6.17	16.29	16.82	16.75

algorithm (see figure 4.10). For the maximal recovered length (maxL) of 442 mm with Mattes, the corresponding volume (V) was 442.95 cm^3. Here the best results were achieved with Mattes-Smoothed followed by the correction with Mattes mutual information, then with Viola-Wells. Where longer fibre lengths were recovered, the voxel count was increased and the tract count diminished.

Table 4.3.: SNR in corpus callosum in FA parameter maps from all subjects using different motion correction techniques. TC:tract count, VC: voxel count, V: volume, maxL: maximum length, minL: minimum length, meanL: Mean length.

Meall all Subjects	*TC*	*VC*	*V [cm^3]*	*maxL [mm]*	*minL [mm]*	*meanL [mm]*
Motion	6204	43958	351.66	260.34	1.49	60.03
Viola-Wells	6218	54632	421.12	390.47	1.56	76.86
Mattes	6131	55369	442.95	442.66	1.53	78.02
Mattes-Smoothed	6147	56908	455.26	429.97	1.53	79.90

Visual inspection of the algorithms performance using data of a tumour patient revealed that without correction it is nearly impossible to notice how the fibres are displaced by the tumour in the coronal view. In the sagittal view (see figure 4.11), the tumour localisation was already noticeable without correction but a more precise fibre progression with more volume all around the tumour was only detected after motion correction.

4.1.3.7. Discussion

Considering two processing pipelines, three mutual information based motion correction methods were implemented and evaluated for alignment of DTI datasets [87, 86, 77]. The registration was performed in 3D and allowed for rigid body subject motion correction. After registration, the b-matrices were properly rotated for DTI processing.

For validation, quantitative measures such as translation and rotation after registration of DTI datasets with artificial induced known motion as well as the visual inspection using data of a

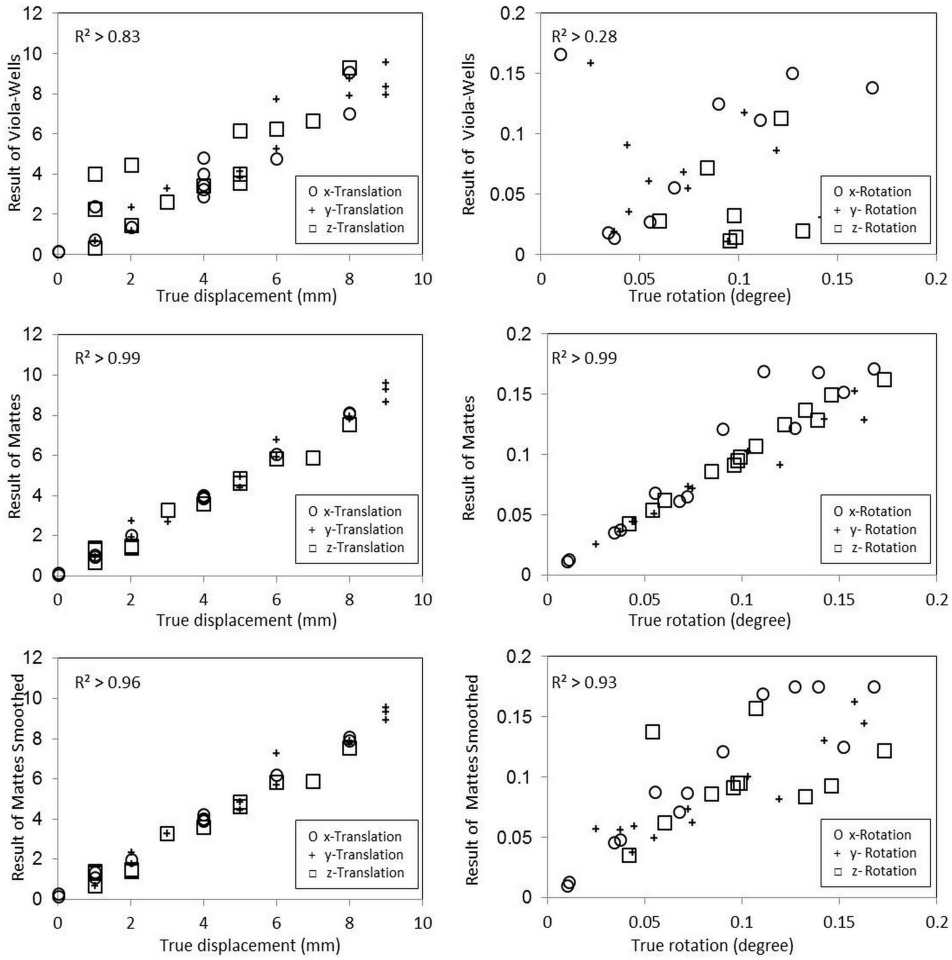

Figure 4.8.: Results of the simulation studies. Each graph displays the transformation parameters found by the registration methods (y-axis) in the six motion-corrupted datasets (true values, x-axis). The individual graphs show the result of the registration after applying various degrees of x- (circles), y- (plus marks) and z- (squares) translation (left) and rotation (right). The parameters found by the registration with Mattes achieved the best agreement with the true values.

tumour patient were used. Additionally in the corpus callosum, the SNR in the FA maps was studied and the length, volume, track count and voxel count of the reconstructed fibres in the whole brain before and after correction were analysed. All the results showed that the quality of the DTI images was significantly improved after alignment. A comparison of the processing pipelines revealed more accurate registration results when aligning all the DW images compared to spatially matching of b_0 images only. In the literature, different processing workflows for DWI motion correction exist [82, 29, 91]. In a study of Tremblay et al. [91], only $b = 0$ images were registered and the resulting transformation matrix was applied to the subsequent DW images, assuming constant motion between the subsequent $b = 0$ s/mm^2 images. Similarly, in a study of Haselgrove and Moore [82] with 5 b-values (0, 160, 360, 640, 1000 s/mm^2) the correction factor found by registering the b_0 to the $b = 160$ s/mm^2 image was used to correct the other DW images with the expectation that the transformation parameters were linearly related to the relative gradient. Since the required use of a higher number of directions together with multiple b-values

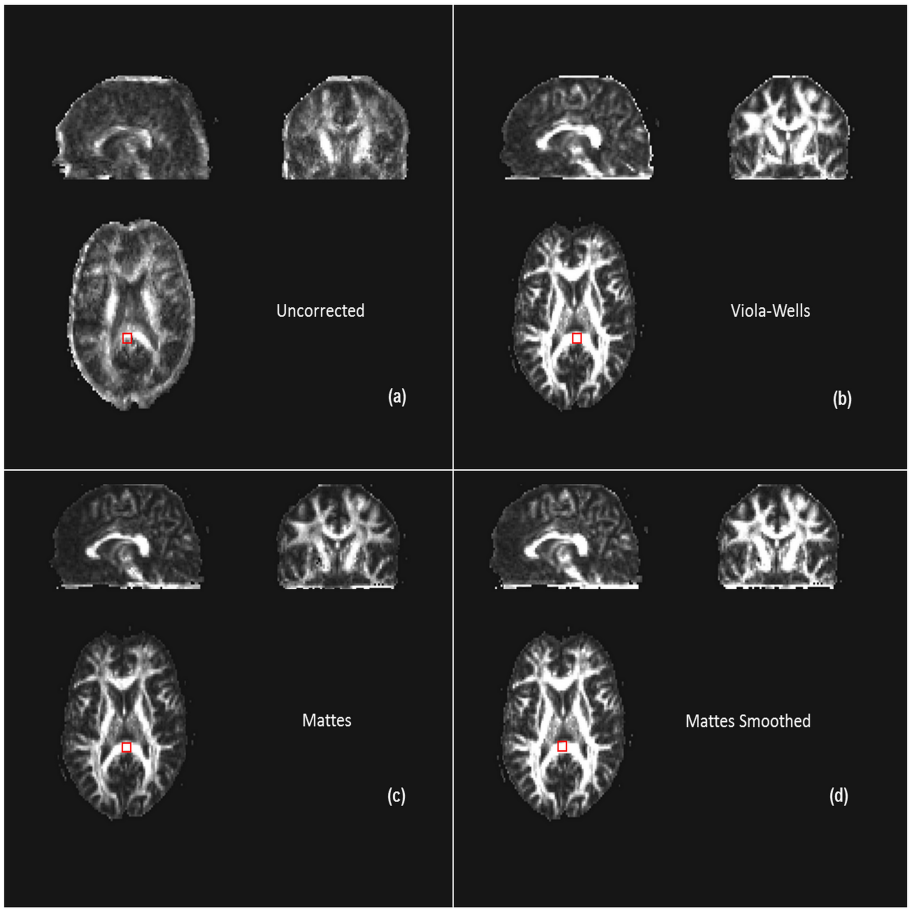

Figure 4.9.: Maps of the fractional anisotropy (FA) without correction (a), after correction with Viola-Wells (b), after correction with Mattes (c) and after correction with Mattes-Smoothed (d). The MI registration with Mattes (c) is clearly superior to the correction with its smoothed version (d) and the MI registration method by Viola-Wells (b).

lengthens the scan times, the probability for non-constant motion between images of the same measurements cycle becomes high. Therefore as the results suggest, for each DTI volume, it is necessary to compute a spatial transformation to the *reference image*.

A recently published study of Yasmin et al. [95] could correct translations up to 3 mm in DTI images by optimising the k-space acquisition and reconstruction method used. An automated 3D registration method for multi-contrast MR imaging proposed by van't Klooster et al. [96] could be used to correct misalignment of about 2.4 mm in three dimensions. In this thesis, the simulated data with artificial misalignment by random rotation from 0.01 ° to 0.20 ° and translation from 0.01 mm to 10 mm, mean residual absolute values after registration were $<$ 0.47 mm and 0.05 °. The resulting reconstructed white matter volumes in a range of 351.66 cm^3 - 455.26 cm^3 are comparable to results of Tang et al. [97] with volumes in range of 398 cm^3 - 394 cm^3. From the DTI processing using the tensorline fibre tracking algorithm, the resulting fibre lengths of 60.03 mm – 79.90 mm were slightly lower than those reported by Tang et al. in range of 105 mm – 122 mm. These small differences might be due to the different fibre tracts assessment techniques involved in the studies as well as the fact that Tang et al. performed their experiments ex-vivo. In their study, Tang et al. [97] estimated the fibre tracts in brain using a systematic uniform random

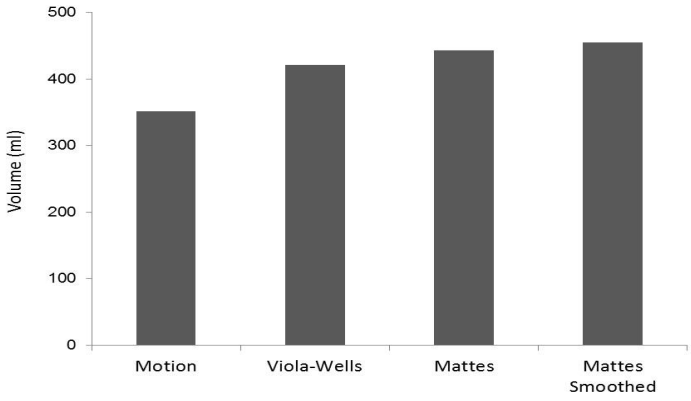

Figure 4.10.: Comparison of the total volume fibre tracts for all the subjects with different registration methods using tensorline as propagation algorithm.

sampling technique that assumes that all brain regions under consideration have equal probability of being sampled. A recent study of Borius et al. [94] evaluating various tractography algorithms could already highlight the potential of tensorline methods. The necessity of motion correction prior to DTI computation was demonstrated using the tensorline algorithm on data of a tumour patient.

For the simulations on artificial data and the SNR measurements in the healthy volunteers, Viola-Wells and Mattes-Smoothed showed poor results compared to the Mattes method. From the evaluation based on tractography measures Mattes-Smoothed showed the best performance followed by Mattes and Viola-Wells.

From the results obtained, if patient motion is present, correcting the data for misalignment with MI prior to DTI processing seems essential. Here accordingly with the simulated data, the best results were achieved with Mattes-Smoothed algorithm that lightly outperformed the Mattes algorithm.

SNR measurements were better with Mattes compared to Mattes-Smoothed algorithm. But Mattes-Smoothed could outperform the other methods with the highest values of reconstructed fibre tracts, volume and length. From these evaluation results, the differences of the algorithms in recovering translational and rotational motion as well as SNR measurements results were more pronounced than the differences in morphometric measures (see figure 4.8). Therefore, the use of the mutual information of Mattes as similarity measures when registering DTI images is recommended.

Patient motion is a common problem in clinical diffusion imaging acquisitions. Here in the experiments carried on, correcting each and any diffusion-weighted image measured at different b-values significantly increases the reproducibility. The results show that datasets containing significant motion can be successfully corrected with MI as a similarity measure.
Although in the present study the tests were performed for the purpose of spatially aligning DTI images of the human brain, it is expected to be beneficial to register images of other body regions [98].

The main limitation of this study lies in the fact that EPI sequences applied in the axial plane in 20 directions with b-values of 0 s/mm^2 and 1000 s/mm^2 were used. It is well known that such sequences are prone to artefacts caused by time-varying magnetic fields that are induced into

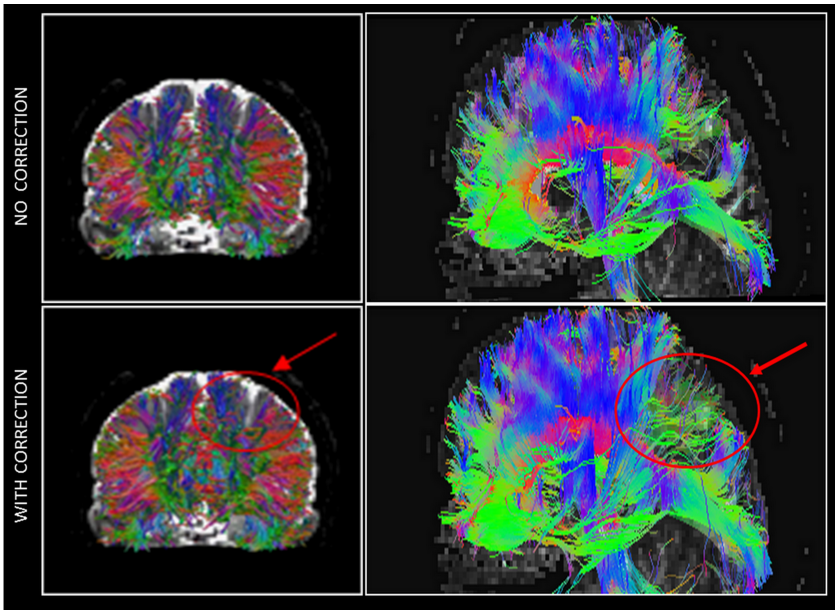

Figure 4.11.: Tractography results of tumour patient data underplayed with b_0 images without and with Mattes motion correction using the tensorline fibre tracking algorithm. Circled region and arrows show more precise fibre progression with more volume all around the tumour detected only after motion correction.

the electric conducting MRI hardware by the rapid gradient echoes of the EPI sequence. In these experiments, "rigid body" was used as the spatial transformation model. A consideration of affine registration would help to remove distortions caused by eddy current artefacts and might increase the performance of MI used as similarity measure in motion correction for DTI. Additionally, a comparison of the correction scheme introduced here to a "gold standard" should be investigated in future studies. As an early step, the primary focus of this work was led on the additional value of mutual information correction in DTI by aligning all the DWI volumes. Moreover, optimisation of motion correction algorithms for modern imaging technologies that consider patients with movement disorder as Parkinson disease or Non-compliance patient is a relevant field of research and should be investigated in future studies.

In summary, formulations of MI based motion correction were implemented and tested here. In previous reports, the registration of DW images was based only on aligning the b_0 images of the acquisitions since they had the same contrast using cross correlations (CC) or mean squared intensity difference (MSQ) as similarity measures. With the introduction of MI, registering images with different contrast is possible. Here, the proposed approaches retrospectively correct for motion prior to DTI computation aligning all the non-DW as well as the DW images using the MI criterion. As a result, they provide maps of quantities derived from the diffusion tensor that are more anatomically accurate. The considered data suggests that using Mattes mutual information as a similarity metric for registering each and any DW image measured at different b-values increases the accuracy of DTI analysis.

4.2. Noise filtering in DKI using weighted least squares

4.2.1. Rice distributed noise in DKI images

For an accurate use of DKI in the clinical routine, it is crucial to remove bias introduced by noise by filtering the individual DW images prior to fitting the tensor model. However, the Rician nature of the noise in DWI [99] prevents from the use of conventional Gaussian-based filtering techniques that may blur important image features and edges destructing diagnostically relevant information. Numerous approaches have been developed to denoise DW images. One can regularise the tensor fields after the diffusion tensor has been estimated [100, 101] or even estimate the diffusion tensor to account for the Rician model [102, 103] or also denoise the DWI volumes before estimating the diffusion tensor.

This thesis concentrates on the last group of techniques and compares 2 classes of filters to reduce noise in DWI images prior to DKI computation, which includes the application of anisotropic smoothing kernels such as Perona-Malik filter [104] and the Linear Minimum Mean Squared Error (LMMSE) filter [99] for conventional MRI and adapted for DWI by Tristán-Vega and Aja-Fernandez [105]. Due to the effectiveness in reducing noise while preserving edges and local details, and without introducing undesirable image artefacts, the anisotropic diffusion filter (ADF) (terminology according to [106, 104]) is one of the most commonly used technique in medical image denoising.

4.2.2. Analysis and evaluation of non-linear anisotropic diffusion filtering compared to joint LMMSE approach

The non-linear anisotropic diffusion filtering [104], where the term *diffusion* should not be confused with the physical diffusion process introduced in chapter 3, and the joint LMMSE approach [107].

4.2.2.1. Non-linear anisotropic diffusion filter (ADF)

The basic idea behind anisotropic diffusion filtering, is to apply a smoothing filter on an image while preserving significant details (edges or lines) that are important for the interpretation of this image. The first approach to realize this concept was proposed by Perona and Malik [104] using the following partial differential equation (PDE) [108]:

$$\frac{\partial I(\mathbf{s},t)}{\partial t} = \mathrm{div}\left[g\left(\left|\nabla I_s^t\right|\right)\nabla I_s^t\right], \tag{4.5}$$

where, $I(\mathbf{s},t)$ is the image intensity to be corrected, $\mathbf{s} = (x,y,z)$ and t are, respectively, the 3D spatial coordinate vector and the stopping time parameter (number of iterations) of the algorithm. The operator ∇ is the gradient operator and the function $g(\cdot)$ refers to the edge-stopping function. From the various possible edge-stopping functions,

$$g\left(\left|\nabla I_s^t\right|\right) = \exp\left\{-\frac{1}{2}\left(\left|\nabla I_s^t\right|/\sigma^2\right)\right\} \tag{4.6}$$

was used that prioritises high-contrast edges over low-contrast ones [108]. Here σ represents the scale parameter which controls the decreasing rate of the diffusion coefficient as the absolute value of the image gradient increases. The value of σ is usually manually set in relation to

the gradient strength of edges in the images that are to be preserved during the diffusion. In summary, the main parameters of the ADF that control the behaviour of the smoothing process are: the scale parameter (σ), the diffusion rate (λ) and the number of iterations (t) of the algorithm.

The optimal number of iterations is set based on the structural similarity index according to the work of Ferrari [108]. Here the time step as well as the gradient modulus threshold that controls the conduction were varied for denoising a volume and the mean structural similarity index (MSSIM) between the denoised volume at iteration (Iter) and the denoised volume at Iteration Iter $+ 1$ was compared with the previous MSSIM index between the volumes at Iter $- 1$ and Iter [108]. The iteration was stopped when the actual MSSIM was inferior to the previous MSSIM [108]. For the data considered here, the time step was optimised and set to 3/44 (see figure 4.12).

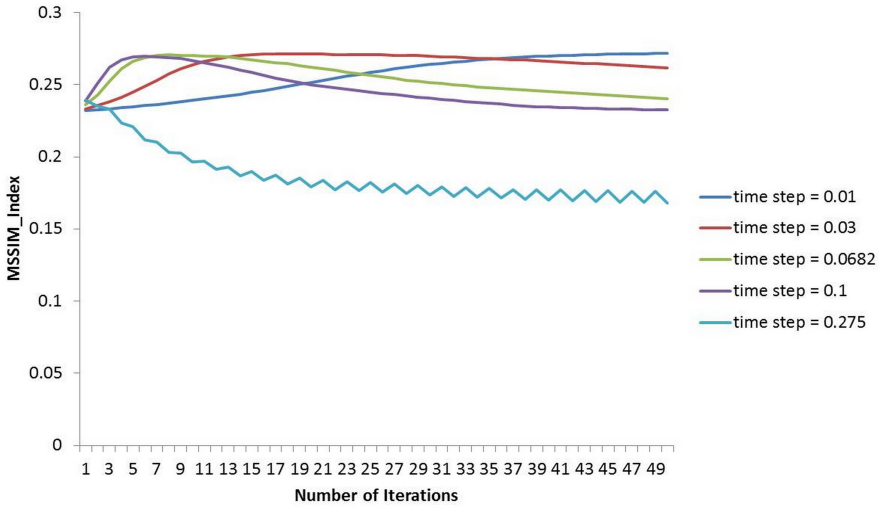

Figure 4.12.: MSSIM index for the ADF correction with different time steps.

4.2.2.2. Joint LMMSE approach

This is a vector LMMSE approach, in the sense that the DWI gradient images of a measurement are filtered together using the Wiener filter over the squared magnitude image M^2. The advantage of working with the square envelope M^2 is that its moments are trivially related to the signal A and the power of noise σ^2 [107].

$$A^2 = E\left\{M^2\right\} - 2\sigma^2;$$
$$A^4 = E\left\{M^4\right\} - 8\sigma^2 E\left\{M^2\right\} + 8\sigma^4.$$

The filter considers all the DWI gradient images simultaneously and is based on the previous published LMMSE filter [99], that is able to detect anatomical structure(s) hidden in correlation information between the separated gradient images. The moments estimates are computed as sample means, and to avoid the over-blurring due to this methodology a non-local means (NLM) scheme is used to distinguish between voxels of different fibre bundles, in such a way

that anatomical structures of the DWI are enhanced.
The implementation of Tristan-Vega et al. [107] considers a stationary Rician model for the noise pattern (i.e., a constant value of σ), which may not be a realistic assumption since parallel acquisition and echo-planar imaging are used. Therefore, the algorithm was modified to generalise the Rician statistics to a non-central Chi model.

For simulation and test purposes, the two algorithms were implemented in MATLAB routines. Details about the data used are found in section 4.2.3.1 and results of the quantitative evaluation and visual inspection are shown respectively in sections 4.2.3.2 and 4.2.3.3.

4.2.3. Validation on synthetic and real brain data

To test the performance of the noise reduction methods investigated in this thesis, a quantitative evaluation and a visual inspection based on synthetic and real DKI data is performed.

4.2.3.1. Input data

Synthetic data

For the quantitative evaluation, synthetic DWI brain datasets of the NITRC project were used [109]. The NITRC project provides DW datasets generated using a multi-tensor model at different SNRs and different sets of diffusion gradient directions. The SNRs available are varied from 9, 18 to 36 and one can choose to use the data with 20, 30, 40, 60, 90 or 120 gradient directions. The SNRs and gradient direction sets are provided in 10 repetitions of the data. This is done for all the data, $b = 1000$ s/mm^2, as is common for clinical acquisitions. For the experiments of this section, DWI datasets with SNR = 9 and SNR = 36 were used. The volumes with SNR = 9 were considered as noisy and the ideal data were the volumes with SNR = 36. 30 diffusion directions were considered.

Real data

Applying the implemented algorithms on real data is necessary to get an impression of the practical usability of the noise reduction methods. A real brain dataset was acquired from a young 22-years old volunteer (female) on a clinical 3T MRI scanner (Magnetom Trio A TIM System; Siemens Medical Systems, Erlangen, Germany) using a 12-channel head coil. DKI data was acquired using a single-shot Spin Echo Planar Imaging (SSEPI) sequence in the axial plane using 3 b-values (0, 1000, 2000 s/mm^2) and 30 diffusion encoding directions. A volume of 60 slices covering the entire brain without gaps was acquired thus enabling the assessment of a wide range of anatomical regions in the atlases. Further imaging parameters were: echo time (TE) $=$ 101 ms, repetition time (TR) $=$ 8100 ms, matrix $= 92 \times 92$, field of view (FOV) $=$ 230 mm, number of averages $= 2$, reconstructed image resolution = $2.5 \times 2.5 \times 2.5$ mm^3. Generalised auto-calibrating partially parallel acquisition (GRAPPA) as a parallel imaging method was applied with an acceleration factor of 2. The mean acquisition time of the DKI sequence was 16:24 min.

4.2.3.2. Quantitative evaluation

A quantitative comparison of the noise reduction algorithms is performed in this section including the evaluation of the following criteria:

- Noise reduction
- Structural similarity
- Peak-signal-to-noise ratio

Noise reduction rate (NRR)

For the methods considered, various smoothing parameters can be chosen that influence the results of the algorithms. The datasets were corrupted with Rician distributed noise at 25 % as explained in section 3.5.2.1. To evaluate the amount of noise suppressed, the standard deviation of the pixel values within two homogeneous regions (see figure 4.13) of the synthetic data of 35 $\times$ 35 pixels is measured in all the filtered volumes of the DKI acquisition and the average is compared to the mean noise in the original (noisy) volumes. Here the 30 th slice, that correspond to a middle slice, was considered for measurements. Accordingly, the noise reduction rate (NRR) in percent is defined as:

$$\text{NRR} = \left(1 - \frac{\sigma^{\text{denoised}}}{\sigma^{\text{original}}}\right) \cdot 100\% \tag{4.7}$$

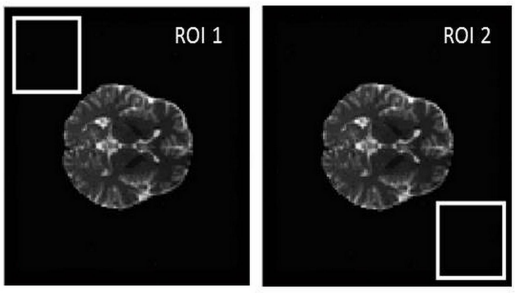

Figure 4.13.: Regions-of-interest (ROIs) selected for evaluation of the noise reduction rate.

In figure 4.14, the noise reduction rates for different approaches are plotted according to the two (regions-of-interest) ROIs. It can be seen for both ROIs that with the ADF method, more noise can be reduced. Besides, the amount of noise suppressed does not differ depending on the region considered for evaluation. No changes are observed in the ROIs depending on the filter used.

Mean structural similarity (MSSIM) index

In this work, the MSSIM index is used as a metric to quantitatively assess the overall quality of all denoised images resulting from the ADF and JaLMMSE noise correction schemes. The structural similarity (SSIM) index was proposed by Wang et al. [110] to measure fidelity (or similarity) between two images. The index is based on similarities of local luminance, contrast and structure between an initial uncompressed noise-free image and a distorted image. Wang et al. [110] proved that the SSIM index, when using as an image quality assessment metric, performs better than the mean squared error (MSE). In addition, unlike traditional image quality metrics, the SSIM index is consistent with human visual perception and its value varies conveniently between -1 and 1. The index is calculated between two corresponding regions (x and y) as the decomposition of three

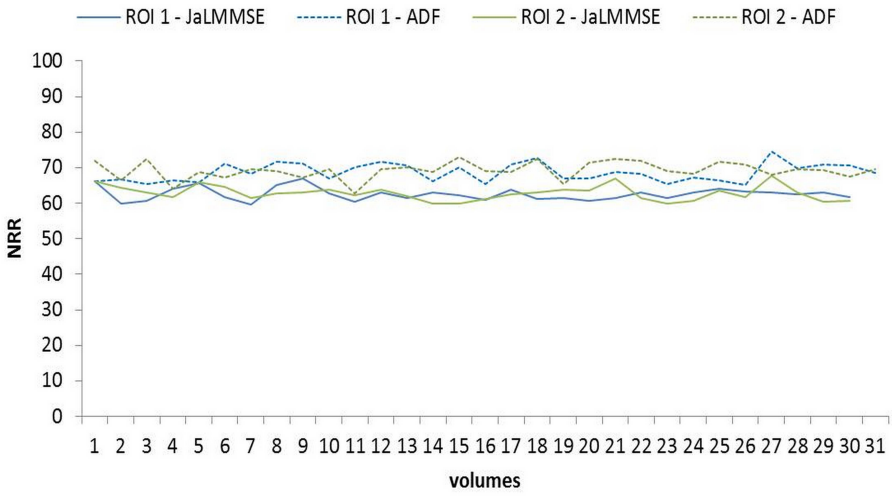

Figure 4.14.: NRR in the two ROIs (see figure 4.13) for the ADF and JaLMMSE approaches.

similarity measures: the similarity of brightness, contrast and structure. These three components can be combined to compute an overall similarity measure as [110]:

$$\text{SSIM}(x,y) = \underbrace{(\frac{2\mu_x\mu_y + C_1}{\mu_x^2\mu_y^2 + C_1})}_{\text{brightness}} \cdot \underbrace{(\frac{2\sigma_x\sigma_y + C_2}{\sigma_x^2\sigma_y^2 + C_2})}_{\text{contrast}} \cdot \underbrace{(\frac{\sigma_{x,y} + C_3}{\sigma_x\sigma_y + C_3})}_{\text{structure}} \tag{4.8}$$

where (μ_x, σ_x) and (μ_y, σ_y) are respectively, the pairs of mean and standard deviation (SD) of the two local regions, x and y, in the image. The value of $\sigma_{x,y}$ indicates the correlation between the x and y regions and the constants C_1, C_2 and $C_3 = \frac{C_2}{2}$ are used to avoid instabilities on each component of the SSIM index [110].

In this work, the constants C_1 and C_2 were chosen as $C_1 = (K_1L)^2$ and $C_2 = (K_2L)^2$, where $L = \max(I) - \min(I)$ is the dynamic range of the image I, and K_1 and K_2 were both set to 0.05. The local statistics, (μ_x, σ_x), (μ_x, σ_x) and $\sigma_{x,y}$ were computed within a local cubic window of 8 $\times$ 8 $\times$ 8 pixels [108].

$$\text{SSIM}(X,Y) = \frac{1}{N}\sum_{j=1}^{N} SSIM(x_j, y_j). \tag{4.9}$$

Here, X and Y are the reference and the source images, respectively; x_j and y_j are the image contents at the j-th local window; N is the number of voxels in the volume since the local cubic window moves voxel-by-voxel over the entire image volume. The value 0 and value 1 of the MSSIM index indicate zero correlation between images and high similarity between images respectively. The MSSIM value of the filtered vs. ideal data using the JaLMMSE was higher compared to the ADF method. Inconsistently MSSIM value of the filtered vs. noisy data using ADF is superior than when considering filtered vs. ideal data (see figure 4.15).

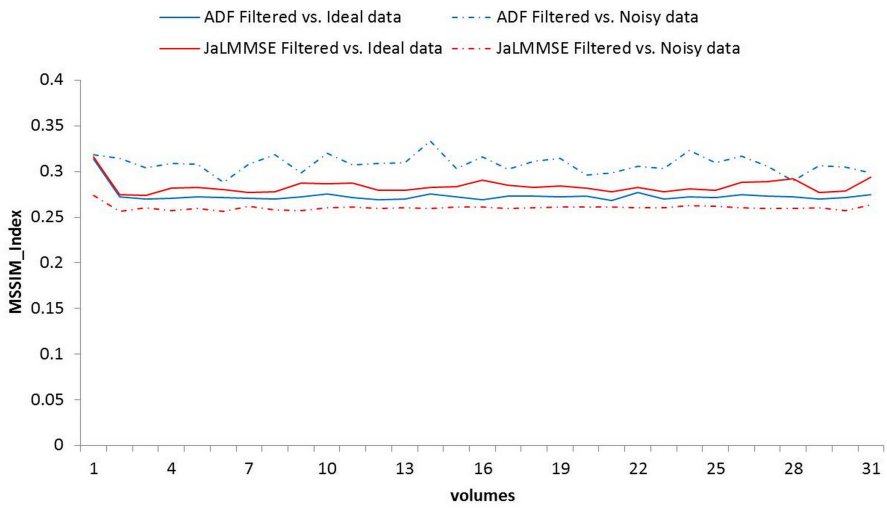

Figure 4.15.: MSSIM index respectively of the filtered vs. ideal volumes and the filtered vs. noisy volumes.

Peak-signal-to-noise ratio (PSNR)

The peak-signal-to-noise ratio (PSNR) can also be used to measure the difference between two images. It is defined as [110]:

$$\text{PSNR} = 20 * log10(b_{signal}/\text{rms}). \tag{4.10}$$

Here b_{signal} is the largest possible value of the signal. The root mean square difference between two images is rms. The PSNR in decibel units (dB) renders the ratio of the peak (maximum) signal and the difference between two images.

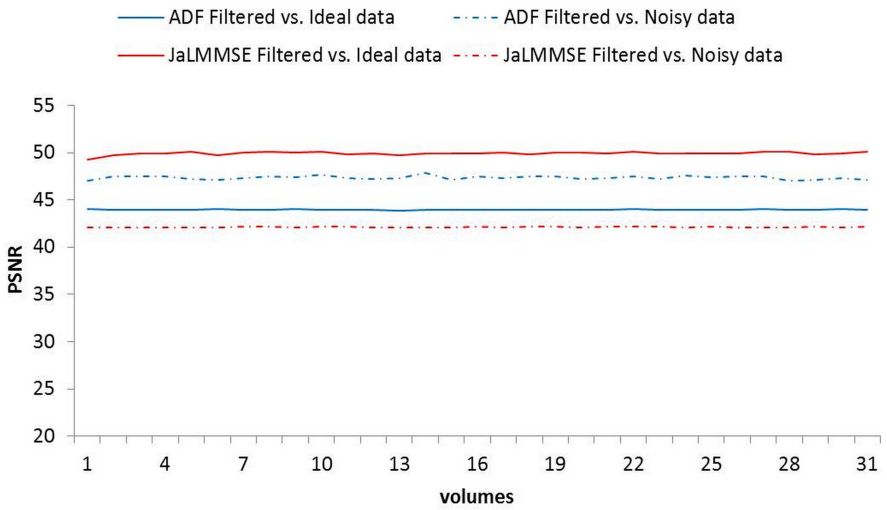

Figure 4.16.: PSNR respectively of the filtered vs. ideal volumes and the filtered vs. noisy volumes.

Experimental results of figure 4.16 shows that a maximum PSNR value of 50 dB is reached after filtering with JaLMMSE compared to 42 dB achieved with ADF when comparing the filtered to the

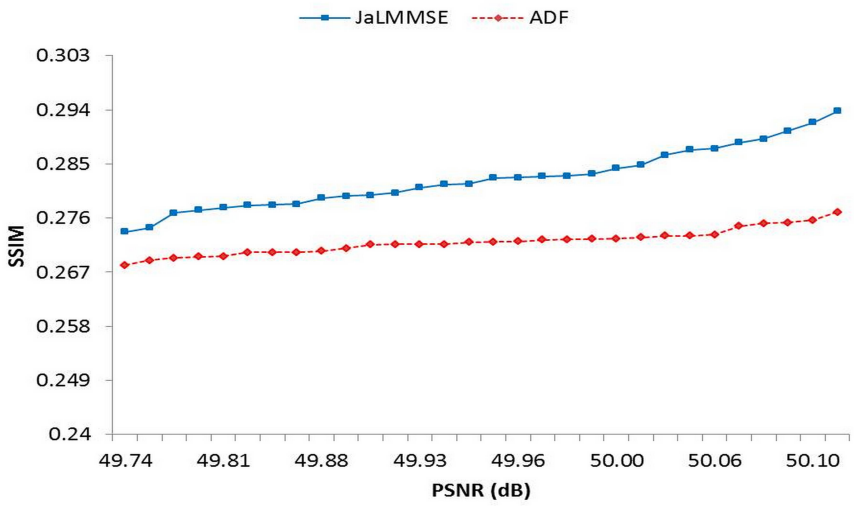

Figure 4.17.: SSIM index plotted against the PSNR values for all the volumes.

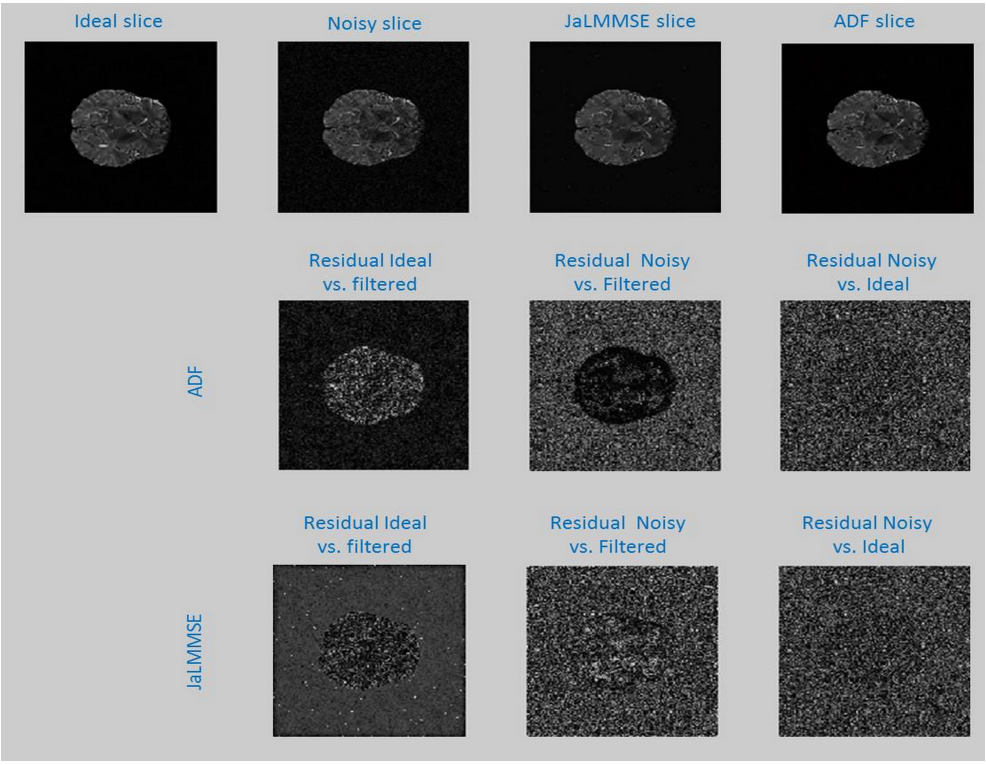

Figure 4.18.: Denoising results of different approaches for a brain slice displayed with the corresponding difference images.

ideal data. Comparing the filtered and noisy volumes PSNR with the JaLMMSE method was lower as expected regarding to the PSNR of the filtered vs. ideal volumes. This comparison revealed inconsistencies as with the MSSIM regarding the ADF method. These might be due to the fact that the filter reduces more noise but is blurring the edges therefore totally changing the structure of the image.

Plotting the MSSIM against the PSNR in figure 4.17 shows the superiority of using the joint information in DWI channels for filtering compared to an edge preserving filter.

In figure 4.18, an example slice taken from the brain volumes is shown. The original slice showed noise due to the low SNR. At first glance, the results of the filtering with the JaLMMSE and the ADF methods look quite natural. In the images denoised, there is no visual difference detectable leading to the conclusion, that the two filters removed noise uniformly in the DWI scans preserving edges and structures. To obtain an impression about how well the structures were preserved by the different filtering schemes, difference images from the denoised and the original noisy scans were generated. Considering the filtering process in the ADF method, the structure is present in the difference images, meaning that the edges are not well preserved with the filtering process on projections; with the structure being destroyed. However, the difference images resulting from the filtering with the JaLMMSE technique show that more of the noise structures are removed without affecting the structure and quality of the edges.

4.2.3.3. Visual inspection on real data

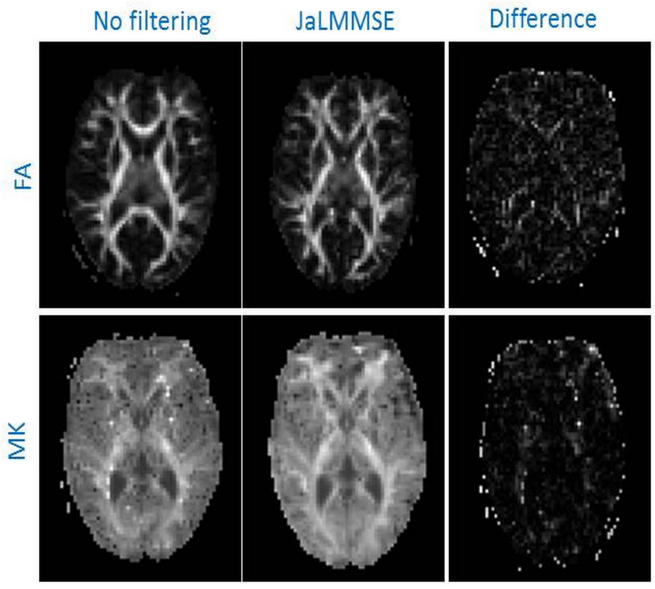

Figure 4.19.: Denoising results of the JaLMMSE approach on real brain data displayed with the corresponding difference images.

Real DWI images of the brain acquired with the protocol described in 4.2.3.1 were filtered prior to DKI computation. For comparison the DKI results with and without filtering using the JaLMMSE filter are shown on figure 4.19. The figure shows improvement of the mean kurtosis (MK) map and fractional anisotropy (FA) map after the filtering process with the JaLMMSE approach.

As a general result, applying noise reduction filters on DWI volumes prior to DKI estimation is

necessary. Even if the anisotropic filter could show a stronger reduction of noise when analysing the NRR, it lost each comparison with the JaLMMSE regarding the MSSIM and PSNR measures. Using the JaLMMSE method to filter synthetic DWI images, structures and edges were better preserved compared to the use of ADF. With respect to these observations, the JaLMMSE method was preferred to filter real DWI images prior to DKI computation.

4.3. Development of an image processing pipeline for the evaluation of the clinical added values of DKI

4.3.1. Image processing pipeline

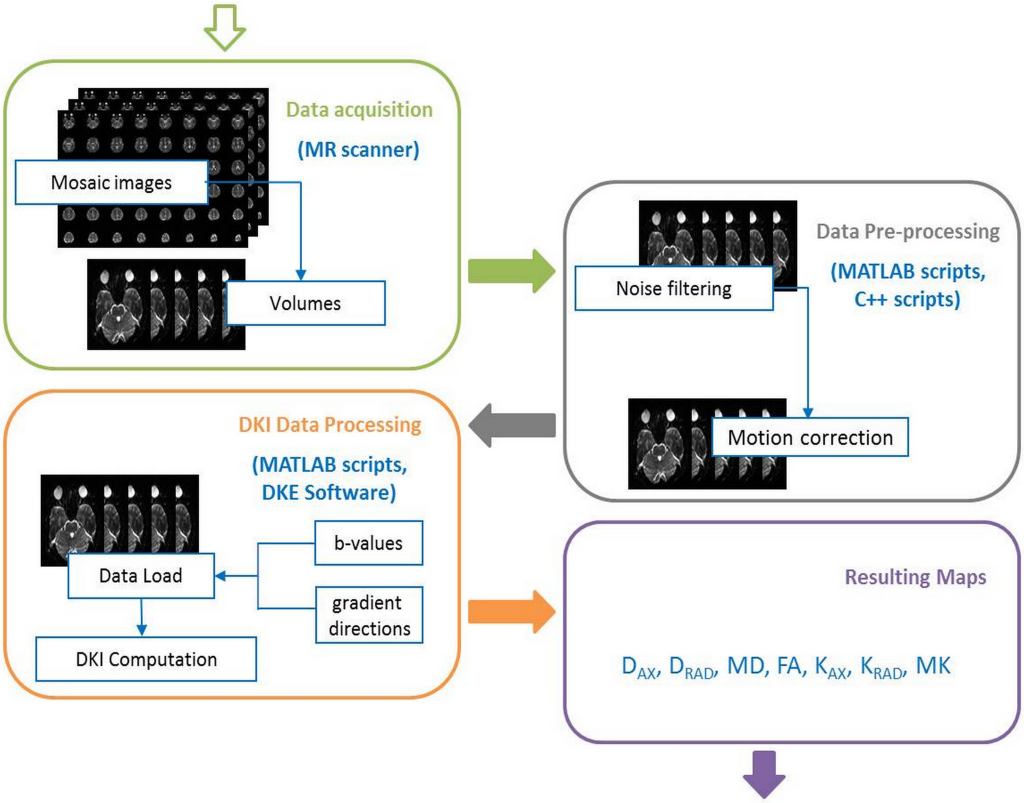

Figure 4.20.: DKI Image Processing.

The block diagram of the resulting image processing pipeline is shown in figure 4.20. A first conversion step is necessary depending on whether the images are in mosaic format or not, followed by the conversion in NIfTI. These two steps are optional and can be skipped if not needed. In this thesis, the use of the Siemens Scanner made this step necessary. In the next processing step, the image volumes are optionally filtered for Rician noise removal with the JaLMMSE approach. Then, the filtered volumes are corrected for motion elimination using a MI based similarity measure. For more details about the pre-processing techniques used, please refer to sections 4.1 and 4.2. After this pre-processing step, the DKI computation is done to produce the MD, FA, D_{AX}, D_{RAD}, MK, K_{AX}, K_{AX} maps. For the DKI estimation, MATLAB scripts that are

introduced later in section 4.3.2.2 and the DKE software published by Tabesh et al. [51] are used. Finally, the pipeline was implemented in-house developed softwares based on Microsoft® Visual C^{++} 2003 - 2010 with the Microsoft Foundation Classes (MFC) for the C++ scripts and based on the MATLAB environment (http://www.mathworks.com) when using the MATLAB scripts presented in section 4.3.2.

4.3.2. DKI data processing

4.3.2.1. Constrained linear least square Fitting for DKI computation

Many least square approaches as the ULLS and the CLLS exist in the literature to fit the diffusion tensor (D_T) and the kurtosis tensor (K_T) [51]. CLLS stands for constrained linear least squared and describes the mathematical formulation of the DW signal modelling under physically and biologically plausible boundary conditions. These constraints result from the underlying geometry of the relevant biological tissues that restricts directional physically true kurtosis [6]. Although it is well known that theoretically, the minimum possible kurtosis should be -2, multi-compartment diffusion models, as for example the bi-exponential model (see 3.4.1.1), and empirical evidence in brain investigations, suggest a purely Gaussian displacement distribution with a minimum kurtosis value $K_{\text{min}} = 0$ [6]. Even if the acquired signal $S(\mathbf{n}, b)$ considering the direction vector **n** should happen to be an increasing function of the b-value in some experiments setting, previous studies affirm that this has never been the case for biological tissues [51]. This explains the necessity to require that the estimated diffusion signal S be a strictly decreasing function of the b for all $\mathbf{n} \in \mathbf{N}$ in medical settings. A maximum kurtosis value of $K_{\text{max}} = 3$ ensures that this condition is fulfilled in the range of b-values used for data acquisition.

In this algorithm, to ensure the physical and biological plausibility of the results, Tabesh et al. [51] introduces two constraints related to the observations mentioned above. The diffusivity should always be positive to ensure kurtosis values between 0 and 3. From equation (3.23) introduced in chapter 3, he formulates an estimation problem for the CLLS approach as follows [51]:

$$\text{minimise } \|\mathbf{AX - B}\|^2 \text{ such that } \mathbf{CX} \leq \mathbf{d}, \tag{4.11}$$

with the objective to determine the elements of the diffusion tensor $\mathbf{D_T}$ and the kurtosis tensor $\mathbf{K_T}$. Here the right-hand side of equation (3.23) should match its left-hand side, respecting the constraints formulated above. **A** is a matrix containing the set of non-zero b-values and gradient directions used during the acquisition. **X** is a 21×1 vector with the unknowns (the 6 independent elements of $\mathbf{D_T}$ and the 15 independent elements of $\mathbf{K_T}$). **B** is the vector of signal attenuation $\ln(\frac{S}{S_0})$ measured in the different directions.

The problem defined by (4.11) can be addressed using two classes of algorithms that are rather standard: the quadratic programming algorithm (CLLS-QP) and the heuristic algorithm (CLLS-H). Here the labels QP and H stand respectively for quadratic programming and heuristic. These methods are described here as published in a recent work of Tabesh et al. [51]. In this thesis the DKE software can be used with the CLLS-QP computationally more expensive but also more accurate method. The CLLS-QP was preferred compared to the CLLS-H as more emphasis was laid on accuracy regarding to the computation time.

In the CLLS-QP, depending on whether it exists or not, a feasible point is used to initialise the algorithm. The definition of Tabesh et al. [51] is considered in this work and a feasible point is defined as one for which the constraints are true. It is calculated with linear programming. In the implementation of Tabesh et al. [51] considered during this work, in a first step, the feasible

point is set to be the unconstrained linear least square (ULLS) solution of equation. This point is also set as final solution of the CLLS problem if it respects the constraints. If not, a feasible point computed using linear programming, as mentioned above, is used to initialise the computation. In a second step, the final feasible point is found through iterations. Please note that the constraints are also updated at each iteration.

4.3.2.2. Software implementation

DKI maps in chapter 6 were produced using in-house developed MATLAB programs adapted from the work of Tabesh et al. [51] as presented below. Results of chapters 5 and 7, were produced with the DKE software introduced in section 4.3.2.2 because of its more user-friendly graphical user interface (GUI).

DKI maps calculation with MATLAB scripts

Before the introduction of the DKE software with a GUI, the DKI maps from a given DW MRI dataset were computed in this thesis using modified MATLAB scripts with the fitting method with CLLS-QP based on [51]. For a standard DW acquisition, the data are organised to follow the folder structure shown in figure 4.21 and given later as input of the MATLAB function.

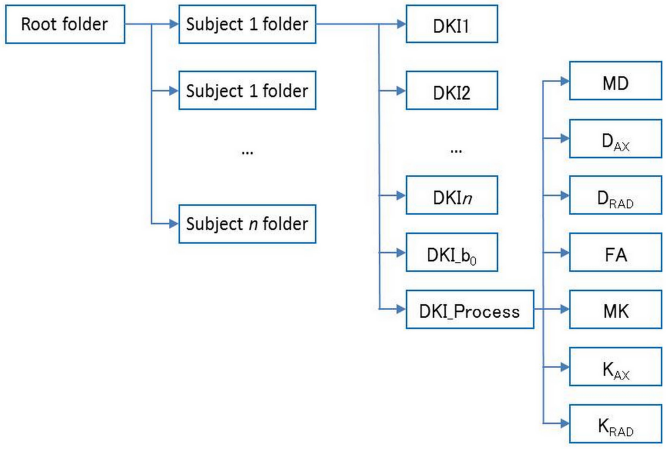

Figure 4.21.: Folder structure for study data.

Folders DKI1, DKI2, DKIn and DKI-b_0 respectively contain the DICOM image data of the first, second and n^{th} DKI series[3], and additional $b = 0$ acquisitions, where n is the number of series. Once processing is complete, the parametric maps in NIfTI format are stored in the folder DKI-Process.

The MATLAB function *dki_process(basedir, options)* receives the basic folder of a subject n (see figure 4.21) with some processing parameters (image format, number of averages, extra b_0 images or not, non-zero b-values, number of gradient directions) as input and plots the DKI maps as output. For processing, the pipeline showed in figure 4.21 is used.

Depending on the data being processed (e.g. brain or kidney data), a background threshold T is optionally set on the $b = 0$ image to accelerate the computation. . Only voxels with $b = 0$ values above T are processed. In this thesis for brain studies, T was set to 70 and for kidneys

[3] also number of averages, or number of acquisitions

$T = 0$ was used. Regarding the constraints formulated in section 4.3.2, the threshold of the final kurtosis maps are set ($K_{\text{min}} = 0$, $K_{\text{max}} = 3$). The kurtosis tensor is then calculated using the *dki_method* and considering the constraints violations (see code 4.2). Depending on whether or not the method is being initialised for a feasible point, the ULLS or CLLS are set with the *dki_method.linear_constrained* variable (refer for more details to section 4.3.2.1). Following the kurtosis estimation, the diffusion tensor is estimated using the *dti_method*. The script also allows either only a DKI or a DTI computation if necessary. For DTI computation, the set of non-zero b-values used can be specified with the *dti_method.b_value* variable with the corresponding gradient directions through the *dti_method.directions* variable. A **.dat* file can be used to specify the set of gradient directions under consideration. For the studies presented in this work, this set varied from 20 to 30 directions for brain and kidney applications. Finally the output files are specified and the diffusion maps are calculated and stored for plotting.

Listing 4.2: DKI / DTI maps estimation exemplary for brain applications.

```
function dki_calculation(dir, opt)
...

% ------------------------------------------------------------------
% Setting the parameters for DKI fitting
% ------------------------------------------------------------------
% Unconstrained (0) or constrained (1) algorithm
dki_fit.linear_constrained = 1;

% Generate maps of constraint violations
dki_fit.linear_violations = 1;

% Intensity of each voxel represents the proportion
% of constraints on directional diffusivities and
% kurtoses violated by the ULLS solution (default: 0)
% For more details see paper of Tabesh et al. [57]
% ------------------------------------------------------------------
% Setting the parameters for DTI fitting
% ------------------------------------------------------------------
% Flag set to (1) means DTI and (0) no DTI computation
dti_fit.dti_flag = 1;

% DTI and DKI computation (0) or only DTI (1)
dti_fit.dti_only = 0;

% Unweighted (0) or weighted (1) linear least-squares
dti_fit.linear_weighting = 1;

% Vector of non-zero b-values for DTI computations
dti_fit.b_value = 1000;

% Array of gradient directions for the non-zero
% b-values used in DTI computations
dti_fit.directions{1} = 1:ndir;
```

```
% ------------------------------------------------------------
% Diffusion gradient directions
% ------------------------------------------------------------
% Gradient vector table
fn_gradients = 'gradient_vectors_TimTrio30_Brain.dat';

% Indices of gradient directions for DKI computations
% for first non-zero b-value
idx_gradients{1} = 1:ndir;
% Indices of gradient directions for DKI computations
% for second non-zero b-value
idx_gradients{2} = 1:ndir;

...
end
```

The Diffusional Kurtosis Estimator (DKE) software

Another possibility to produce DKI maps is to use the DKE software. In this thesis, results of chapter 5 and chapter 7 are produced with DKE Version 2.5.1. DKE is a program for the post-processing of diffusional kurtosis imaging (DKI) datasets. It allows the pre-processing of DW images (convert, co-register, and combine) and estimation of the diffusion parametric maps for datasets acquired on Siemens scanners and can be seen as a GUI of the Matlab scripts presented in the previous section.

Chapter 5

Construction of a whole brain atlas on the basis of magnetic resonance diffusion tensor and diffusion kurtosis data: Age and gender related study

Understanding biological tissue microstructure and its alteration process through human brain atlases is important for brain research. The normalised data of healthy individuals in an atlas may help to identify common anatomical structures usable as standard references. Brain atlases also play an obvious role in the quantitative assessment of typical patterns and variation of measures in the "average" healthy [111] as well as unhealthy brain. This in turn establishes a solid base for testing voxel-based as well as region-of-interest (ROI)-based statistical hypotheses. Actually, one of the most used atlases in the literature is the Tailarach coordinate system [112]. Even though it was constructed using the histology data of only one single subject, it has been widely used in previous reports for identification, registration, and report of human cortical locations in a common coordinate system since its completion with cyto-architectural information of the cortex present in Brodmann's map [113]. In addition to the Tailarach coordinate system other relevant probabilistic maps were introduced by the Montreal Neurological Institute (MNI) [114, 115] and the international Consortium of Brain Mapping (ICBM) [116]. To create these maps, a large number of MR images of healthy subjects were linearly registered into a common template. These maps work well for normalisation-based group analyses [117]. New imaging methods as Diffusion-Weighted Imaging (DWI), Diffusion Tensor Imaging (DTI) or Diffusion Kurtsosis Imaging (DKI) techniques introduced in chapter 3 can provide additional diagnostic or (micro-) structural information. Therefore the need of brain atlases containing these new information is crucial.

Reporting registered DKI data across normal subjects into an atlas can reliably identify common anatomical structures and provide a standard reference of DKI indices to increase diagnostic confidence. Previous efforts reporting kurtosis regional values in the healthy brain focussed on predefined regions as the pre-frontal brain cortex [10]. A more recent study of Lätt et al. [118] presents kurtosis indices in a thin slab of 27 slices in healthy brains. Thus, the purpose of this chapter was to develop a human whole brain age-dependent atlas of diffusion tensor and diffusion kurtosis indices in healthy volunteers and to evaluate their variability mapped to the

existing well-established anatomical MNI space.

5.1. Data acquistion

Eighty-five healthy volunteers without neurological complaint, history of past head injury or any history of neurological or neuro-psychological diseases or previous neurosurgery, diabetes and other type of disorder that could possibly affect the central nervous system, epilepsy, hypertension, migraine (44 males and 41 females), whose ages ranged from 21 – 69 years (males, 21 – 67; females, 21 – 69), with mean age of 40.27 $\pm$ 15.62 (males, 38.46 $\pm$ 15.97; females, 41.26 $\pm$ 15.53) were enrolled in this study. The review board of the institution validated the study and all the volunteers signed an information consent before examination. The ANOVA tests on age distribution of females and males showed no statistical significant difference ($p > 0.05$). In addition, a radiologist with more than 5 years' experience reviewed all the acquired images of all subjects to identify any relevant structural abnormalities or pathology. Participants were grouped in 10-year increments in five age groups from 20 years through the age of 69 years: 20YG (mean age 22.46 $\pm$ 1.05; range 21 – 29 years), 30YG (mean age 33.31 $\pm$ 2.10; range 31 – 36 years), 40YG (mean age 45.90 $\pm$ 3.41; range 41 – 48 years), 50YG (mean age 54.38 $\pm$ 2.79; range 51 – 59 years), 60YG (mean age 64.38 $\pm$ 2.26; range 61 – 69 years). In each age group, the number of participants was fixed to 13. The 20- and 30-year groups (mean age 26.93 $\pm$ 4.83, range 21 – 36) were merged and used to compute the principal atlas [119]. For the principal atlas additional 20 volunteers were acquired such that a total of 46 volunteers were considered in this group. Repeated scans of three participants imaged at different dates were acquired and used for reproducibility measurements.

All the MRI examinations were performed on a clinical 3T MRI scanner (Magnetom Trio A TIM System; Siemens Medical Systems, Erlangen, Germany) using a 12-channel head coil. DKI data were acquired using a single-shot Spin Echo Planar Imaging (SSEPI) sequence in the axial plane using 3 b-values (0, 1000, 2000 s/mm^2) and 30 diffusion encoding directions. A volume of 60 slices covering the entire brain without gaps was acquired thus enabling the assessment of a wide range of anatomical regions in the atlases. Further imaging parameters were as follows: echo time (TE) $=$ 101 ms, repetition time (TR) $=$ 8100 ms, matrix $= 92 \times 92$, field of view (FOV) $=$ 230 mm, number of averages = 2, reconstructed image resolution $= 2.5 \times 2.5 \times 2.5$ mm^3. generalised auto-calibrating partially parallel acquisition (GRAPPA) as a parallel imaging method was used accelerated by a factor of 2. The mean acquisition time of the DKI sequence was 16:24 min. Additionally, a high-resolution 3D T_1-weighted magnetisation Prepared Rapid Gradient Echo (MPRAGE) sequence for anatomical reference was obtained with the following parameters: TE $=$ 2.98 ms, TR = 2300 ms, FOV $=$ 256 mm, 1 mm slice thickness and matrix $= 256 \times 256$. The scan time for this sequence was 04:08 min.

5.2. Data analysis

For further analyses, the DW images were transferred to a workstation running a Windows 7 platform for motion correction. Details about this correction driven by an in-house developed mutual information based motion correction algorithm [120] were already introduced in section 4.1 The coregistered DKI datasets were then filtered using the JaLMMSE filter (see section 4.2)

The estimated tensors were utilised to determine the diffusion and kurtosis measures for each subject corresponding to the parameters mean diffusivity (MD), fractional anisotropy (FA), mean kurtosis (MK), axial kurtosis (K_{AX}) and radial kurtosis (K_{RAD}) as introduced in chapter 3 .

5.2.1. Normalisation

The b_0 ($b = 0$ s/mm^2) images of each subject were normalised to the ICBM-152 T_2 brain template that is based on T_2-weighted maps of 50 normal young adult brains [116] in the MNI space. The entire normalisation process was performed using the Advanced Neuroimaging Tools (ANTs) software based on symmetric normalisation as a transformation model and mutual information as similarity measure [73]. ANTs is using a diffeomorphismus based registration resulting in precise normalisation compared to other common normalisation techniques [73, 121]. The resulting transformation matrix of the b_0 image normalisation for each subject was then applied to the other parameter maps (MD, FA, MK, K_{AX}, and K_{RAD}). The final dimensions of the b_0, MD, MK, K_{AX}, and K_{RAD}, were 91 $\times$ 109 $\times$ 91 voxels, and the final voxel size was 2.0 $\times$ 2.0 $\times$ 2.0 mm^3 that correspond to the resolution of the MNI atlas.

5.2.2. Measurement of normalisation accuracy

Data from ten randomly selected subjects were used to evaluate the normalisation quality by assessing the accuracy in matching different brain structures between subjects [122]. For that purpose, thirty anatomical landmarks (12 in the axial planes, 12 in the sagittal planes and 6 in the coronal planes) were manually selected on prominent brain structures in the b_0 images using DiffeoMap (www.mristudio.org, Version 1.9) [123] (see figure 5.1). These landmarks were placed on the normalised datasets of one subject that served as reference template. The same landmarks were copied on the normalised datasets of the other subjects and moved to the corresponding structures. Displacements (i.e., landmark displacement) of the i^{th} landmark defined on the reference template, and moved to a new location in the subject brain were measured to quantify normalisation quality. The minimum, maximum, mean and standard deviation (SD) values of the landmark displacement in the b_0 images over all the subjects were estimated. The landmark coordinates used are listed in the table .1 in section A in the appendices.

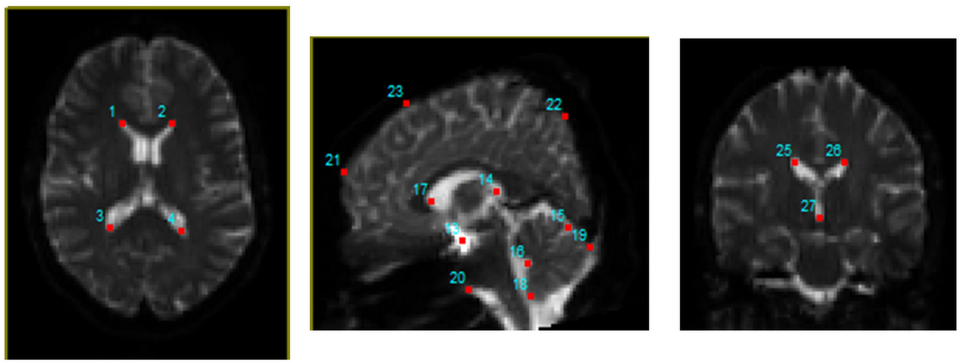

Figure 5.1.: Representation of some landmarks in the axial, sagittal and coronal planes. Altogether 30 were considered.

5.2.3. Regional analyses

After assessing the accuracy of registration, 23 anatomically relevant structures in the brain (see figure 5.2) were delineated with manual drawn ROIs of 7 to 50 pixels: internal capsule anterior (ALIC), basal ganglia, caudate, body of corpus callosum (CCb), genu of corpus callosum (CCg), splenium of corpus callosum (CCs), centrum semiovale (cent. sem.), cerebral peduncle (cereb.

ped.), cingulate, cingulate temporal (cing. temp.), corona radiata, cortex, external capsule (ext. caps.), Fornix, frontal white matter (FWM), mesencephalom (mesenc.), palladium, internal capsule posterior (PLIC), pons, putamen, parietal white matter (PWM), thalamus and temporal white matter (TWM). Reliably identifiable ROIs with the least possible partial volume effects were drawn on b_0 images in all subjects. ROIs on b_0 images were copied onto the corresponding position of the other maps of each subject. For each ROI, the mean value of the diffusion parameter was extracted to construct the atlas. For each bilateral structure a single value was produced by averaging the values of the left and the right ROI. For singular structures, a single ROI average was used.

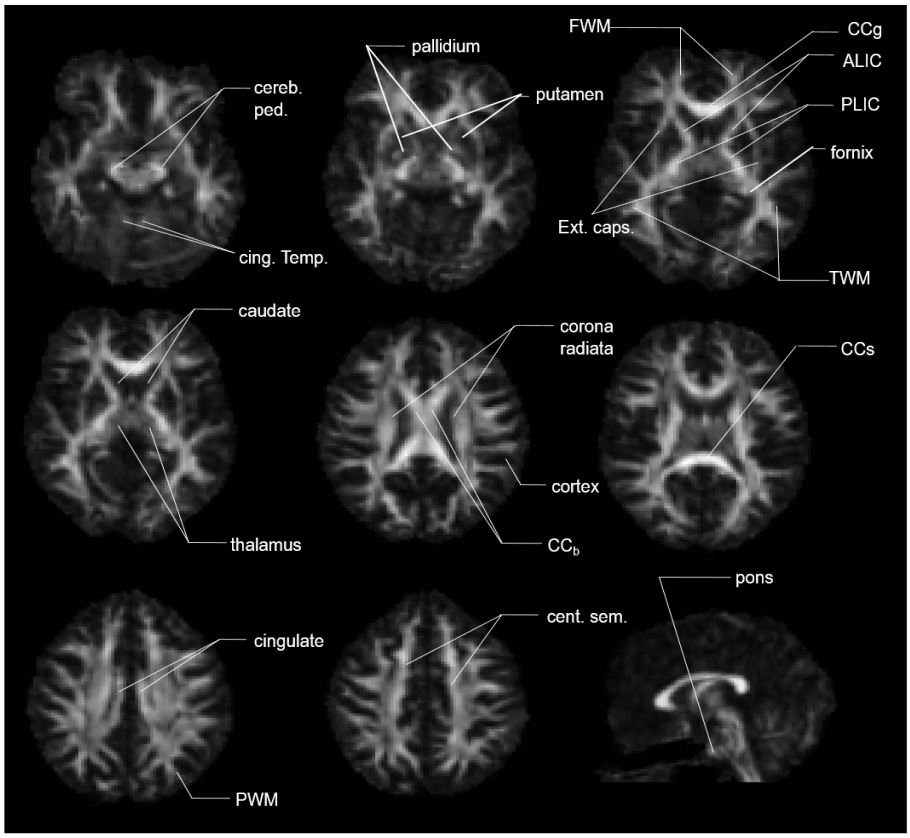

Figure 5.2.: Brain regions selected showed on a representative fractional anisotropy (FA) map of a 22-years old volunteer.

5.2.4. Measurement error

Intra-subject reproducibility and inter-observer variability of FA and MK values were examined using the free hand ROI technique [57]. Intra-subject reproducibility analysis was based on data of three volunteers (mean age: 24.83 $\pm$ 3.31, range 22 – 29 years, 1 male, 2 females) imaged on two different dates. The interval between the first and second MRI acquisitions of each volunteer was not less than two weeks. In the ROIs, the FA and MK values of the first MRI acquisitions from the 3 volunteers were assessed and compared to the values obtained from the second MRI acquisitions. For the inter-observer variability, two independent observers were instructed to independently place the ROIs in the first MRI acquisitions of the three volunteers. Resulting values from the first

and second observers were compared.

5.2.5. Construction of the whole brain atlas

High-resolution atlases of MD, FA, MK, K_{AX}, K_{RAD} were created as maps of mean and SD of the normalised data of each subject for the five age groups and additionally for the 20-, and 30-year group merged together to form the principal atlas.

5.2.6. Statistical analysis

Statistical tests were performed using the statistics toolbox in MATLAB (Version: 8.0.0.783 (R2012b)). All data are expressed as mean $\pm$ SD. For all tests statistical values of $p \leq 0.05$ were considered to indicate a statistically significant difference. The reproducibility measurements were compared using a two-sided, paired-samples Student's t-test and Bland-Altman plots. The difference versus the mean of the DKI parameters of the repeated measurements is plotted.

5.2.6.1. Age and gender dependency

With linear regression [124], age as well as gender influences of all diffusion measures was tested in all the ROIs. The correlation coefficient R was used to describe the correlations between diffusion measurements. In addition, analysis of variance (ANOVA) among the 20-, 30-, 40-, 50-, and 60-, year groups was examined.

5.3. Results

In 80 of 85 subjects the DKI measurement could be acquired in sufficient image quality. In five subjects the data were discarded due to subject movement, incidental findings or technical problems. Therefore, 80 healthy volunteers were included in the DTI and DKI analyses. Figure 5.3 shows a representative transverse slice through the brain of a 22-years old volunteer after registering it into the MNI space. Both MK and K_{RAD} had high tissue contrast between the white matter (WM) and the gray matter (GM) similar to FA. However, the contrast was more pronounced on the FA map compared to MK.

5.3.1. Measurement of normalisation accuracy

Analysing how accurate the different brain structures between the subjects matched after the normalisation resulted in the measures shown in figure 5.4 and figure 5.5. The average distance between the landmarks coordinates of the reference and individual brains was approximately 0.71 mm on $b = 0$ s/mm^2 images. For 73 % of all the landmarks selected in all the subjects, the distance was less or equal to 1 mm, for 86 % of all the landmarks this boundary was 2 mm or less and for 100 % of the landmarks 4 mm or less was recorded (see table .2 in section A of the appendices).

5.3.2. Regional analyses

Examples of the mean b_0 image and mean DKI maps over participants of the principal atlas (20YG and 30YG) after normalisation are shown in figure 5.6. Most visible structures in the individual subjects' brain structures (see figure 5.3) before the normalisation process were preserved on the

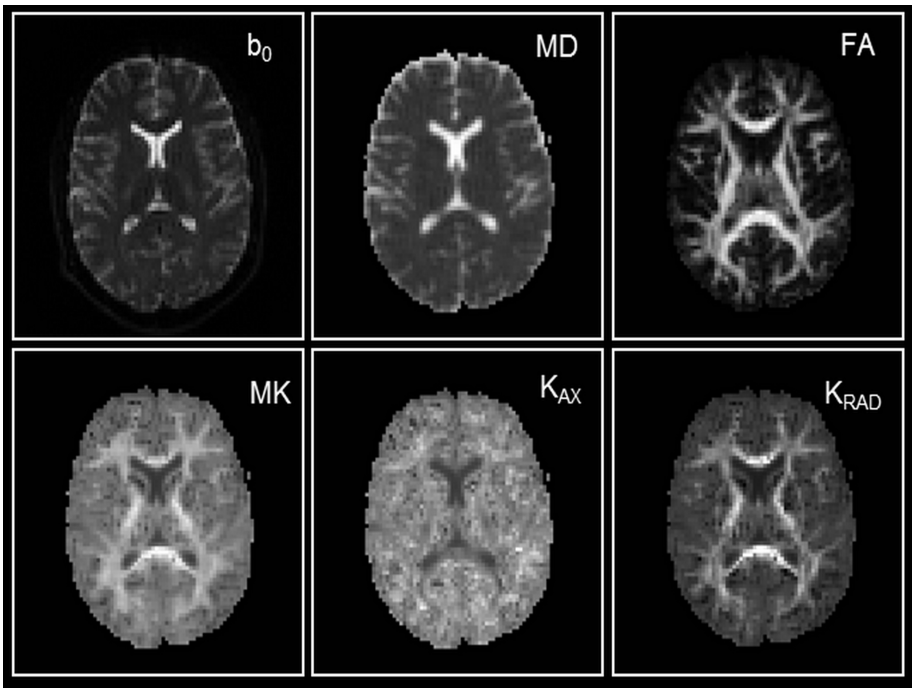

Figure 5.3.: Maps of diffusion-weighted (DW) measures of a 22-years old volunteer shown for one axial slice. EPI non-diffusion-weighted image (b_0), mean diffusivity (MD), fractional anisotropy (FA), mean kurtosis (MK), axial kurtosis (K_{AX}), radial kurtosis (K_{RAD}).

normalised maps after averaging. FA and MK values exhibited regional difference among 20-, 30-, 40-, 50-, and 60-YG. (All these tables are provided in section B of the appendices). In the principal atlas (see table 5.1), MD varied from 0.69 $\pm$ 0.04 μm^2/ms to 0.92 $\pm$ 0.15 μm^2/ms, FA from 0.13 $\pm$ 0.04 to 0.80 $\pm$ 0.05, MK from 0.71 $\pm$ 0.05 to 1.76 $\pm$ 0.31, K_{AX} from 0.65 $\pm$ 0.05 to 1.17 $\pm$ 0.25 and K_{RAD} from 0.78 $\pm$ 0.22 to 2.57 $\pm$ 0.31. MK and FA correlated positively with $R = 0.85$, $p < 10^{-6}$. Neither MK nor FA correlated with MD ($R = 0.02$, $p = 0.48$ and $R = -0.03$, $p = 0.53$, respectively).

WM regions with high a high amount of myelin with homogeneous orientation, such as the splenium of corpus callosum (CCs), 0.80 ± 0.05 and internal capsule posterior (PLIC) , 0.61 ± 0.05 showed relatively high FA values. In contrast, the putamen had relatively lower FA values 0.15 ± 0.02. This effect was much more pronounced on MK maps with values of 1.76 ± 0.31, 1.17 ± 0.13, 0.96 ± 0.20 for the CC, PLIC and putamen respectively. Exemplary data of a 20YG- and a 60YG-volunteer are shown on figure 5.7.

5.3.3. Measurement error

Respectively exemplary for the cortex, CCs, FWM, thalamus, putamen and pons, the globally measured mean [5] $FA_{FirstObs/FirstMeas}$ was 0.21 $\pm$ 0.07; 0.76 $\pm$ 0.07; 0.42 $\pm$ 0.07; 0.26 $\pm$ 0.04; 0.12 $\pm$ 0.05 and 0.35 $\pm$ 0.08, the mean $FA_{FirstObs/SecondMeas}$ 0.24 $\pm$ 0.07; 0.78 $\pm$ 0.07; 0.40 $\pm$ 0.06; 0.28 $\pm$ 0.03; 0.14 $\pm$ 0.04 and 0.39 $\pm$ 0.07, and the mean $FA_{SecondObs/FirstMeas}$ 0.3 $\pm$ 0.08; 0.79 $\pm$ 0.07; 0.40 $\pm$ 0.09; 0.25 $\pm$ 0.03; 0.11 $\pm$ 0.05 and 0.36 $\pm$ 0.07. The first and second FA measurements of the first observer ($p = 0.74$) and the measurements of the second observer ($p = 0.71$) were not significantly different. In the principal atlas, the measured mean $MK_{FirstObs/FirstMeas}$

[5] *Obs*: observer; *Meas*: measurement.

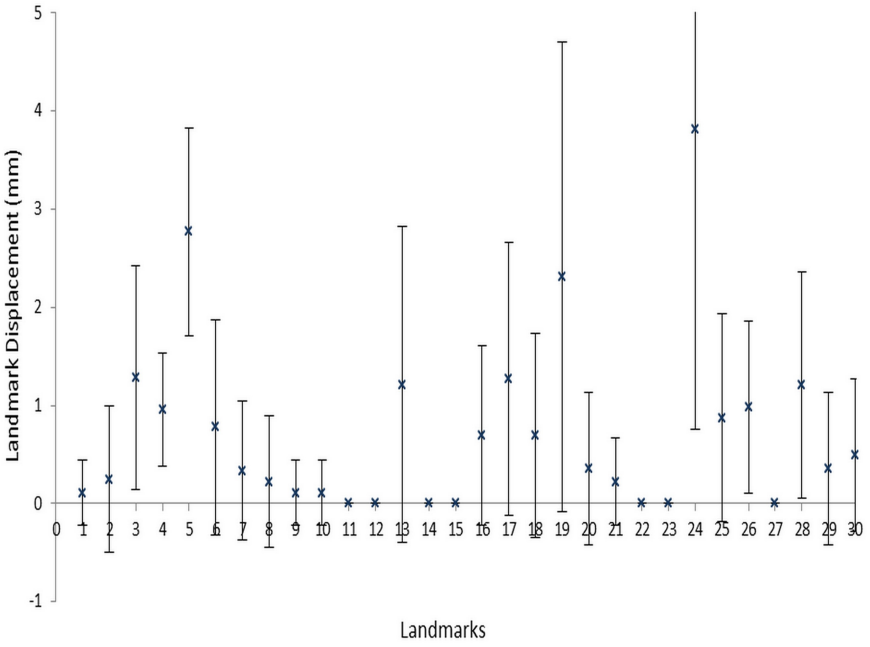

Figure 5.4.: Mean deviation of the individual landmarks (1 to 30) from the reference brain for all the subjects with respective SD in mm. For more details, please see table .2 in section A of the appendices.

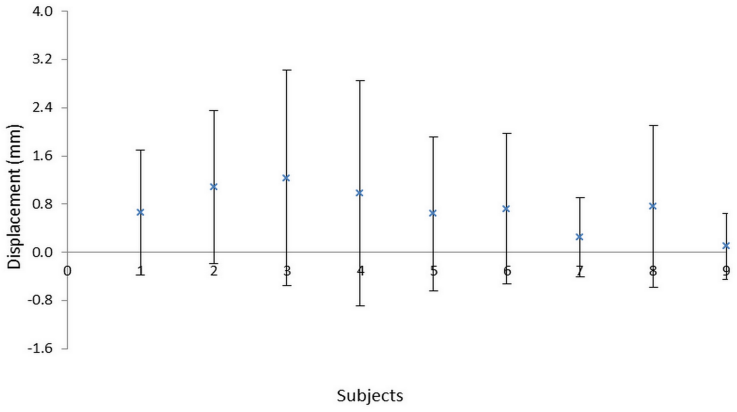

Figure 5.5.: Mean deviation of the landmarks for the individual subjects (1 - 9) with SD in mm. Subject 0 is reference.

Table 5.1.: Resulting atlases respectively for the merged Groups.

Merged Groups	MD $[\mu m^2/ms]$	FA	MK	K_{AX}	K_{RAD}
ALIC	0.72 ± 0.04	0.47 ± 0.05	1.02 ± 0.09	0.96 ± 0.09	1.36 ± 0.20
Basal Ganglia	0.74 ± 0.11	0.32 ± 0.07	1.11 ± 0.17	1.03 ± 0.16	1.26 ± 0.23
Caudate	0.87 ± 0.14	0.13 ± 0.04	0.77 ± 0.18	0.78 ± 0.18	0.78 ± 0.22
CCb	0.92 ± 0.15	0.64 ± 0.06	1.22 ± 0.19	0.90 ± 0.16	2.08 ± 0.38
CCg	0.86 ± 0.08	0.74 ± 0.06	1.56 ± 0.25	1.05 ± 0.19	2.47 ± 0.39
CCs	0.78 ± 0.11	0.80 ± 0.05	1.76 ± 0.31	1.17 ± 0.25	2.57 ± 0.31
Cent. Sem.	0.71 ± 0.02	0.50 ± 0.04	1.14 ± 0.06	1.00 ± 0.06	1.59 ± 0.19
Cereb. ped.	0.75 ± 0.08	0.69 ± 0.04	1.49 ± 0.22	1.07 ± 0.19	2.20 ± 0.37
Cing. temp.	0.73 ± 0.06	0.45 ± 0.07	1.18 ± 0.10	1.05 ± 0.14	1.78 ± 0.37
Cingulate	0.71 ± 0.08	0.37 ± 0.06	1.05 ± 0.16	1.01 ± 0.13	1.16 ± 0.41
Corona Rad.	0.69 ± 0.04	0.57 ± 0.05	1.27 ± 0.07	0.99 ± 0.13	1.77 ± 0.16
Cortex	0.84 ± 0.13	0.24 ± 0.07	0.86 ± 0.13	0.83 ± 0.11	0.96 ± 0.20
Ext. caps.	0.72 ± 0.05	0.54 ± 0.06	1.02 ± 0.13	0.94 ± 0.11	1.51 ± 0.29
Fornix	0.75 ± 0.05	0.25 ± 0.06	0.71 ± 0.05	0.65 ± 0.05	0.80 ± 0.08
FWM	0.73 ± 0.03	0.42 ± 0.04	1.08 ± 0.11	0.95 ± 0.08	1.32 ± 0.19
Mesenc.	0.80 ± 0.10	0.39 ± 0.04	1.23 ± 0.11	1.06 ± 0.10	1.49 ± 0.19
Pallidium	0.76 ± 0.06	0.22 ± 0.05	0.98 ± 0.19	1.03 ± 0.16	0.91 ± 0.25
PLIC	0.72 ± 0.05	0.61 ± 0.05	1.17 ± 0.13	0.92 ± 0.12	1.66 ± 0.34
Pons	0.76 ± 0.08	0.38 ± 0.04	1.22 ± 0.13	1.08 ± 0.12	1.53 ± 0.23
Putamen	0.72 ± 0.04	0.15 ± 0.02	0.96 ± 0.20	0.99 ± 0.18	0.93 ± 0.24
PWM	0.77 ± 0.07	0.40 ± 0.06	1.07 ± 0.07	0.95 ± 0.06	1.31 ± 0.19
Thalamus	0.80 ± 0.06	0.29 ± 0.02	1.04 ± 0.14	0.96 ± 0.11	1.16 ± 0.18
TWM	0.71 ± 0.05	0.63 ± 0.05	1.24 ± 0.11	0.94 ± 0.12	1.82 ± 0.28

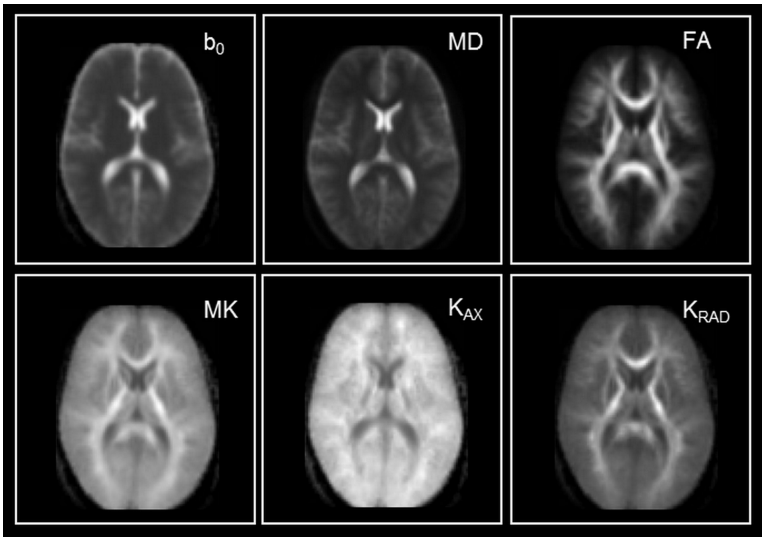

Figure 5.6.: EPI non-diffusion-weighted image (b_0), mean diffusivity (MD), fractional anisotropy (FA), mean kurtosis (MK), axial kurtosis (K_{AX}), radial kurtosis (K_{RAD}) maps shown for one axial slice for all 80 subjects of the merged group after normalisation.

was 0.80 $\pm$ 0.05; 1.68 $\pm$ 0.26; 0.99 $\pm$ 0.16; 1.02 $\pm$ 0.20; 0.84 $\pm$ 0.23 and 1.13 $\pm$ 0.19, the mean $\text{MK}_{\text{FirstObs/SecondMeas}}$ 0.80 $\pm$ 0.07; 1.85 $\pm$ 0.33; 0.99 $\pm$ 0.16; 1.03 $\pm$ 0.20; 0.78 $\pm$ 0.18 and 1.27 $\pm$ 0.22 and the mean $\text{MK}_{\text{SecondObs/FirstMeas}}$ was 0.81 $\pm$ 0.10; 1.69 $\pm$ 0.26; 1.00 $\pm$ 0.16; 1.02 $\pm$ 0.20; 0.83 $\pm$ 0.22 and 1.13 $\pm$ 0.18. The first and second MK measurements of the first observer ($p = 0.97$) and the measurements of the second observer ($p = 0.89$) were not significantly different (see table 5.2).

The results of the Bland-Altman analysis of the repeated measurements are shown in figure 5.8. This analysis showed a good agreement between the 1^{st} and 2^{nd} measurements of the 1^{st} observer with -0.02 and 0.00 as mean differences as well as between the 1^{st} measurement of the 1^{st} observer and the measurement of the 2^{nd} observer with mean differences of -0.02 and 0.01 for FA and MK.

Table 5.2.: The p-values derived from a two-sided, paired-samples Student's t-test. There was no significant difference between the first and second FA, MK measurements of the first observer and the measurements of the second observer.

P-Values	*MD*	*FA*	*MK*	K_{AX}	K_{RAD}
Intra-subject	0.32	0.74	0.97	0.32	0.33
Inter-observer	0.32	0.71	0.89	0.32	0.32

5.3.3.1. Age- and gender- dependency

Scatterplots for the correlations between age, MD, FA, MK, K_{AX}, and K_{RAD} are presented for some brain regions in figure 5.9, figure 5.10, figure 5.11, figure 5.12 and figure 5.13.

These analyses showed statistically significant reduction in MK and K_{RAD} ($p < 0.05$) with increasing age in the centrum semiovale, CCg, external capsule, FWM and the thalamus. In the

5. Construction of a whole brain atlas on the basis of magnetic resonance diffusion tensor and diffusion kurtosis data: Age and gender related study

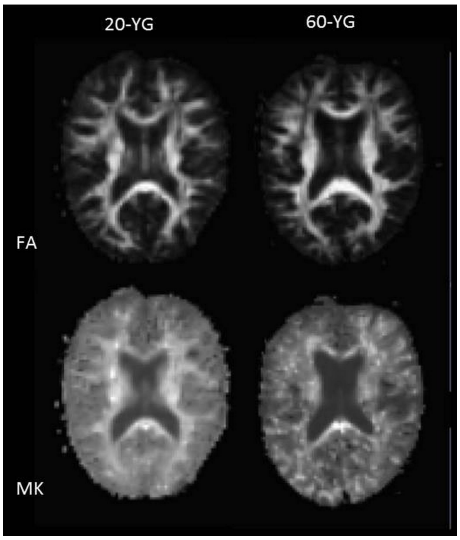

Figure 5.7.: Example of the FA and MK metrics in an axial image of a young adult of the 20-year group (left panel) and an older adult of the 60-year group (right panel). The FA map shows the restrictive micro-environment of water molecules, partly due to the high myelination, and is therefore higher in regions of more densely packed fiber bundles that are homogeneous oriented as for example in the corpus callosum. The demyelination is more pronounced on MK maps.

Pons, MK and K_{RAD} increased with age. For K_{RAD}, age dependence was additionally found with $p < 0.05$ in the CCs, ALIC and PLIC. In some areas, MD, K_{AX}, and FA declined with age (see figure 5.9, figure 5.10, figure 5.11, figure 5.12 and figure 5.13). Much the same results were obtained through ANOVA analyses among groups as described below.

ANOVA among the 20-, 30-, 40-, 50-, and 60-, year groups demonstrated significant differences for MK in the CCg $F(4, 40) = 4.38$, $p < 0.01$; the FWM $F(4, 40) = 3.24$, $p = 0.021$. For K_{RAD}, the groups showed statistical significant differences in the CCg $F(4, 40) = 2.84$, $p = 0.036$; the CCs $F(4, 40) = 3.65$, $p < 0.05$; the FWM $F(4, 40) = 2.28$, $p = 0.05$. Post-hoc testing using Student-Newman-Keuls showed that the 60-YG had significantly lower MK and K_{RAD} ($p < 0.05$) in regard to the other groups.

ANOVA tests revealed no statistically significant difference between different age groups for ALIC and PLIC on K_{RAD} maps (respectively, $p = 0.29$ and $p = 0.28$).

The linear regression analyses with female = 1 and male = 2 were used to test gender effects. FA and MK of the thalamus was statistically significant lower in females as compared to males ($p = 0.01$ and $p = 0.02$, respectively). No other statistically significant gender differences were found in the other parametric maps in the ROIs.

5.4. Discussion

DKI is more sensitive to brain microstructure than the well-known Diffusion Tensor Imaging (DTI) (see chapter 3); in particular in tumour micro-environments where DKI can provide valuable information and increase diagnostic confidence of brain tumours [52, 9]. A DKI human brain atlas artefacts-free and preserves sufficient adequate information on the micro-structural properties throughout the whole brain is therefore crucial for accurate voxel- and ROI-based comparisons across populations. In this work, many weaknesses of earlier published efforts to report

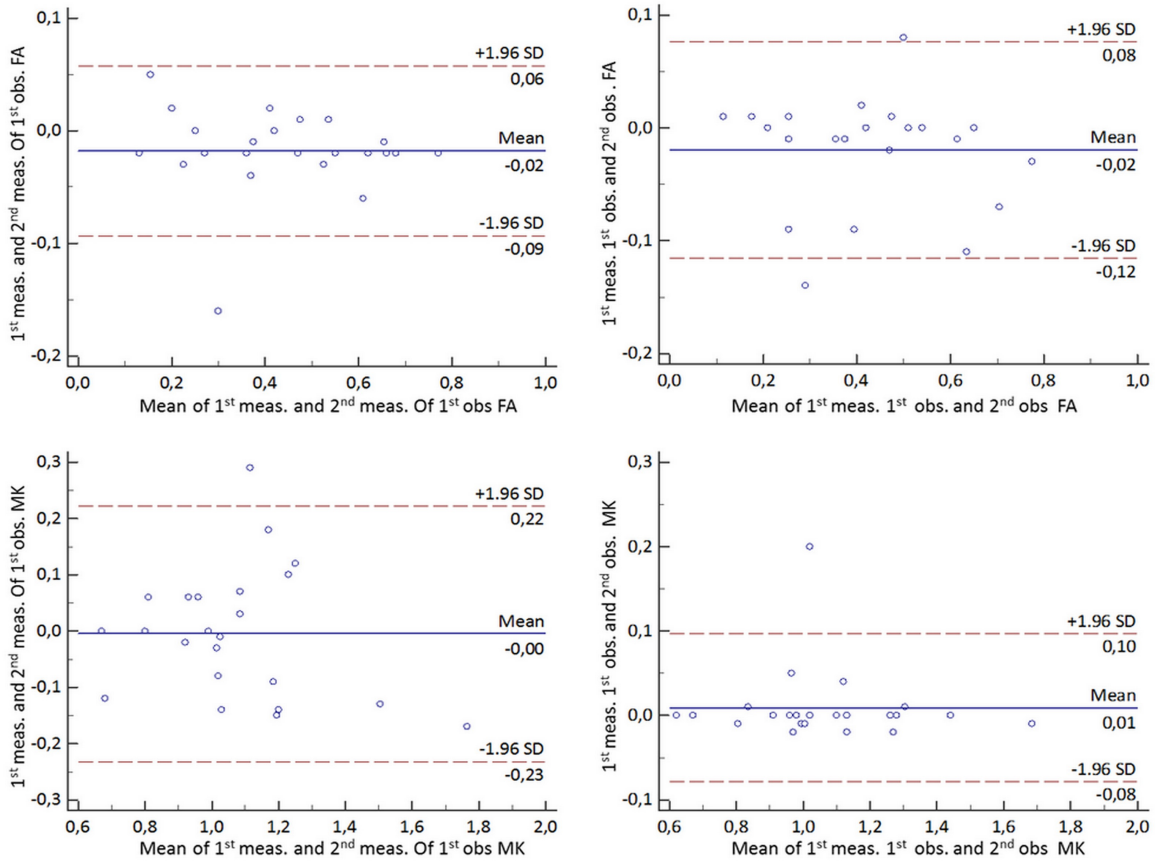

Figure 5.8.: Bland-Altman analysis of the difference between the repeated measurements of the two observers for fractional anisotropy (FA) and mean kurtosis (MK).

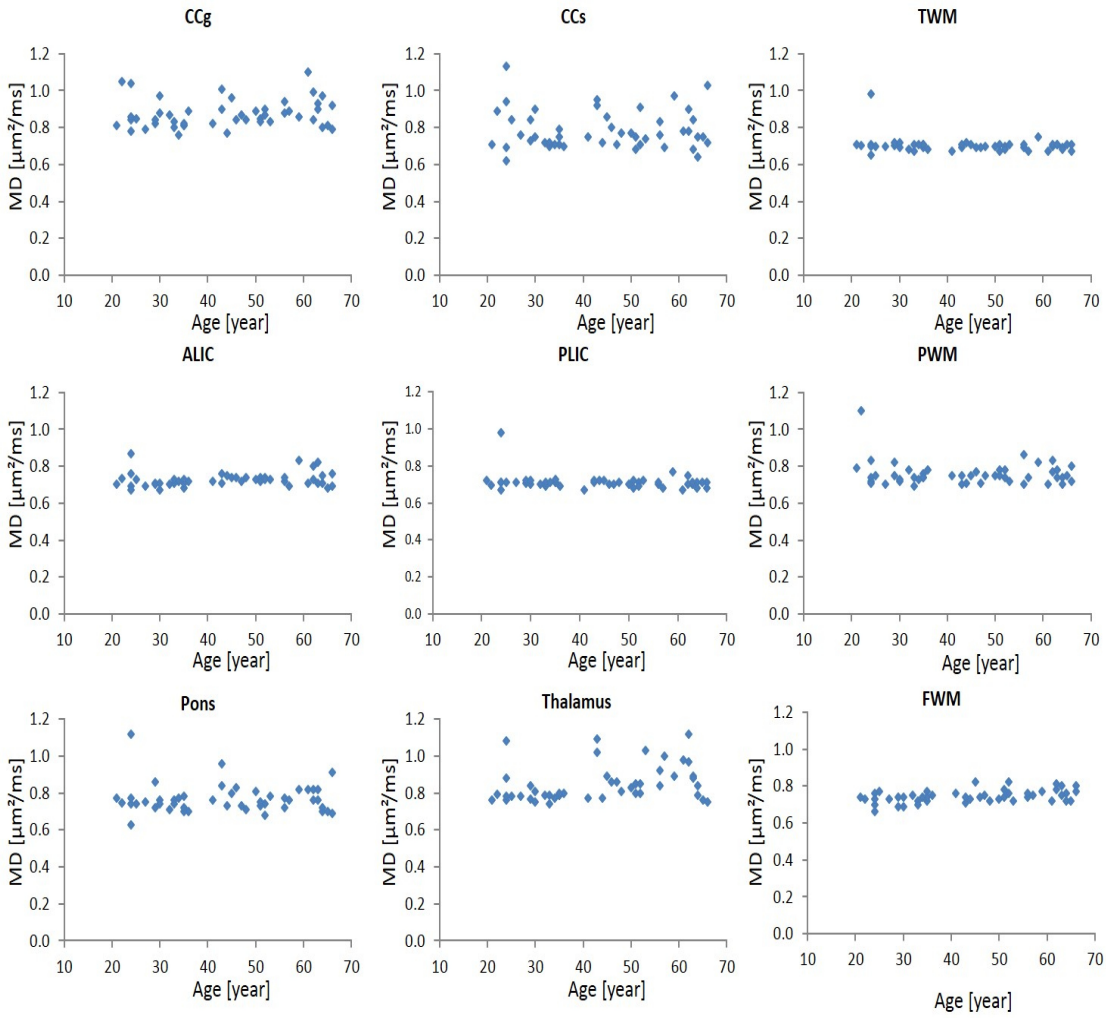

Figure 5.9.: Effect of aging on regional MD.

diffusion kurtosis values in the brain were addressed. Here the resulting set of DKI provides full brain coverage and contains reliable kurtosis metrics using 30 diffusion encoding directions (overestimated equation system) with 3 b-values (0, 1000 and 2000 s/mm^2). Furthermore, to date, this is the first DKI atlas based on a rather large number of subjects. In addition, the resulting DKI atlas matches the commonly used ICBM-152 anatomical well-known brain template of the MNI space, at the same time simplifying the combination of DKI, anatomical and functional brain investigations.

Previous studies have reported DKI values for selected human cerebral areas. For example, Falangola et al. [10] analysed non-Gaussian diffusion values of brain tissue microstructure in the prefrontal brain using 6 b-values and 30 diffusion encoding directions. In a study of Lätt et al. [118] regional values of DKI were reported for a 5.4-cm-thick slab of 27 slices over the brain from beneath the cerebral peduncles to the hand area of the primary motor cortex and more considering 15 directions with b-values 0, 500, 1000, 2500, and 2750 s/mm^2. In these previous studies, the FA and MK of the normal human brain have been reported to have a values that

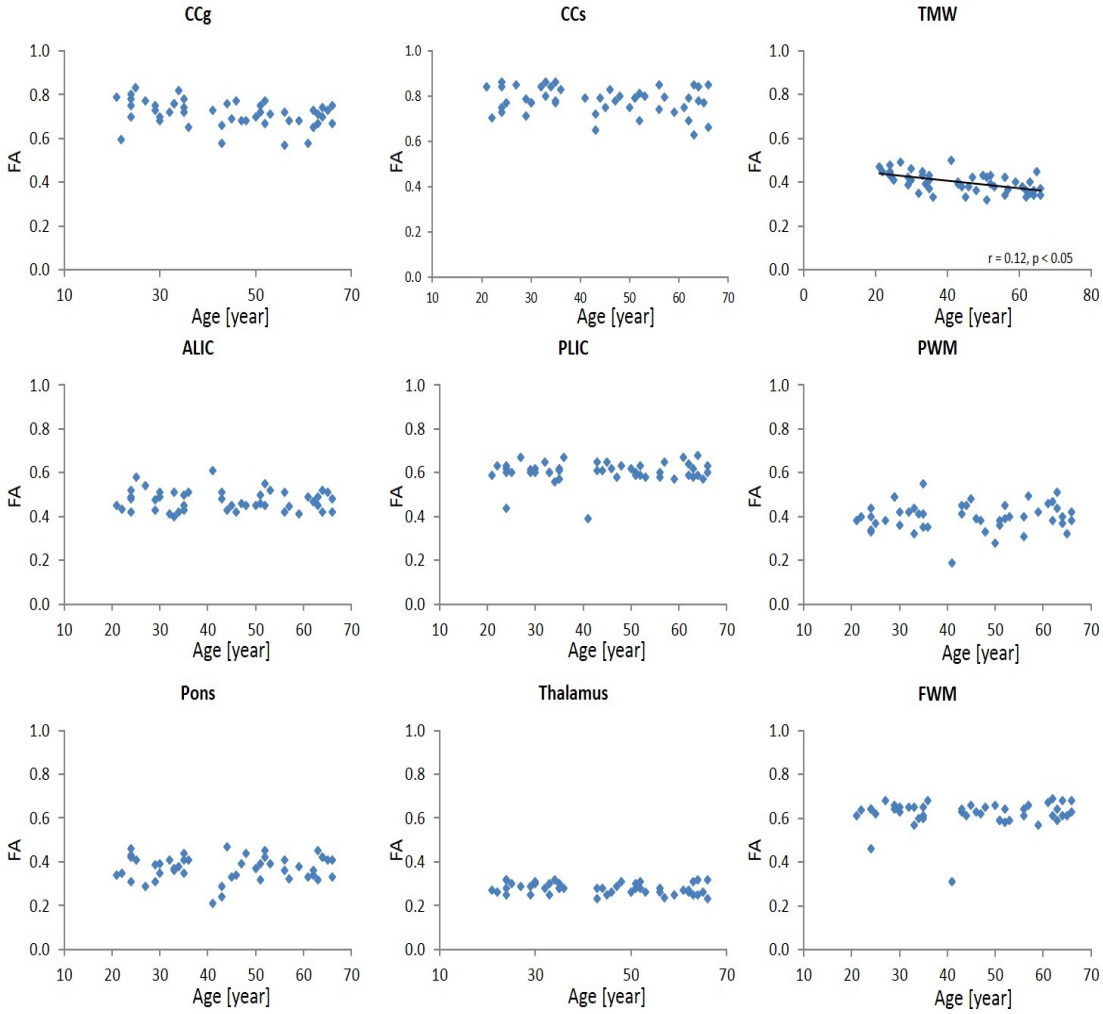

Figure 5.10.: Effect of aging on regional FA.

range between 0 and 0.80 and between 0.31 and 1.50 (dimensionless) respectively by Falangola et al. [10]. In the work of Lätt et al. [118] these values were between 0.14 in the caudate and 0.83 in the splenium of corpus callosum (CCs) for FA and 0.67 in the putamen and 1.32 in the CCs for MK.

The present work referred to the experiments of Poot et al. [125] where the DKI acquisition parameters are optimised for brain acquisitions. Their proposed setting with 30 diffusion gradient directions and b-values of 0, 1000 and 2000 s/mm^2 is considered here. This range of b-values for DKI in the brain was also already confirmed in a recent study of Jensen and Helpern, 2010 [9]. The average FA values of the principal atlas between 0.13 in the caudate and 0.80 in the CCs were comparable to the results of Lätt et al. [118]. While the MK values reported here ranging from 0.71 in the fornix to 1.76 were slightly higher compared to those reported by Falangola et al. [10], the differences were negligible referring to the work of Lätt et al. [118] (see table 5.3). The differences regarding the reports of Falangola et al. [10] might be explained by the fact that the data considering full brain coverage underwent pre-processing steps including motion- and

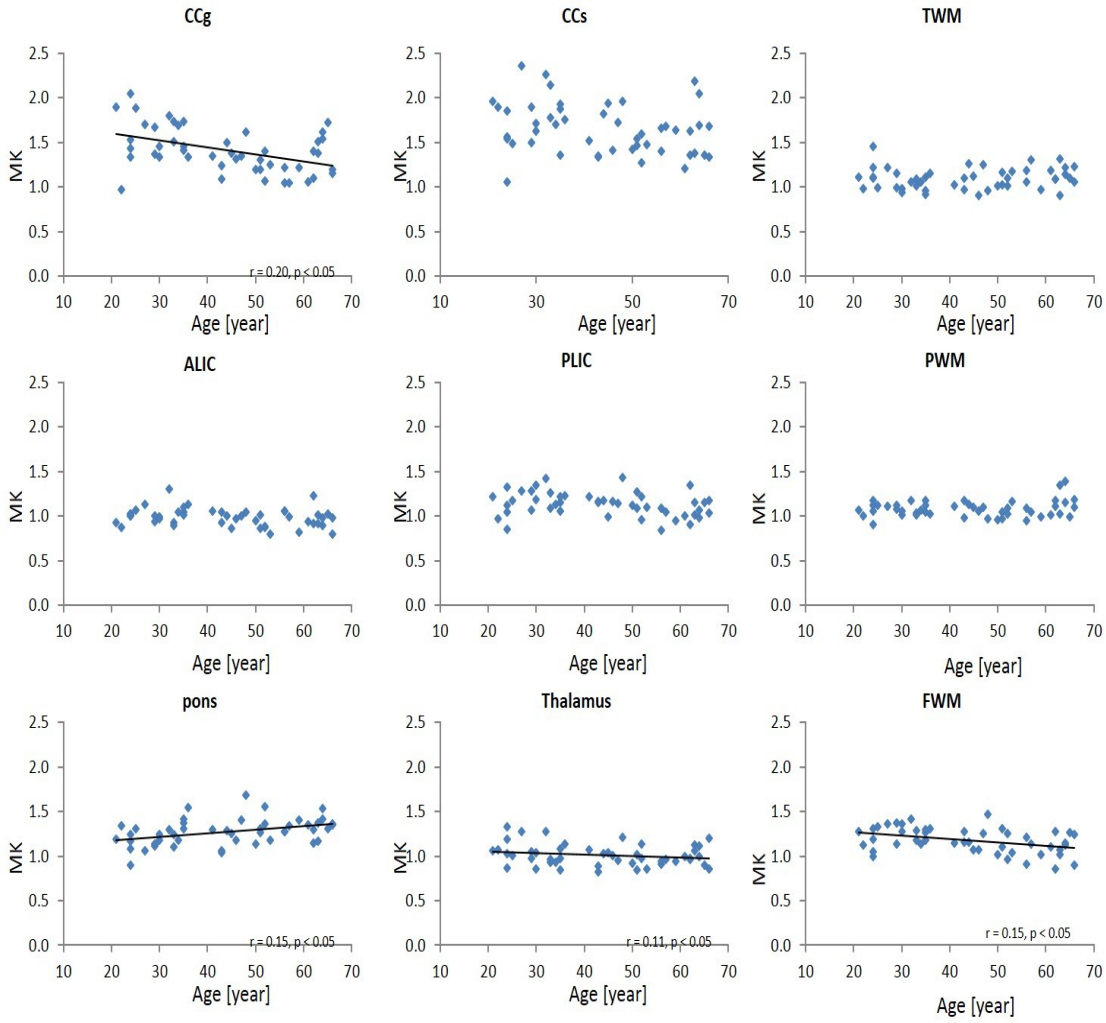

Figure 5.11.: Effect of aging on regional MK.

noise correction to ensure artefacts elimination in the whole brain prior to DKI computation. Additionally compared to the present study, Lätt et al. [118] reported DKI measures with 15 diffusion directions. Whereas another study [63], highlighted the fact that a higher number of directions has greater effects on acquiring suitable DW images justifying here the choice to report DKI measures using 30 diffusion directions.

5.4.1. Effects of participants' age and gender on the final human brain DKI atlas

In addition to the pre-processing procedures used for artefacts correction in this study, the human subjects considered were carefully recruited. This selection was based upon the report of Sullivan and Pfefferbaum [126] showing that age influences diffusion properties of brain tissues. Healthy subjects aged from 20 to 40 years were included in the principal DKI atlas, because it is well-known that the diffusion properties are relatively stable in the brain of this specific age group [122]. In a study of Mori et al. [123] or even a recent study of Lätt et al. [118], the authors averaged data from

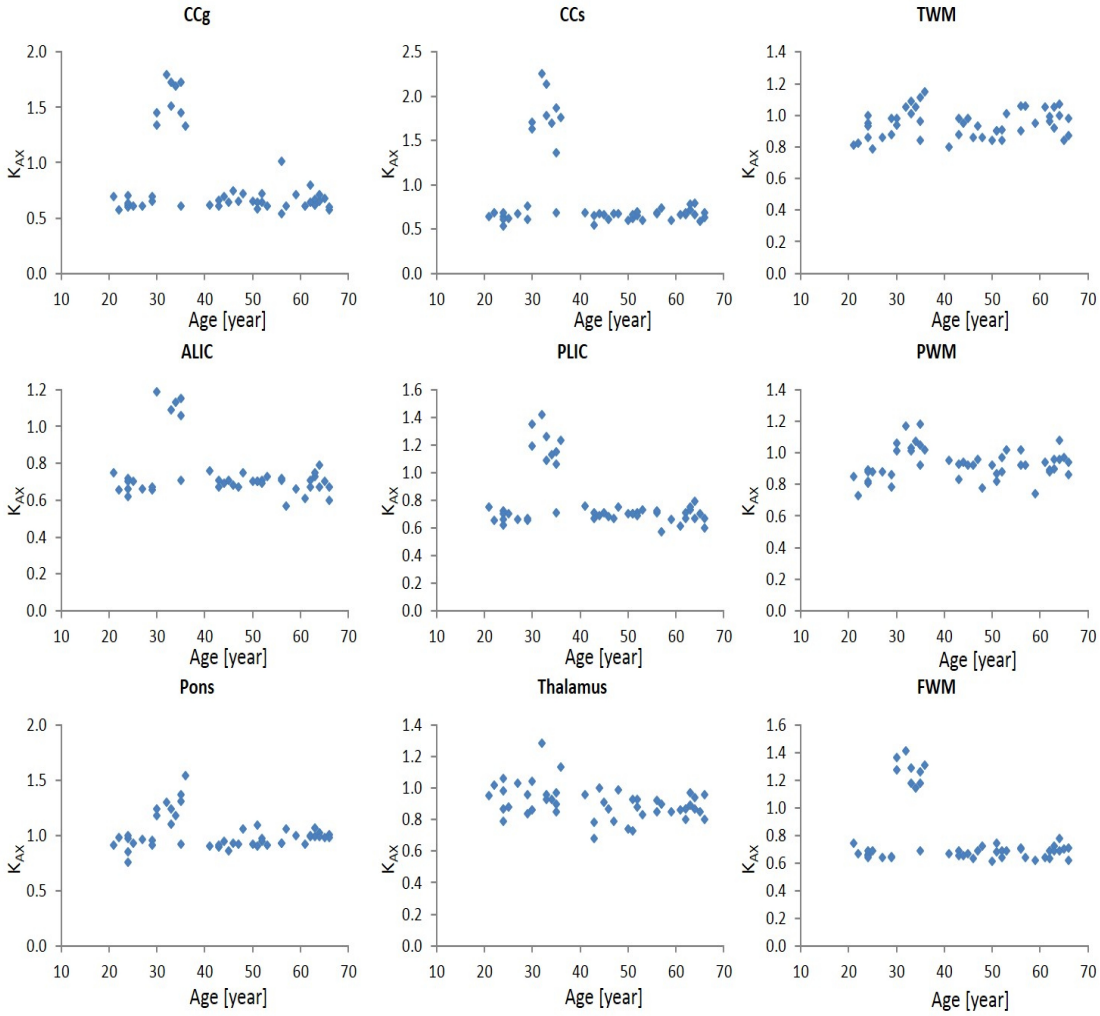

Figure 5.12.: Effect of aging on regional K_{AX}.

subjects with very different ages (18 – 59 years and 20 – 64 years, respectively); assuming that the dissimilarities in macro- and micro-structural properties of the brain is not significantly different among these age groups. This might explain the slightly different MK values detected in the work of Lätt et al. [118] compared to the proposed DKI atlas. As a result of the recruitment strategy, the principal DKI atlas introduced here reporting diffusion measures in the healthy human brain at the age of 20 to 40 years together with atlases over different age groups (20YG, 30YG, 40YG, 50YG, 60YG) in the whole brain, is meaningful and more useful.

5.4.2. Effects of spatial normalisation on the final human brain DKI atlas

Another major factor that contributes to the high quality of the DKI atlases introduced in this work is the spatial normalisation to the ICBM-152 template of the MNI space, as nonlinear registration in ANTs applied in the work. The benefits of non-linear approaches toward accurate normalisation of diffusion data are widely accepted [127, 128]. However, in some previously published studies

5. Construction of a whole brain atlas on the basis of magnetic resonance diffusion tensor and diffusion kurtosis data: Age and gender related study

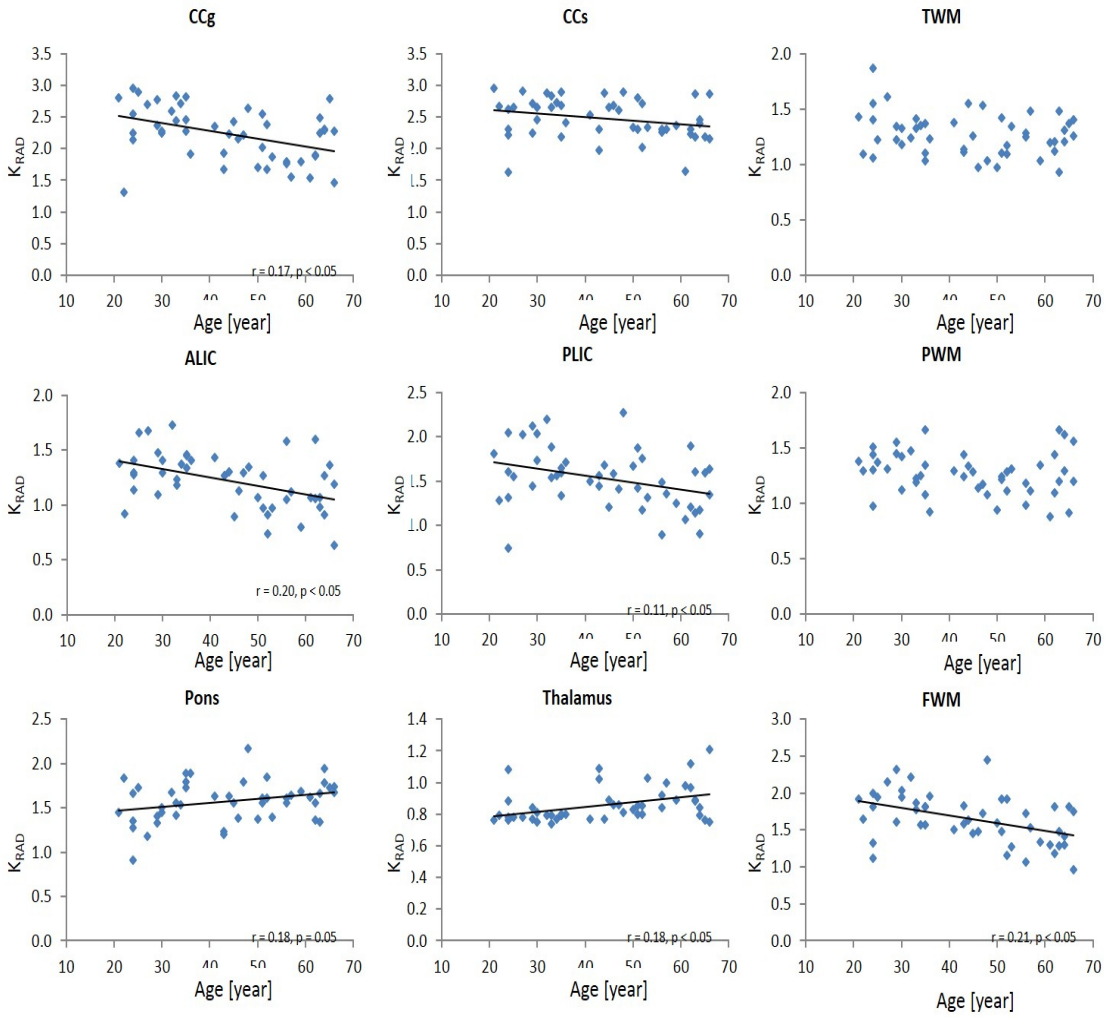

Figure 5.13.: Effect of aging on regional K_{RAD}.

on developing templates for DTI, affine registration driven by feature registration was used. As already pointed out by Jones [129] and Müller et al. [130] this might result in less accurate inter-subject matching. The major advantage of affine registration lies in its reduced sensitivity to noise in the image in regard to nonlinear techniques. In this work, the effects of image noise on nonlinear normalisation were minimised by fitting the DWI data prior to DKI computation. As a result, the mismatch of selected landmarks was only 0.71 mm on average. The normalisation step with diffeomorphic transformations and mutual information similarity measure used here also contributed to the increase the resolution of the diffusion kurtosis maps derived from the principal atlas. Recent advances in investigating atlas building methods published by Zhang et al. [131] introduced the DTI-TK as a FA-based non-parametric image normalisation software. The preference of FA as scalar feature compared to MD, DWI maps as well as b_0 images for normalisation in DTI was already highlighted by Liu et al. [132] using a fluid-based nonlinear registration. ANTs is using diffeomorphic deformable image registration just as DTI-TK. In this study a b_0-based registration is chosen since it still remains unclear whether FA-based

Table 5.3.: Mean and standard deviation (SD) of FA in ROIs of the principal atlas and template as well as regional values published by [118, 123, 122].

ROI	Principal atlas FA	Lätt et al. 2013-FA	Peng et al. 2009-FA	Mori et al. 2008-FA
ALIC	0.47 ± 0.05	0.60 ± 0.04	0.57 ± 0.04	0.44 ± 0.06
Caudate	0.13 ± 0.04	0.14 ± 0.03	--	--
CCg	0.74 ± 0.06	0.80 ± 0.04	1.40 ± 0.20	0.91 ± 0.07
CCs	0.80 ± 0.05	0.83 ± 0.03	--	--
Cingulate	0.37 ± 0.06	0.66 ± 0.06	0.84 ± 0.12	0.44 ± 0.08
Ext. caps.	0.54 ± 0.06	0.41 ± 0.03	--	--
FWM	0.42 ± 0.04	0.48 ± 0.04	--	--
PLIC	0.61 ± 0.05	0.71 ± 0.04	--	--
Putamen	0.15 ± 0.02	0.15 ± 0.02	--	--
PWM	0.40 ± 0.06	0.56 ± 0.05	--	--
TWM	0.63 ± 0.05	0.52 ± 0.03	--	--

diffeomorphic nonlinear registration could perform better or not. Therefore comparing the effect of using alternative atlas building methods on normalisation results under consideration of diffeomorphic nonlinear registration is an important area of future research.

In the present study the focus was on healthy subjects between the ages of 20 and 70 years. It is known that diffusion measures in the brain change with aging [122]. Therefore, the effect of age on diffusion kurtosis measures in the whole brain of subjects younger than 20 and older than 70 still has to be investigated. Additionally, no handedness criterion was considered in the recruitment strategy. In a recent study, Powell et al. [133] noticed differences in anisotropy measurements comparing left-handed to right-handed. Therefore, further studies should investigate the effect of left-, right- and mixed-handedness on the diffusion measurements achieved with kurtosis imaging.

Furthermore, a single-shot EPI sequence was used for DKI data acquisition. In addition to their low spatial resolution, EPI images are very sensitive to geometric distortions and susceptibility errors [134]. An approach that might further help to increase the resolution of DW acquisitions and to reduce the susceptibility and blurring artefacts would be the use of readout-segmented muti-shot EPI sequences. This method can significantly increase the image quality compared with DW sequences with single-shot EPI at 3T [135].

The analysis of normalisation accuracy performed in this study refer to normal adult subjects not including patients with significantly altered neuro-anatomy. Compromised neuro-anatomy in patients, such as enlarged ventricles, can impact results of a poor registration process [123]. Therefore, a careful inspection of the normalisation process on patient data should be guaranteed for an adequate interpretation of the diagnostic findings.

In conclusion, a set of human whole brain DTI and DKI atlases were developed for subjects between 20 and 40 years of age and for subjects in five age groups (20 – 29; 30 – 39; 40 – 49; 50 – 59; and 60 – 69). The DKI atlases match spatially the ICBM-152 template and are characterised by controlled image quality, full brain coverage, and reliable kurtosis metrics based on a large number of subjects. With advancing age, significant diffusion related changes were noticed in some regions of the brain for the FA, MK and K_{RAD} maps. These changes were more pronounced

in kurtosis measures compared to fractional anisotropy indices. Additionally, ROI measurements in the thalamus showed a gender-depended decrease in MK values of females compared to males.

Chapter 6

Cortico-medullary differentiation in human kidneys with DKI

Important anatomic structures of the kidneys such as tubules that are orientated in a radial fashion resulting in anisotropic diffusion (see chapter 3), could already be assessed with DTI [136]. However, since conventional DTI has limitations in assessing the non-Gaussian behaviour of water molecules diffusion [9] (see section 3.4 for more details), DKI might be more helpful than DTI for assessing renal diseases affecting the renal microstructure, particularly function and structure of tubular integrity such as renal tumours and renal artery stenosis.

In this chapter, the feasibility and reproducibility of DKI of the human kidney are investigated. Here the cortico-medullary differentiation in kurtosis maps was examined in details.

6.1. Data acquisition

The review board agreed to the protocols and all volunteers signed the informed consent before the start of the study. Ten young healthy volunteers (6 men, 4 women, mean age 28.50 $\pm$ 3.34 years, range 28 - 34 years) without any history of renal disease, previous renal surgery, or any known systemic disease potentially related to the kidneys were included in this study.

A 3T whole-body clinical MRI scanner (Magnetom Trio, a TIM system; Siemens Medical Systems, Erlangen, Germany) was used for the examinations with a 6 channel body coil and a 24 channel spine coil integrated into the scanner table.

For DKI, a single-shot EPI sequence was applied in the coronal plane using respiratory triggering via a respiratory belt with 3 b-values (0, 300 s/mm^2 and 600 s/mm^2), 30 diffusion directions and 8 signal averages. Other imaging parameters were: echo time (TE) $=$ 90 ms, repetition time (TR) $=$ 1500 ms, matrix $=$ 192 $\times$ 192, field of view (FOV) $=$ 400 mm, 10 slices with a slice thickness of 5 mm. GRAPPA (generalised auto-calibrating partially parallel acquisition) accelerated with a factor of 2 was applied as parallel imaging method. The mean acquisition time of the respiratory triggered DKI sequence was 32:08 $\pm$ 4:37 min (range, 23:56 - 36:30 min).

6.2. Data analysis

Initially, all diffusion-weighted (DW) images were reviewed including a subjective motion analysis by a radiologist with more than 10 years' experience in image processing and MR diffusion imaging to assess whether the MR image quality was good enough for subsequent analysis. For this purpose, a landmark was set on the first $b = 0$ s/mm^2 non DW image of the kidney of each volunteer that served as reference and then in the following $b = 300$, 600 s/mm^2 DW images. The displacement between the reference landmark and the landmarks in the DW images were measured to quantify motion. The results were averaged over all the subjects to obtain minimal and maximal values of the diffusion maps.

The DKI tensor was estimated as described in chapter 4 using the MATLAB scripts. The estimated tensors were utilised to determine the diffusion kurtosis measures for each subject corresponding to the parameters apparent diffusion coefficient (ADC), fractional anisotropy (FA), mean kurtosis (MK) according to the methods of Tabesh et al. [51] and Le Bihan et al. [7] respectively as explained in section 3.4. Although values of radial kurtosis (K_{RAD}) and axial kurtosis (K_{AX}) could be determined from the acquired data, apart from figure 6.2 where they are shown once, they are not reported in the present work, but focus is either laid on investigating the relevance of MK measures for human kidney DKI.

To optimise the DKI sequence by the means of acquisition time versus SNR, parametric images of ADC, FA and MK were calculated from subsets of the measured DWI including 2, 4, 6 and 8 signal averages. ROIs were drawn by hand on the averaged $b = 0$ s/mm^2 images for different signal averages. The $b = 0$ s/mm^2 image was chosen for the measurements because of the lower SNR in the DW images [137]. SNR was given by the ratio of the mean signal intensity S within the ROI to the standard deviation (SD) of the background noise in an homogeneous region $SNR = S/SD$.

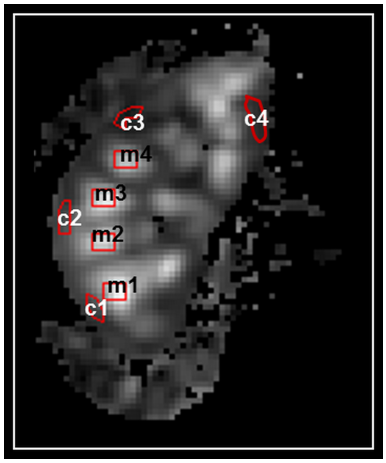

Figure 6.1.: Free hand ROIs on the cortex and medulla of the upper pole, mid-zone and lower pole shown on the FA image.

Eight separate, manually drawn ROIs of 9 to 13 pixels were placed on the FA map of each subject because of its proven high cortico-medullary discrimination [136]. The ROIs were drawn over the cortex and medulla on the upper pole, mid-zone and lower pole of the right kidney in each subject (figure 6.1). For analysis, the right kidney was selected because it is less prone to cardiac and respiratory motion artefacts since the liver is placed above it [138]. ROIs on FA maps were copied onto the corresponding position on the ADC and MK maps. The mean and SD of the FA and MK

values respectively as averaged values of the 4 ROIs on the cortex and the 4 ROIs on the medulla were calculated for all the signal averages to quantify the cortico-medullary differentiation.

As an indicator of measurement error or reproducibility, the intra-subject reproducibility and inter-observer variability of FA and MK values were examined using the free hand ROI technique [57]. Intra-subject reproducibility analysis was based on data of one volunteer imaged on different dates. The interval between the MRI measurements was 14 days. The FA and MK values of the 1st measurement were assessed and compared to the values obtained from the 2nd measurement. For the inter-observer variability, two radiologists were instructed to independently place the ROIs on the cortex and medulla of the same volunteer using data of the 1st MRI measurements of the two observers. A two-sided, paired-samples Student's t-test was used to compare the results from the 1st and 2nd measurements of the 1st observer and the results from the 1st measurements of the two observers.

For qualitative evaluation, a 5-grade human observer study of MK and FA maps was conducted by the two radiologists taking into account the cortico-medullary discrimination. Data of 6 subjects from all the signal averages (2, 4, 6, and 8) were included in this analysis. For graduation the following point-scale was used: 1 for not evaluable; 2 for poor (no visible cortex-medulla difference); 3 for moderate (visible cortex-medulla difference but not clear); 4 for good (plausible cortex-medulla difference); 5 for excellent (clear cortex-medulla difference).

Statistical tests were performed using the curve fitting and statistics toolbox in MATLAB (Version: 8.0.0.783 (R2012b)). For all the tests, a p-value < 0.05 indicates a statistically significant difference.

To assess cortico-medullary differentiation for various signal averaging (2, 4, 6 and 8 averages), a Student's t-test statistic was used.

A goodness of fit evaluation was performed to test for the mathematical fitting of the mono-exponential and kurtosis models to the DWI data (see equation 3.23 and equation 3.7). The R^2 value was calculated, which is the square of the correlation between observed and expected outcome values. R^2 is expressed as [139]:

$$R^2 = 1 - \frac{\text{SSR}}{\text{SST}} \tag{6.1}$$

where SSR stands for the sum of squares of the distance between the data points and the best-fit curve. SST is the sum of squares of the distances between the data points and the mean value of all data points [140]. For the fitting, mean signal intensities of the ROIs placed over the cortex (see figure 6.1) of DWI images over all the volunteers for the 8 averages were computed. These averaged values were then placed on a graph as function of the 3 b-values (0, 300 s/mm^2 and 600 s/mm^2). Repeated-measures analysis of variance (ANOVA) with the Tuckey's honestly significant difference (HSD) post-hoc test was used to examine the effect of variable signal averaging on the cortico-medullary differences of MK.

Intra-subject reproducibility and inter-observer variability was calculated from reproducibility measurements using a two-sided, paired-samples Student's t-test and Bland-Altman plots. With the Bland-Altman plots one can analyse whether two different measurements are similar or not. The difference versus the mean of the DKI parameters of the repeated measurements is plotted. This was plotted for the two measurements of the 1st observer and the 1st measurement of the 1st observer and the 2nd observer.

Table 6.1.: Mean ± standard deviation (SD) of ADC, FA and MK values of the renal cortex and medulla for 2, 4, 6, 8 averages (av.) from data of 10 volunteers.

N° of signal	ADC $\times 10^{-3} mm^2/s$		FA		MK	
averages	Cortex	Medulla	Cortex	Medulla	Cortex	Medulla
2 av.	2.91 ± 0.22	2.66 ± 0.22	0.21 ± 0.05	0.38 ± 0.06	0.93 ± 0.09	0.86 ± 0.11
4 av.	3.60 ± 0.28	2.82 ± 0.25	0.18 ± 0.04	0.42 ± 0.05	0.94 ± 0.07	0.78 ± 0.07
6 av.	3.27 ± 0.24	3.61 ± 0.23	0.18 ± 0.03	0.46 ± 0.10	0.91 ± 0.03	0.74 ± 0.07
8 av.	3.39 ± 0.24	3.80 ± 0.28	0.19 ± 0.03	0.43 ± 0.07	0.91 ± 0.04	0.78 ± 0.06

6.3. Results

In all subjects a maximal motion of 0.28 ± 0.02 mm (range, 0.05 - 0.29) was measured from the landmark displacement. Representative images are shown on figure 6.2.

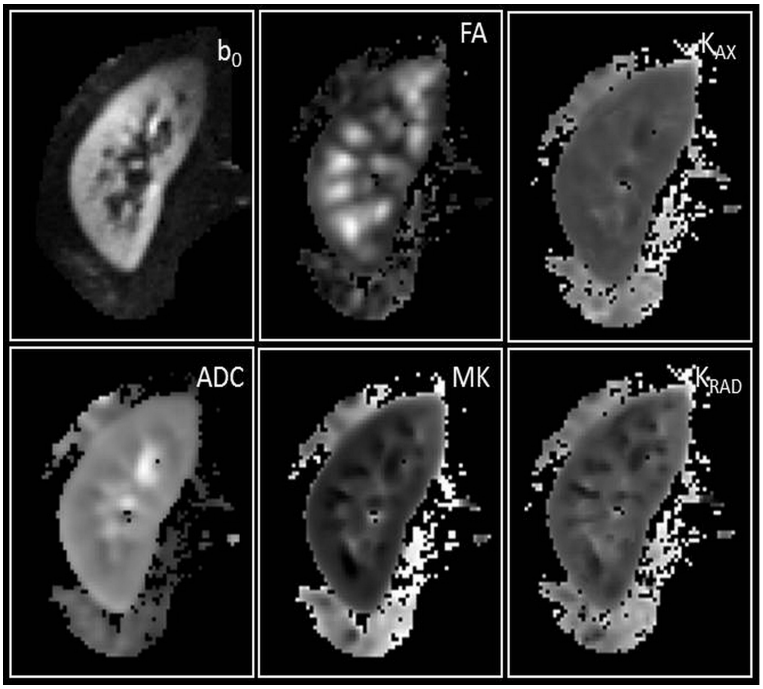

Figure 6.2.: EPI non diffusion-weighted image (b_0), apparent diffusion coefficient (ADC), fractional anisotropy (FA), mean kurtosis (MK), axial kurtosis (K_{AX}) and radial kurtosis (K_{RAD}) maps are shown for one coronal slice for one healthy volunteer.

Mean ADC, FA and MK values were obtained with the four different signal averaging sequences. ADC values ranged from 2.91 $\times$ 10^{-3} mm^2/s to 3.60 $\times$ 10^{-3} mm^2/s in the cortex and from 2.66 $\times$ 10^{-3} mm^2/s to 3.80 $\times$ 10^{-3} mm^2/s in the medulla. FA of the cortex ranged from 0.18 to 0.21, whereas that of the medulla ranged from 0.38 to 0.46. MK of the renal cortex ranged from 0.91 to 0.94 and that of the medulla ranged from 0.74 to 0.86 (table 6.1). MK values of the renal cortex were significantly higher than in the medulla while FA values in the medulla were significantly higher than in the cortex ($p < 0.001$). Mean values for FA and MK are listed on figures 6.3 and 6.4.

Respiratory triggered acquisitions with 4 averages (total acquisition time was 15:47 $\pm$ 2:42 min,

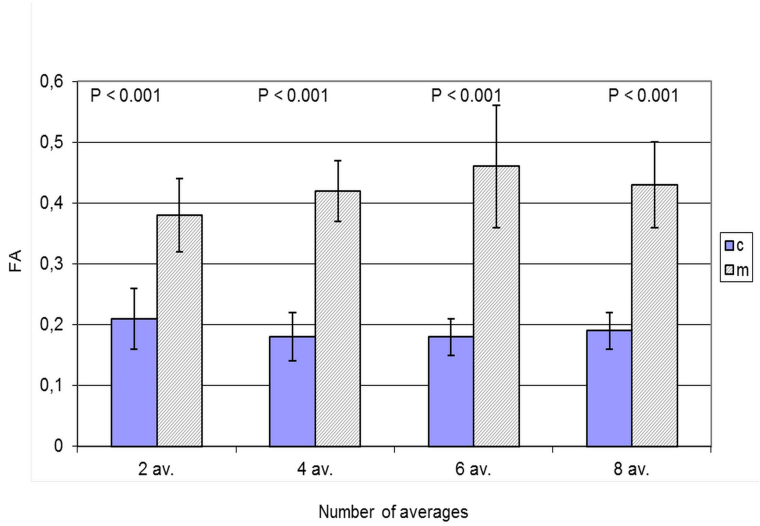

Figure 6.3.: Differences between the cortex (c) and medulla (m) on FA maps for the 2, 4, 6, 8 averages (av.). The y-axis reveals the different mean FA values between cortex and medulla over the 10 subjects.

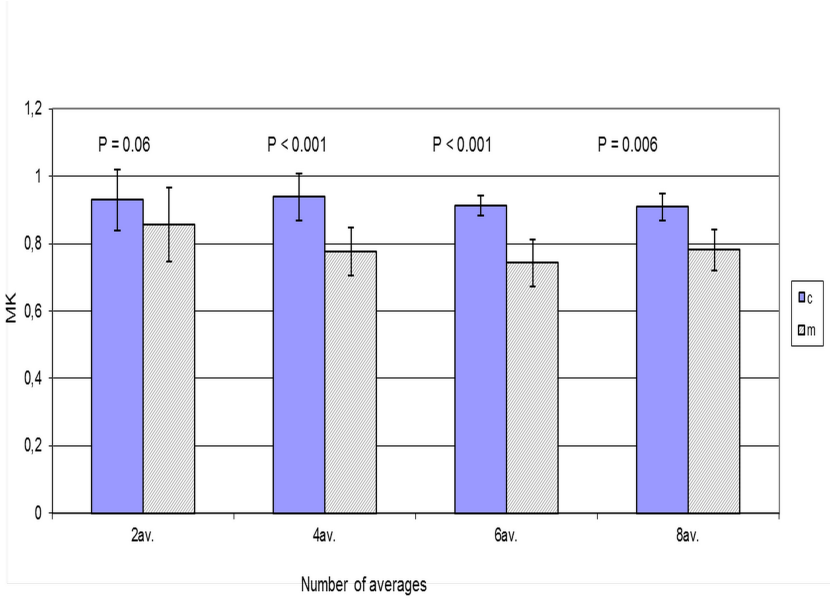

Figure 6.4.: Differences between the cortex (c) and medulla (m) on MK maps for the 2, 4, 6, 8 averages (av.). The y-axis reveals the different mean MK values between cortex and medulla over the 10 subjects.

Table 6.2.: Mean $\pm$ SD values of FA and MK for each measurement (meas.) in the cortex and the medulla for the two observers (obs.).

	Cortex		Medulla	
	FA	MK	FA	MK
1st obs.1st meas.	0.19 ± 0.03	0.88 ± 0.10	0.52 ± 0.04	0.74 ± 0.05
1st obs. 2nd meas.	0.20 ± 0.03	0.93 ± 0.05	0.48 ± 0.07	0.79 ± 0.09
2nd obs.	0.18 ± 0.02	0.85 ± 0.11	0.47 ± 0.07	0.71 ± 0.06
Mean	0.19 ± 0.03	0.88 ± 0.09	0.49 ± 0.06	0.75 ± 0.14

Table 6.3.: The p-values obtained from a two-sided, paired-samples Student's t-test. No significant difference was found comparing the 1st and 2nd FA, MK.

	Cortex		Medulla	
	FA	MK	FA	MK
Intra-observer	0.71	0.13	0.29	0.73
Inter-observer	0.73	0.07	0.24	0.47

Table 6.4.: Qualitative evaluation of FA and MK maps from data of 6 volunteers. *Evaluations were made with a scoring at 5-grades: 1 for not evaluable; 2 for poor cortex-medulla difference; 3 for moderate cortex-medulla difference; 4 for good cortex-medulla difference and 5 for excellent cortex-medulla difference. All the images used in the analysis had a score superior to 1.

	FA map						MK map					
Evaluation*	2	3	4	5	Mean	SD	2	3	4	5	Mean	SD
2 av.	1	4	1		3	0.63	3	3			2.5	0.55
4 av.		1	3	2	4.17	0.75		5	1		3.17	0.41
6 av.			4	2	4.33	0.52		4	1	1	3.5	0.84
8av.			2	4	4.67	0.52		4	1	1	3.5	0.84

range: 13:26 - 19:06 min) exhibiting a SNR of 8.31 ($p < 0.001$) resulted in improved image quality with better cortico-medullary differentiation in FA and MK maps compared to the sequence with 2 averages (SNR = 6.12). Whereas the use of 6 (SNR = 8.33) or 8 averages (SNR = 8.34) did not lead to a further improvement as compared to 4 averages. Representative images of one subject are shown on figure 6.5.

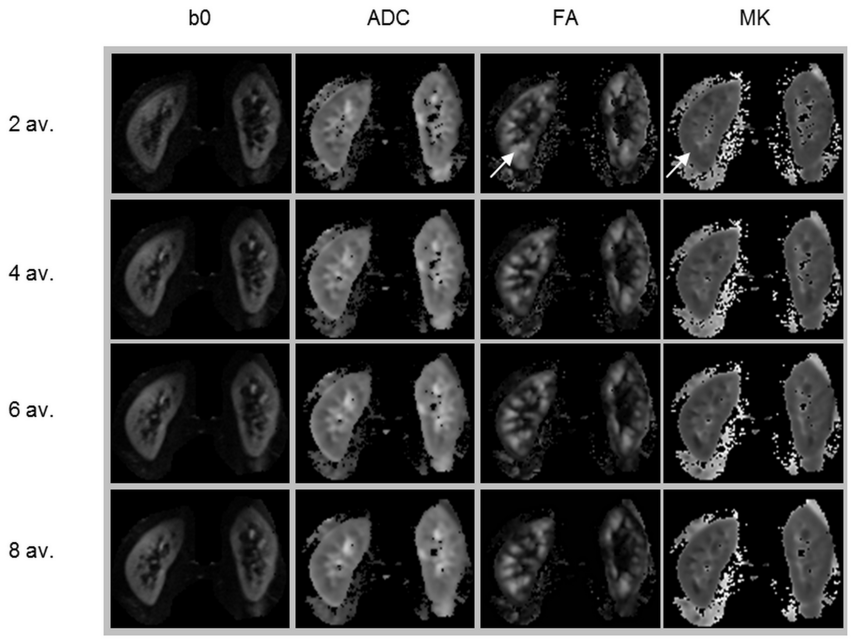

Figure 6.5.: $b = 0$ images without diffusion-weighting, ADC maps, FA maps and MK maps obtained with different sequences in the same volunteer with 2, 4, 6 and 8 averages (av.). The arrows point out better cortico-medullary differentiation in 2 averages compared to the sequences with 4, 6, and 8 averages.

Respectively for the cortex and the medulla, the mean $FA_{\text{first/first}}$ measured was 0.19 $\pm$ 0.03 and 0.52 $\pm$ 0.04, the mean $FA_{\text{first/second}}$ was 0.20 $\pm$ 0.03 and 0.48 $\pm$ 0.07, and the mean FA_{second} was 0.18 $\pm$ 0.02 and 0.47 $\pm$ 0.07. No significant difference was found comparing the 1st and 2nd FA measurements of the 1st observer ($p = 0.71$; $p = 0.29$) and the measurements of the 2nd observer ($p = 0.73$; $p = 0.24$). The globally measured mean $MK_{\text{first/first}}$ was 0.88 $\pm$ 0.10 and 0.74 $\pm$ 0.05, the mean $MK_{\text{first/second}}$ was 0.93 $\pm$ 0.05 and 0.79 $\pm$ 0.09, and the mean MK_{second} was 0.85 $\pm$ 0.11 and 0.71 $\pm$ 0.06. No significant difference was found between the 1st and 2nd FA measurements of the 1st observer ($p = 0.13$; $p = 0.73$) and the measurements of the 2nd observer ($p = 0.07$; $p = 0.47$). The FA and MK measurements with the matching p-values are indicated in Tables 6.2 and 6.3.

From the qualitative evaluation of the FA and MK maps with different number of averages (2, 4, 6, and 8), the sequence with 8 averages scored highest, followed by the sequences with 6 and 4 averages; the sequence with 2 averages had the lowest score (table 6.4).

Figure 6.6 illustrates how the mean signal intensity decreases in a homogeneous region in the kidney of one subject as a function of the b-value. The data points on the plot show that the decay is nonlinear. The fitting curves from the mono-exponential and the diffusional kurtosis model are also illustrated. Here, it is clear that the non-Gaussian kurtosis analysis fits the data point considerably better than does the mono-exponential fitting procedure. The R^2 value for the mono-exponential fit was 0.96 and 0.99 for the kurtosis fit. As seen on the figure, a b-value

of 600 s/mm^2 is already sufficient to observe the deviation of the renal MR diffusion signal from the mono-exponential behaviour.

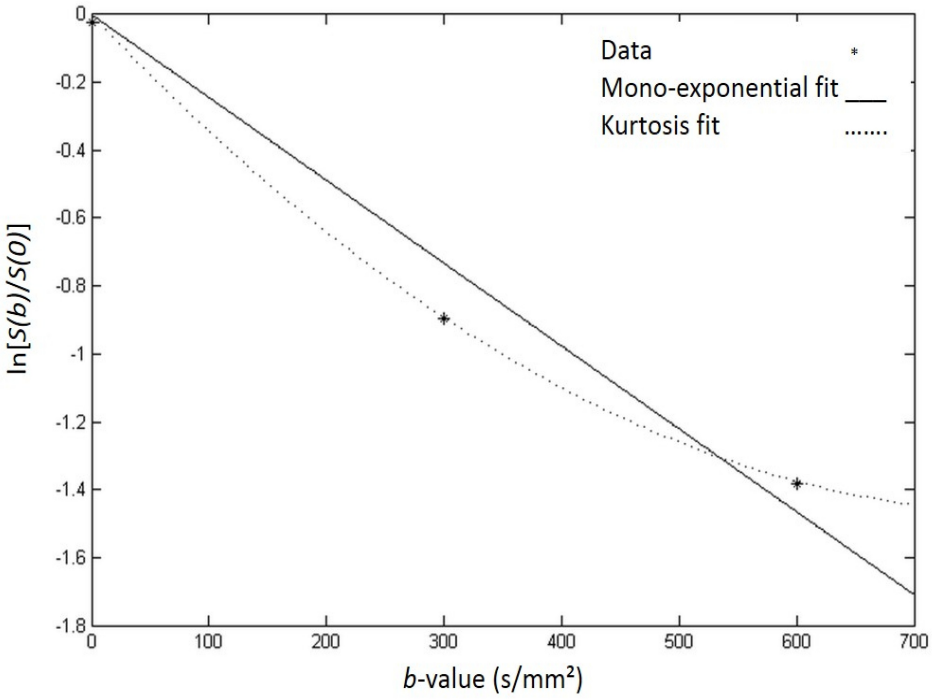

Figure 6.6.: Example of a diffusion MR signal attenuation of the renal cortex ($S/S(0)$) against the b-value, including the mathematical fitting of the two models [(3.23)] and [(3.7)] to illustrate data modelling. The asterisks (*) stands for the signal intensities measured within ROIs in the renal cortex (see figure 6.1) averaged over the 8 signal averages and all the volunteers; "mono-exp" and "kurt" denote the mono-exponential and the kurtosis model. The graph clearly illustrates the errors associated with the assumption of Gaussian distribution of water diffusion as in the case of the mono-exponential fit ($r = 0.96$) versus a non-Gaussian distribution assumption from DKI ($r = 0.99$).

Repeated-measures analysis of variance by one-way ANOVA in MK showed that there was a statistically significant difference considering the cortex-medulla discrimination between groups with different signal averages ($F(1,6) = 25.46$, $p = 0.0023$). To further analyse the differences, a post-hoc analysis was performed with Tukey HSD using the sequence with 4 averages as control. Compared to the sequence with 2 averages, the sequence with 4 averages showed significantly higher cortex-medulla difference ($p = 0.02$). There were no statistically significant differences between sequences with 4, 6 and 8 averages.

The results of the Bland-Altman analysis of the repeated measurements are shown on figure 6.7. This analysis showed that there is a good agreement between the 1st and 2nd measurements of the 1st observer with -0.02 as mean difference as well as between the 1st measurement of the 1st observer and the measurement of the 2nd observer with a mean difference of 0.03. No obvious deviation was observed in regard to absolute values. All the recordings were placed in the 95 % limits of agreement.

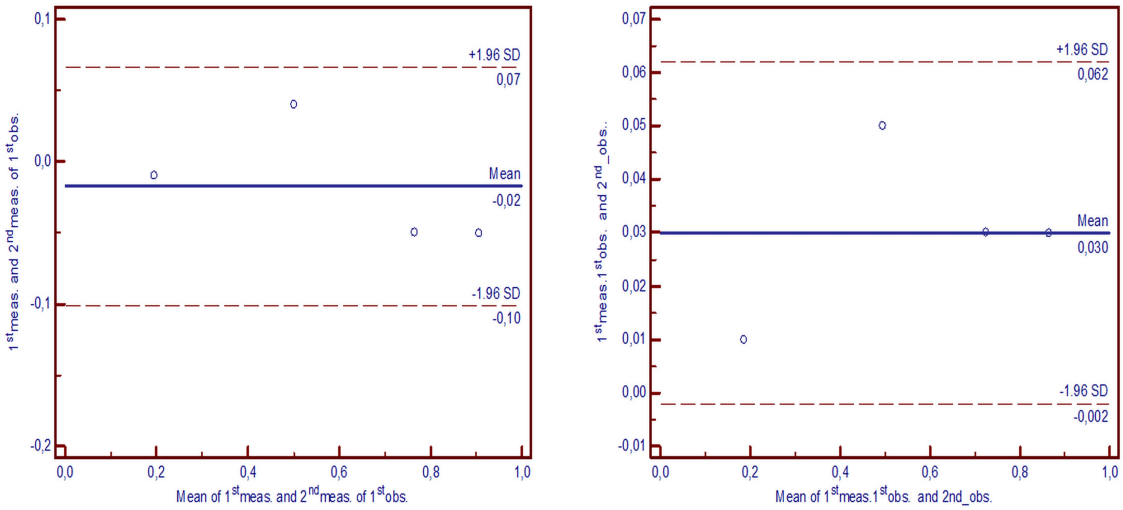

Figure 6.7.: Bland-Altman analysis of the difference between the repeated measurements of the two observers.

6.4. Discussion

In this study, respiratory triggered acquisitions are used to demonstrate that DKI of the kidneys is feasible with good cortico-medullary differentiation. DKI could be performed in all subjects with reliable image quality. Merging the results of the MK, FA and ADC-values, cortex-medulla contrast, reproducibility, and quantitative evaluation, the resulting DKI sequence exhibited a SNR of 8.31 when using $b = 0, 300, 600$ s/mm^2. This was reached with the respiration triggered DKI sequence designed here using 4 signal averages and 30 diffusion-weighting directions which resulted in a total measurement time of about 15 min.

Few scientific reports have studied the use of non-Gaussian DWI for abdominal organs. However, none of these studies measured the complete kurtosis tensor. Rosenkrantz applied non-Gaussian DWI for a better characterisation of diffusion processes in the prostate [141]. As an additional challenge, a crucial problem for calculation of parameters of higher diffusion models in abdominal organs [142] is the low SNR.

From previous studies, it is well known that ADC values in the healthy kidney lie between 3.00 and 1.50 $\times$ 10^{-3} mm^2/s [57]. Thoeny et al. [65] demonstrated that using low b-values for DWI leads to no significant difference between ADC in the cortex and ADC in the medulla in healthy subjects. They explained this observation by the influence of pure diffusion in the cortical regions being restricted by the presence of anisotropy in the radial structures of the medulla. Similar to these results, they reported that in the cortex ADC values are significantly different from those of the medulla when higher b-values are used. The average FA values in this actual study were comparable to values reported by Ries et al. [61] but slightly lower than in other volunteer studies [26]. These differences can be explained by the influence of blood flow on diffusion coefficients [143]. Notohamiprodjo et al. [136] applied DTI in human kidneys at 3T. In the healthy subjects, consistent with the results here, the medulla with higher FA values showed higher anisotropy compared to the cortex. They used two b-values (200 and 400 s/mm^2) with 12 diffusion encoding directions and the observation was with higher b-values and an increased number of directions, the measurement of diffusion is more accurate. Another study [63] reported that if similar acquisition time is maintained, a higher number of directions

has greater effects on acquiring suitable DW images than increasing the number of averages and is much more important to get reliable diffusion indices. In addition, the departure of the diffusion process from the Gaussian model is well-observed with the use of higher b-values (1000, 2000 s/mm^2) in brain DKI [6, 9, 51, 144, 145]. This study shows that b-values in the range of about 600 - 800 s/mm^2, are sufficient in abdominal DKI to observe the departure of the diffusion signal from mono-exponential behaviour. This was already demonstrated in the work of Wittsack et al. [140] when evaluating the DWI signal of the human kidney with b-values up to 750 s/mm^2. Again, Rosenkrantz applied the kurtosis model in the prostate at a maximal diffusion strength of 800 s/mm^2 [141]. Because of the low SNR at high b-values in abdominal DKI and the above mentioned reasons, the choice of 30 diffusion directions and b-values up to 600 s/mm^2 seems appropriate for renal DKI.

To identify the parameters of the optimal sequence, cortico-medullary differentiation on MK maps are used. With the radially oriented structure of the medulla in kidneys composed of tubules, differences in diffusion kurtosis as a directional measure are expected. Previous studies reported a better characterisation of tissue microstructure with kurtosis measurements in the brain [6, 51, 11, 145]. Therefore one can expect that DKI parameters might differ between the renal cortex and medulla. The MK of the cortex was constantly higher than that of the medulla in all four sequences. While the present study concentrates on the non-Gaussian analysis of the biological tissue microstructure using the kurtosis method, various groups did report results based on other higher diffusion models. As for example in a novel framework combining diffusion kurtosis and bi-exponential tensor analysis, Grinberg et al. [146] could highlight the non-Gaussian behaviour of water diffusion in human brain tissues using an extended range of b-factors (up to $7000\ s/mm^2$). However, this experimental method is not yet clinically feasible due to the long total acquisition time necessary to get sufficient SNR in particular in kidney imaging. Moreover, the biexponential behaviour of the diffusion MR signal in kidneys was shown before [145] and should be investigated in terms of tensorial analysis in future studies.

In a recent study, Lanzman et al. [147] could already highlight the potential of DT imaging for non-invasive functional assessment of transplanted kidneys. They could show significant differences in FA values of the medulla between allograft recipients with heavily impaired renal function and those with moderate or mild impairment in their renal function. Comparing MK values of normal kidneys with those of patients with various renal diseases may help to evaluate the clinical significance of renal kurtosis values and the role of the renal DKI. For instance, in renal cancer DKI may provide additional diagnostic information. Recently, Raab et al. [11] applied DK imaging in glioma and could differentiate between tumour grades using MK maps. Although the exact underlying meaning of the kurtosis findings could not yet be explained entirely these previous findings support the potential of DKI to reveal additional information to pathological alterations of the renal tissue.

Since DKI has been proven to be more sensitive to tissue microstructure in comparison to ADC and FA measures, DKI of the kidney might provide useful information for the investigation of the kidney is situation of tumours, renal transplants, or even for therapy control.

The study has some limitations. First, navigator-triggering was not possible due to technical limitations so that a respiratory belt had to be used. In clinical routines, the application of the respiratory belt-type sensor may be suboptimal. Furthermore, respiratory movements of the kidney mainly occur in the cranio-caudal direction, and therefore do not always match with the abdominal wall movements. An approach that might further help to reduce motion artefacts would be the use of navigator-echo type respiratory triggered acquisitions. They could help monitoring diaphragmatic motion and therefore decrease misregistration [63]. Due to technical

difficulties on the MR scanner, this acquisition technique could not be integrated in the respiratory triggered DWI protocol.

Second, the study was conducted on young healthy volunteers who were able to perform normal regular breathing. The results might differ in older subjects, patients in pain and patients who are less cooperative, having difficulties following a respiratory triggered acquisition.

Furthermore, the hydration status of the kidney was not controlled in this study. It is known that renal diffusion properties vary with water load. The influence of water load on the renal diffusion kurtosis still has to be investigated [136].

However, although the water load was not controlled, measurements of the reproducibility showed stable results of MK and FA within the error bounds. Further studies including patients with renal diseases should be conducted.

In summary, DKI of human kidneys is feasible. The use of 4 signal averages seems adequate in order to obtain good image quality when 3 b-values of 0 s/mm^2, 300 s/mm^2, 600 s/mm^2 and 30 diffusion directions are used. This study clearly indicates differences in kurtosis parameters corresponding to the medulla and cortex regions.

Chapter 7

Optimisation of MRI acquisition parameters for DKI in human kidneys

Previous studies revealed that optimising the set of diffusion imaging parameters can have a considerable influence on the precision of the estimated Diffusion-Weighted Imaging (DWI) parameters [148, 51]. For DKI, it is advantageous to acquire multiple b-values in order to achieve good data modelling to the signal decay [148, 68]. At least 15 encoding directions are required for DKI, but an increase in diffusion direction might improve the accuracy of the tensor calculation [149, 150]. In the human brain, actual reports have shown that 20 motion probing gradient (MPG) directions with 3 b-values (0, 1000, 2000 s/mm^2) might be optimal for an adequate accuracy of the DKI computation [148].
Referring to Yoshikawa et al. [142] who already mentioned the suitability of human kidneys for the application of DWI due the presence of anisotropy in important anatomic renal structures such as tubules that are radially orientated, the feasibility of DKI was demonstrated during this thesis (see chapter 6). While the diffusion parameter sets used have been optimised for DKI acquisitions in the human brain [125], for renal DKI it is still unclear which number of diffusion encoding directions and which range of b-values should be chosen for accurate calculation of diffusion kurtosis parameters.

In this chapter, experiments are carried out to optimise b-values and the number of encoding directions for DKI of human kidneys. These experiments are divided in two steps:

- In a first step, data sets required for the optimisation are acquired.
- In a second step, processing of the DW volumes is performed on the interesting combinations of choice and number of b-values and number of encoding directions for the DKI computation and the results are extracted.

7.1. Study population and MRI image acquisition

The institutional review board approved the study and written informed consent was obtained from all volunteers. Eight healthy volunteers (4 men, 4 women; mean age 25.70 $\pm$ 3.26 years; range 22 years - 30 years) with no history of kidney disease, diabetes, vascular disease, previous renal surgery, or any known systemic disease potentially involving the kidneys participated in the study. The examination was performed without any preparations as fasting or drinking before.

All the volunteers were examined on a clinical 3T whole-body MRI scanner (Magnetom Trio a TIM system; Siemens Medical Systems, Erlangen, Germany) using a 6 channel phased array body coil and a 24 channel phased array spine coil integrated into the scanner table. For DKI, a single-shot EPI sequence was applied in the coronal plane using respiratory triggering via a respiratory belt. For the measurements, 30 diffusion directions and 7 b-values between 0 - 1500 s/mm^2 (0, 250, 500, 750, 1000, 1250, 1500 s/mm^2) were considered. For comparison purposes, the same acquisitions process was repeated with a reduced set of 20 diffusion directions and 7 b-values between 0 - 1500 s/mm^2 (0, 250, 500, 750, 1000, 1250, 1500 s/mm^2). The other imaging parameters were as follows: field of view (FOV) $=$ 400 mm, echo time (TE) $=$ 98 ms, repetition time (TR) $=$ 1500 ms, matrix $=$ 192 $\times$ 192, 10 slices with a slice thickness of 6 mm and a resolution of 2.1 $\times$ 2.1 mm considering 2 averages. GRAPPA (generalised auto-calibrating partially parallel acquisition) as parallel imaging method accelerated at a factor of 2 was used. Since a respiratory belt was used the respiratory rate of each individual and the acceptance window's length for the belt position at each respiratory cycle influenced the acquisition time. The mean scan time was 23 min 18 s.

7.2. Data processing

Initially, all the acquired datasets were transferred to a workstation and motion correction was applied to the diffusion-weighted (DW) data using a diffeomorphism (see section 4.1.1.1) based registration approach implemented in the software fMRLung 3.0 (Siemens Corporate Research, Princeton, NJ, USA) [151, 152].

Furthermore, the scalar measures of DKI were calculated using DKE software [51, 144]. The constrained linear least square (CLLS) formulation of the kurtosis model and the conventional diffusion model used to fit the signal intensities S on a voxel-by-voxel basis are introduced in equations (3.23) and (3.7). Details about the processing pipeline used can be found in section 4.3.

For region-of-interest (ROI) analyses on mean diffusion (MD), fractional anisotropic (FA) and mean kurtosis (MK), one continuous ROI was delineated over the cortex, covering the whole cortex [56]. Four separate ROIs were positioned in four medullar areas on the parametric maps (figure 7.1). All ROI placements were performed on the $b = 0$ images in each subject and successively copied to the corresponding positions on the MD, FA and MK maps. The b_0 image was chosen for the measurements because of their higher SNR compared to DW images [137]. For analysis, the right kidney was selected because it is less prone to cardiac and respiratory motion artefacts since the liver is placed above it [138]. Mean MD, FA and MK values respectively of the ROI on the cortex and as averaged values of the ROIs on the medulla were computed and used to evaluate the different measurement protocols (see table 7.1).

7.2.1. Statistical analysis

Statistical analysis was performed with the statistics toolbox in MATLAB (Version: 8.0.0.783 (R2012b)). For all the tests a p-value < 0.05 indicated statistically significant difference. Using analysis of variance (ANOVA) with the Tuckey's honestly significant difference (HSD) post-hoc test, the effect of b-values and MPG directions schemes on renal MK in medulla and cortex was examined.

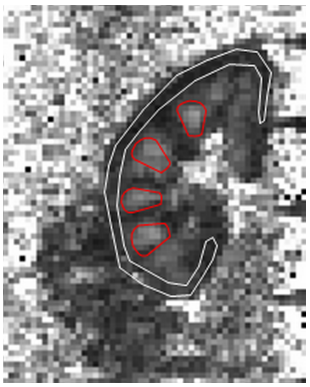

Figure 7.1.: ROIs placed on fractional anisotropy map for evaluating ADC, FA and MK values in renal cortex and medulla. (renal cortex (white), medulla (red)).

Table 7.1.: Overview of the different evaluation schemes.

Sequence	*N° of averages*	*b-values* (s/mm^2)	*N° of MPG directions*
Protocol 1	2	0, 250, 500	30
Protocol 2	2	0, 500, 750	30
Protocol 3	2	0, 500, 1000	30
Protocol 4	2	0, 750, 1250	30
Protocol 5	2	0, 250, 750, 1250	30
Protocol 6	2	0, 500, 1000, 1500	30
Protocol 7	2	0, 500, 1000	20

7.3. Selecting the Diffusion-weighted Gradient and diffusion direction Subsets

The DKI datasets were partitioned and grouped to evaluate the influcence of DWI schemes. More specifically, diverse combinations of three (protocols 1 - 4, 7) and four (protocols 5 and 6) b-values sets were chosen from the complete dataset with 7 b-values at 30 diffusion directions to study the influence of the diffusion strength. Seven protocols using different b-values and number of encoding directions were examined (table 7.1). Protocol 1 used 3 b-values, $b = 0, 250, 500$ s/mm^2, as proposed by Pentang et al. [98]. For protocol 2 - 4, a combination that used all the three higher b-values than those in protocol 1 was prepared, in order to compare this protocol with mean diffusional kurtosis values and their standard deviation (SD) [148]. To study the influence of the number of diffusion encoding directions, the mean and SD values of the ROIs on MD, FA and MK maps of the protocols 1 - 6 were compared. The protocol with the best cortico-medullary differentiation and lowest number of b-values at 30 directions was then compared to the same b-value scheme at 20 directions (refer to table 7.1). This was the protocol 7. The other imaging parameters were the same as for the b-values protocols.

7.4. Evaluating the performance of different acquisition schemes

To identify the most efficient acquisitions parameters for clinical DKI of the kidneys (10 min of measurement time), the following experiments were performed.

7.4.1. Experiment#1: Influence of the choice of b-values on derived DKI parameters

Here the accuracy and variability of the values set in ROIs on the diffusion maps is compared to assess how the choice of b-values influences the quality of DKI estimation. The resulting values are compared with previous published reports. The comparison is performed with the datasets based on 30 diffusion directions. This is the most used number of diffusion directions in the literature for a DKI acquisition [9, 98] and considering protocols 1 - 4. Regional DW values are computed from the eight complete DKI datasets of the volunteers. Different b-value subsets considering 30 diffusion directions are then selected from each of the eight complete DKI datasets to recreate the $\mathbf{D_T}$ and $\mathbf{K_T}$ using equations (3.23) and (3.7). The mean and SD for each diffusion parameter are then calculated. The aim of this experiment is to find out the best combination of b-values DKI estimation at highest accuracy.

7.4.2. Experiment#2: Influence of numbers of b-values chosen on the variability of DKI estimation

The accuracy of diffusion and kurtosis parameter estimates from the choice of the number of b-values was studied in this experiment. The goal of this experiment was to understand whether the increased number of b-values is useful for an accurate DKI calculation. Only the optimal b-value schemes from Experiment#1 were considered along with the 30 diffusion directions for every DKI dataset. Assessment was again based on comparison of mean and SD of the diffusion maps. Here the aim is to achieve practical clinical acquisition time of $\sim$ 10 min with accurate results.

7.4.3. Experiment#3: Evaluating the performance of the optimal b-value acquisition scheme considering different numbers of diffusion encoding directions

The effect of the number of MPG directions on renal DKI measures was determined based on the optimal imaging schemes from Exp#1 and Exp#2. This was the optimal $\sim$ 10 min scheme with 30 diffusion directions, $b = 0, 500, 1000$ s/mm^2. Here the number of diffusion directions were varied from 30 to 20 and the mean and SD values in cortex and medulla were analysed. The goal was to understand whether the reduced number of MPG directions would impact renal DKI estimation.

Statistical tests were performed using the curve fitting and statistics toolbox in MATLAB (Version: 8.0.0.783 (R2012b)). For all the tests a p-value < 0.05 indicated statistically significant difference. Additionally, repeated-measures analysis of variance (ANOVA) with the Tuckey's honestly significant difference (HSD) post-hoc test was used to examine the effect of the choice and number of b-values and diffusion direction on MK values.

7.5. Results

Image acquisition was performed successfully in all subjects. Parametric maps of MD, FA and MK are shown exemplary for one volunteer on figure 7.2

Table 7.2 shows the mean and SD of MD, FA and MK for each protocol evaluated, as representative of cortex and medullary regions. No statistically significant difference was found in MD values of cortex and medulla comparing the four protocols with 3 b-values in cortex (2.13 $\pm$ 0.10 $\times$ 10^{-3} mm$^2/s$ – 2.42 $\pm$ 0.18 $\times$ 10^{-3} mm$^2/s$) and medulla (2.04 $\pm$ 0.10 $\times$ 10^{-3} mm$^2/s$ – 2.22 $\pm$ 0.22 $\times$ 10^{-3} mm$^2/s$).

In contrast, FA of the cortex (0.16 $\pm$ 0.05 – 0.18 $\pm$ 0.05) was significantly lower than in the medulla (0.37 $\pm$ 0.08 - 0.43 $\pm$ 0.07) in all b-values schemes ($p < 0.05$).

For MK, the two first protocols (protocol 1: b = 0, 250, 500 s/mm^2; protocol 2: b = 0, 500, 750 s/mm^2) showed higher values in the cortex compared to the medulla using 500 s/mm^2 or 750 s/mm^2 as highest b-values. Additionally, MK values in protocol 1 were higher as in protocol 2. SD of MK values was higher in protocols with 500 s/mm^2 or 750 s/mm^2 as maximum b-values. Only the b-value sets with highest values of at least 1000 s/mm^2 (protocol 3: b = 0, 500, 1000 s/mm^2; protocol 4: b = 0, 750, 1250 s/mm^2) resulted in lower cortex values compared to medullary values in MK as expected from the kidney's anatomy regarding isotropic or anisotropic diffusion. At this point, the MK values of protocol 3, b = 0, 500, 1000 s/mm^2 reflecting the more anisotropic nature of medulla (0.71 $\pm$ 0.06) compared to cortex (0.66 $\pm$ 0.05) showed clear advantage compared to protocol 1 and 2. For protocols 3 and 4, the differences between the various choices of b-values increasing the maximum b-value to 1250 s/mm^2 were small.

Table 7.2.: Quantitative assessment of MD ($\times$ 10^{-3} mm$2/s$), FA and MK considering 30 diffusion encoding directions at different b-values schemes.

Protocol	*MD* ($\times 10^{-3} mm^2/s$)		*FA*		*MK*	
N°a	*Cortex*	*Medulla*	*Cortex*	*Medulla*	*Cortex*	*Medulla*
1	2.42 $\pm$ 0.18	2.22 $\pm$ 0.22	0.17 $\pm$ 0.05	0.42 $\pm$ 0.06	1.02 $\pm$ 0.19	0.91 $\pm$ 0.04
2	2.38 $\pm$ 0.17	2.11 $\pm$ 0.20	0.17 $\pm$ 0.05	0.43 $\pm$ 0.07	0.76 $\pm$ 0.07	0.70 $\pm$ 0.05
3	2.41 $\pm$ 0.12	2.21 $\pm$ 0.22	0.18 $\pm$ 0.05	0.41 $\pm$ 0.07	0.66 $\pm$ 0.05	0.71 $\pm$ 0.06
4	2.13 $\pm$ 0.10	2.04 $\pm$ 0.10	0.16 $\pm$ 0.05	0.37 $\pm$ 0.08	0.61 $\pm$ 0.06	0.66 $\pm$ 0.06
5	2.85 $\pm$ 0.30	2.54 $\pm$ 0.29	0.22 $\pm$ 0.06	0.47 $\pm$ 0.09	0.74 $\pm$ 0.03	0.82 $\pm$ 0.02
6	2.22 $\pm$ 0.18	2.10 $\pm$ 0.12	0.16 $\pm$ 0.05	0.43 $\pm$ 0.06	0.63 $\pm$ 0.03	0.66 $\pm$ 0.03

Protocol 1: 0, 250, 500

Protocol 2: 0, 500, 750

Protocol 3: 0, 500, 1000

Protocol 4: 0, 750, 1250

Protocol 5: 0, 250, 750, 1250

Protocol 6: 0, 500, 1000, 1500

[a] Each protocol number contains the following b-values [s/mm^2]

Table 7.2 shows mean and SD of MD, FA and MK with various number of b-values (3 b-values: protocol 3: b = 0, 500, 1000 s/mm^2; protocol 4: b = 0, 750, 1250 s/mm^2, (4 b-values: protocol 5:

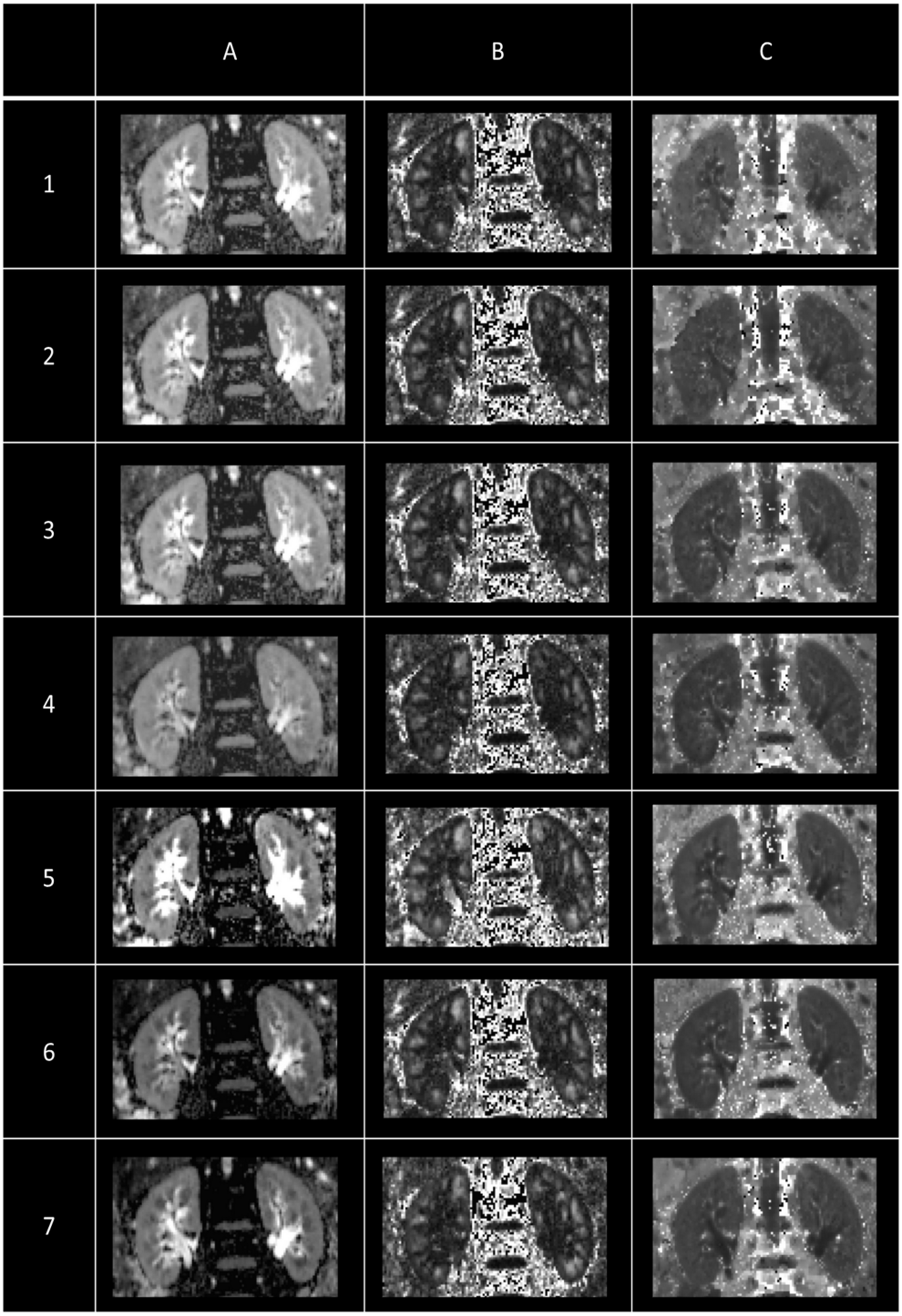

Figure 7.2.: From left to right, A: mean diffusivity (MD), B: fractional anisotropy (FA), and C: mean kurtosis (MK) maps of the kidney of a healthy volunteer with 30 diffusion directions: Top row (Protocol 1): 0, 250 , and 500 s/mm^2, 2^{nd} row (Protocol 2): 0, 500 , and 750 s/mm^2, 3^{rd} row (Protocol 3): 0, 500 , and 1000 s/mm^2, 4^{th} row (Protocol 4): 0, 750, and 1250 s/mm^2, 5^{th} row (Protocol 5): 0, 250, 750 and 1250 s/mm^2, 6^{th} row (Protocol 6): 0, 500, 1000, and 1500 s/mm^2 and with 20 directions 7^{th} row (Protocol 7) considering b-values: 0, 500, and 1000 s/mm^2.

b = 0, 250, 750, 1250 s/mm^2; protocol 4: b = 0, 500, 1000, 1500 s/mm^2). Increasing the number of b-values from three to four brought no additional information regarding the cortico-medullay differentiation in MK values. However, there was a little decrease in the MD values using low b-values of 250 s/mm^2 (see protocol 1 and 5) probably due to perfusion effects. Using very high b-values of 1500 s/mm^2 revealed increase in MD values. Whereas the high SD of MD noticed in protocol 6 could result from noise accompanying low SNR at high diffusion-weighting. From experiment#1 and experiment#2, protocol 3 with a combination of 30 diffusion directions and 3 b-values was chosen as the best protocol.

Repeated-measures analysis of variance by one-way ANOVA showed that there was a statistically significant difference in the MK values in the cortex ($F(5,6) = 963.87$, $p < 0.05$)) and medulla ($F(5,6) = 439.07$, $p < 0.05$)) depending on the choice of b-values. Post-hoc Tukey HSD demonstrated significant differences between protocol 1 and the protocols 2, 3, 4 and 6 showed statistical significant difference in medullary and cortical MK ($p < 0.05$).

After experiment#3, no statistically significant difference ($p > 0.05$) was found for MD, FA when comparing 20 and 30 MPG directions using the b-values 0, 500, 1000 s/mm^2 in protocols 3 and 7 (see Tables 7.1 and 7.3) indicating the advantage of reducing the number of directions. For MK, the cortex values were significantly different from the medulla values with 20 directions ($p = 0.02$) and with 30 directions ($p = 0.01$).

Table 7.3.: Quantitative assessment of MD ($\times$ 10^{-3} mm^2/s), FA and MK considering b-values (0, 500 and 1000 s/mm^2) at different number of MPG directions.

N° of MPG	*Scanning*	*MD* ($\times 10^{-3} mm^2/s$)		*FA*		*MK*	
direction	*time*	*Cortex*	*Medulla*	*Cortex*	*Medulla*	*Cortex*	*Medulla*
20	8 min:35 s	2.52 $\pm$ 0.18	2.49 $\pm$ 0.24	0.22 $\pm$ 0.04	0.42 $\pm$ 0.09	0.74 $\pm$ 0.06	0.79 $\pm$ 0.07
30	9 min:59 s	2.41 $\pm$ 0.12	2.21 $\pm$ 0.22	0.18 $\pm$ 0.05	0.41 $\pm$ 0.07	0.66 $\pm$ 0.05	0.71 $\pm$ 0.06

Protocol 3: 30 MPG directions, b-values (0, 500, 1000),

Protocol 7: 20 MPG directions, b-values (0, 500, 1000)

7.6. Discussion

High b-values in DKI, meaning increasing the weighting by diffusion in DWI, allows the monitoring of water molecule movement at a microscopic scale and hence make the DW sequence very sensitive to the tissue microstructure. However, depending on the number of diffusion-weightings and directions used, the scans can be very long and sometimes are clinically impractical.

Respiratory triggered acquisitions were used to analyse the influence of acquisition parameters in terms of b-values and number of diffusion encoding directions on renal DKI parameters with the focus on clinically feasible acquisition times. The experiments performed in this study demonstrate that an efficient DKI imaging scheme with only two non-zero b-values (500 and 1000 s/mm^2) and 20 diffusion directions can provide accurate DKI values in a clinically feasible time.

Here the mean MK values were lower in cortex (0.74 $\pm$ 0.06) compared to medulla (0.79 $\pm$

0.07). Quantitative evaluation using 0, 500 and 1000 s/mm^2 as b-values and 20 MPG directions showed comparable mean values for MD (in cortex from 2.52 $\pm$ 0.18 $\times$ 10^{-3} mm^2/s and medulla from 2.52 $\pm$ 0.24 and FA (in cortex from 0.22 $\pm$ 0.04 and in medulla 0.42 $\pm$ 0.09) as previously published [148, 56, 136, 57, 61].

For depiction of the non mono-exponential decay of the fitting curve, b-values should be usually higher than those employed in DTI.

Additionally an increase of DW directions that implies longer acquisition times might lead to more accurate measurement of diffusion [63]. The first study [98] applying DKI in human kidneys used 30 diffusion directions and a maximum b-value of 600 s/mm^2 (b-values: 0, 300, 600 s/mm^2); that is the lower bound from which the departure from the Gaussian model is observed [98]. Here the authors demonstrated feasibility of renal DKI in healthy humans reporting MK values of 0.94 $\pm$ 0.07 in the cortex and 0.78 $\pm$ 0.07 in the medulla. Although still not proven, this study also supports their findings using a comparable protocol with 0, 250 and 500 s/mm^2 as b-values resulting in the case of this study to cortical MK values between 0.76 $\pm$ 0.07 and 1.02 $\pm$ 0.19 and medullary MK values between 0.70 $\pm$ 0.05 and 0.91 $\pm$ 0.04. Although, this finding was contradictory with the knowledge that the renal medulla is more anisotropic than cortex [136, 57]. Indeed, the choice of the maximum b-value should be based on the diffusivity and kurtosis value of the studied tissues. In the normal human brain, it is assumed that $D \approx 1 \times 10^{-3}$ mm^2/s and $K \approx 1$, and the recommended DKI protocol for brain uses 2000 s/mm^2 as the maximum b-value. For the healthy human kidneys, $D \approx 2 \times 10^{-3}$ mm^2/s has been reported. Using similar b-values as in the brain would lead to a very low SNR in renal diffusion values. This justified the choice of analysing b-values schemes using maximum diffusion-weighting of at least 1000 s/mm^2/s as in protocols 3, 4, 5 and 6.

The reported MK values of 0.74 $\pm$ 0.06 in the cortex and 0.79 $\pm$ 0.07 in the medulla using the protocol 7 with b-values: 0, 500 and 1000 mm^2/s were higher than findings of a study by Huang et al. [153] using a comparable protocol reporting lower MK values in the cortex (0.377 $\pm$ 0.16) compared to the medulla (0.561 $\pm$ 0.07). These differences might be explained by the influence of blood flow on diffusion coefficients [143].

The regional analyses indicate that increasing the number of b-values does not reduces the variability in the calculated DKI measures. However, maximum b-values would directly impact the estimation of DKI scalar measures. The mean kurtosis parameters estimated with a maximum b-value of at least 1000 s/mm^2 were more accurate compared to the those calculated with a maximum b-value of 500 s/mm^2 or 750 s/mm^2. Then again, even if diffusion measures as the MD more depend on the b-value [129], in DKI they are not influenced by the choice of the maximum b-value. This supports the results of Veraart et al. [154]. They reported namely that DTI measures are more exactly estimated with the DKI model [154]. Even though a maximum b-value of 1500 s/mm^2 is preferred compared to 1000 s/mm^2, renal diffusion-weighted images at b-value of 1500 s/mm^2 have a very low signal intensity and are more susceptible to noise.

As already stated above, an increased number of MPG directions would lead to more reliable diffusion maps. Indeed feasibility of renal DKI was demonstrated in previous studies with 30 diffusion directions as proposed by Jensen et al. [9]. In this study, the optimal set of b-values (0, 500 and 1000 s/mm^2) was kept stable and experiments were carried out to evaluate whether a reduction in number of directions (30 to 20 directions), would impact the clinical utility of DKI in kidneys. The findings indicate that for DKI of the kidney at 3T with 20 diffusion directions, medullary values (0.79 $\pm$ 0.07) are higher than cortex values (0.74 $\pm$ 0.06) thus reflecting the more anisotropic structure in medulla compared to cortex ($p = 0.02$). Although increasing the number of MPG directions to 30 showed a more pronounced cortico-medullary differentiation

($p = 0.01$), focus was either laid on reduced scanning times at 20 directions compared to 30 therefore increasing the practicable feasibility of clinical renal DKI. Future studies could use the optimal set of b-values presented here to investigate impact of number of MPG directions inferior to 20 on renal DKI measures with the aim of reducing the acquisition time.

In addition to the limitations of the study described in chapter 6 regarding navigator-triggering and the hydration status, comparing MK values of normal kidneys with those of patients with various renal diseases may help to evaluate the clinical significance of renal kurtosis values and the role of renal DKI. A recent study of Lanzman et al. [147] could already highlight the potential of DT imaging for non-invasive functional assessment of transplanted kidneys .

This study establishes optimal and efficient DKI imaging parameters ($b = 0$, 500, 1000 s/mm^2 and 20 diffusion directions) that requires only $\sim$ 8 min to obtain data from the human kidneys. Lower maximum b-values resulted in underestimation of non-Gaussian behaviour of water diffusion, and inclusion of low b-values in the analysis has the potential to increase cortico-medullary differentiation. Because it helps to discriminate slow diffusion from fast diffusion in the renal tubules and collecting ducts, they respectively result in higher MD values compared to other diffusion evaluation schemes. In conclusion, the set of b-values and number of MPG directions influences renal DKI parameters while keeping DTI indices quite stable. The diagnostic value of DKI for evaluation of kidney diseases will have to be assessed in further studies.

Chapter 8

Summary and Outlook

There were two main goals for this thesis. The first was to develop the necessary image reconstruction pre-processing tools and imaging protocols for practical use of Diffusion Kurtosis Imaging (DKI) in the clinical routine, while still preserving as much information as possible. The second goal of this dissertation was to assess the feasibility of DKI, as a recently developed imaging technique, in detecting biological tissue microstructure in the healthy human brain and kidneys.

8.1. Technical Developments

In the first section of chapter 4 a robust image pre-processing pipeline for motion correction in diffusion-weighted (DW) images prior to DKI reconstruction was designed, implemented and tested. The conventional way of motion correction in DW images consist in registering only the non-DW images (b_0 images) of an acquisition to the first b_0 image and applying the resulting transformation parameters on all the other DW images [82, 129]. The similarity measurement between the *moving image* and *reference image* is based on cross-correlation (CC) metrics or mean squared intensity difference (MSQ). This method although often applied is inappropriate not only because it just uses the spatial transformation between b_0 images in the registration process neglecting diffusion-weighting, but also because the contrast of the *source* and *reference images* differs significantly in DKI, thus making the use of CC and SSID similarity measures non-efficient for alignment of images with changing contrast. The present thesis used mutual information (MI) - a basic concept of information theory - as a similarity measure to improve motion correction of DWI/DKI images. The use of MI requires no specification about the geometry between the two images and is not based on the comparison of the grey values but either considers their entropy. From the methods tested, the Mattes-implementation of the mutual information was used and all the DW images were registered to the first b_0 image prior to DKI computation. The resulting registration process retrospectively corrects for motion prior to DKI computation and provides maps of quantities derived from the kurtosis tensor that are more anatomically accurate.

Even with motion corrected DW images, DKI is still highly subject to errors due to noise. The effect of noise on DKI estimation appears to be mainly due to an increased likelihood of erroneous fitting of data with low SNR. Kurtosis parameters are more susceptible to noise than diffusion parameters because it is easier to violate the kurtosis value constraints. Mean kurtosis (MK) and radial kurtosis K_{RAD} tend to be underestimated, while axial kurtosis (K_{AX}) is overestimated

as SNR is reduced. In the second section of chapter 4 state-of-the art noise reduction schemes were reviewed, investigated and analysed. For this purpose, synthetic DW data corrupted with noise were used to compare two different Rician noise reduction algorithms based on standard well-known quantitative (NRR, MSSIM, PSNR) and qualitative metrics. The results achieved with the joint LMMSE filter demonstrate the necessity of applying a noise reduction filter on DWI images prior to DKI computation.

In chapter 7 after proving the feasibility of DKI in human kidneys (see chapter 6), experiments were performed to investigate the influence of the choice and number of b-values and diffusion directions on renal DKI. The results were optimised and efficient acquisition parameters ($b = 0$; 500; 1000 s/mm^2 and 20 diffusion directions) for DKI of human kidneys were established.

8.2. Clinical contributions

Recent studies suggest that Diffusion Kurtosis Imaging (DKI) is more sensitive to brain microstructure than the well-known Diffusion Tensor Imaging (DTI) [6]; in particular in tumour micro-environments where DKI can increase diagnostic confidence [11]. DKI brain atlases might further improve understanding of brain microstructure. In chapter 5, the first age- and gender-dependent MRI whole human brain atlases of healthy subjects on the basis of diffusion kurtosis and diffusion tensor data at 3T were developed. The variability of the diffusion indices were evaluated in 80 human brains with the great advantage of being mapped to the existing well-established anatomical Montreal Neurology Institute (MNI) template. The resulting atlases with high-resolution, full brain coverage in a large number of subjects showed age correlation in FA, MK and K_{RAD}. This study revealed that the demyelination process is more pronounced in MK maps compared to FA maps. These atlases may serve in the future as standard reference values for comparison with changes associated with development, aging and pathologies in human brains.

DKI has so far been applied to human and small animal brain studies. Non-Gaussian Diffusion-Weighted imaging (DWI), not determining the complete kurtosis tensor, was rarely used in abdominal organs [120]. The anisotropy of renal tissues makes the human kidneys suitable for the application of DKI. In chapter 6, DKI was applied for the first time in healthy human kidneys using respiratory triggered acquisitions at 3T. Feasibility and reproducibility was assessed for renal DKI. MK and Fractional anisotropy (FA) values were different in cortex compared to medulla.

8.3. Future Directions

Beyond the contributions of this thesis, there are still several challenges ahead. The DKI imaging technique is currently being applied in the human brain [6, 9, 145], kidneys [98], prostate [155], spinal cord [156]. Other body regions such as intervertebral discs (IVDs) were already examined for DWI feasibility [157], therefore it could be interesting to model the signal in IVDs and other musculoskeletal body regions with the DKI model. Additionally, Sinkus et al. [158] could use DTI measurements to distinguish between benign and malignant breast diseases. Feasibility of DKI for mammography should be investigated as using the new and additional information provided by DKI could help to improve breast tumour detection.

As an extension of the experiments in chapter 7, the influence of less diffusion directions, inferior to 20, on renal DKI could be investigated. Here the effect of image noise should also be considered. Furthermore, optimising kurtosis imaging acquisitions parameters for specific

regions of the human body would be of great interest to improve accuracy of resulting parameter maps.

Moreover comparing MK values of normal kidneys with those of patients with various renal diseases may help to evaluate the clinical significance of renal kurtosis values and the role of the renal DKI. For instance in renal cancer, DKI may provide additional diagnostic information.

A single-shot EPI sequence was used for DKI data acquisition in this thesis. Aside from the relatively low spatial resolution, EPI data are prone to various artefacts, in particular, susceptibility artefacts and geometric distortions [134]. An approach that might further help to increase the resolution of DW acquisitions and to reduce the susceptibility and blurring artefacts would be the use of readout-segmented muti-shot EPI sequences in DKI. This technique provides significant image quality improvement compared with DW single-shot EPI at 3T [135].

Conclusion

The most significant original contributions of this thesis are the design and implementation of a motion correction software prior to DKI estimation for brain data, the construction of a healthy whole human brain atlas based on DTI and DKI maps *in vivo*, the demonstration that DKI can be applied in human kidneys and the optimisation of acquisition parameters for renal DKI. The developed pre-processing tools such as image registration and noise filtering are able to improve non-Gaussian *in vivo* DWI / DKI measurements in humans. The results may then serve as a basis for the practical use of DKI in clinical studies.

Appendix

A. Landmarks

Landmarks x-, y-, z-, brain coordinates. (Refer to chapter 5 - Figure 5.1)

Landmarks	*(x y z) MNI coordinates*	*Mean Distance (mm)*	*SD of Distance (mm)*
1	(37 35 45)	0.11	0.33
2	(53 35 45)	0.25	0.74
3	(33 67 45)	1.28	1.14
4	(56 68 45)	0.96	0.58
5	(45 74 38)	2.77	1.06
6	(31 66 38)	0.78	1.09
7	(59 68 38)	0.33	0.71
8	(45 46 31)	0.22	0.67
9	(45 65 31)	0.11	0.33
10	(45 64 24)	0.11	0.33
11	(28 46 24)	0	0
12	(61 48 24)	0	0
13	(44 48 28)	1.21	1.61
14	(44 59 43)	0	0
15	(44 82 32)	0	0
16	(44 69 21)	0.69	0.91
17	(44 38 40)	1.27	1.39
18	(44 70 11)	0.69	1.04
19	(44 89 26)	2.31	2.4
20	(44 50 13)	0.36	0.78
21	(44 10 49)	0.22	0.44
22	(44 81 66)	0	0
23	(44 30 70)	0	0
24	(38 13 35)	3.81	3.05
25	(37 55 52)	0.87	1.06
26	(53 55 52)	0.99	0.88
27	(45 55 52)	0	0
28	(52 62 46)	1.21	1.15
29	(35 62 46)	0.36	0.78
30	(44 62 39)	0.49	0.78

Table .2.: Mean and SD of the distance between the landmarks in the reference brain and individual subjects.

Subjects	Mean Distance (mm)	SD of Distance (mm)
1	0.00	0.00
2	0.66	1.03
3	1.08	1.27
4	1.23	1.79
5	0.97	1.87
6	0.64	1.28
7	0.72	1.25
8	0.25	0.65
9	0.76	1.35
10	0.10	0.55

B. Atlases

Age-dependent atlases developed in chapter 5.

Table .3.: Resulting atlases respectively for the the 20YG

20YG	MD $[\mu m^2/ms]$	FA	MK	K_{AX}	K_{RAD}
ALIC	0.73 ± 0.06	0.48 ± 0.05	1.00 ± 0.07	0.89 ± 0.05	1.33 ± 0.24
Basal Ganglia	0.77 ± 0.13	0.32 ± 0.08	1.03 ± 0.11	0.89 ± 0.09	1.15 ± 0.16
Caudate	0.94 ± 0.21	0.13 ± 0.04	0.78 ± 0.14	0.80 ± 0.13	0.80 ± 0.18
CCb	0.88 ± 0.15	0.64 ± 0.04	1.25 ± 0.22	0.68 ± 0.08	2.13 ± 0.46
CCg	0.87 ± 0.10	0.75 ± 0.06	1.58 ± 0.32	0.64 ± 0.04	2.47 ± 0.49
CCs	0.82 ± 0.15	0.78 ± 0.06	1.71 ± 0.36	0.65 ± 0.06	2.49 ± 0.40
Cent. Sem.	0.71 ± 0.02	0.51 ± 0.03	1.14 ± 0.07	0.89 ± 0.04	1.62 ± 0.18
Cereb. ped.	0.77 ± 0.13	0.68 ± 0.06	1.41 ± 0.22	0.68 ± 0.05	2.10 ± 0.46
Cing. temp.	0.74 ± 0.09	0.43 ± 0.07	1.17 ± 0.11	0.98 ± 0.11	1.66 ± 0.38
Cingulate	0.73 ± 0.13	0.39 ± 0.09	1.03 ± 0.18	0.94 ± 0.10	1.26 ± 0.54
Corona Rad.	0.70 ± 0.07	0.56 ± 0.05	1.25 ± 0.08	0.74 ± 0.06	1.71 ± 0.20
Cortex	0.82 ± 0.09	0.24 ± 0.05	0.84 ± 0.13	0.80 ± 0.08	0.91 ± 0.21
Ext. caps.	0.73 ± 0.07	0.53 ± 0.07	1.01 ± 0.12	0.87 ± 0.06	1.47 ± 0.35
Fornix	1.15 ± 0.03	0.26 ± 0.06	0.72 ± 0.04	0.60 ± 0.05	0.82 ± 0.07
FWM	0.73 ± 0.03	0.44 ± 0.03	1.13 ± 0.14	0.89 ± 0.07	1.38 ± 0.25
Mesenc.	0.83 ± 0.13	0.39 ± 0.06	1.16 ± 0.16	0.88 ± 0.06	1.38 ± 0.26
Pallidium	0.78 ± 0.08	0.20 ± 0.05	0.91 ± 0.14	0.99 ± 0.07	0.84 ± 0.19
PLIC	0.73 ± 0.09	0.60 ± 0.06	1.14 ± 0.15	0.68 ± 0.04	1.59 ± 0.43
Pons	0.79 ± 0.13	0.37 ± 0.06	1.15 ± 0.13	0.92 ± 0.07	1.41 ± 0.27
Putamen	0.73 ± 0.07	0.14 ± 0.06	1.01 ± 0.17	1.04 ± 0.12	0.99 ± 0.20
PWM	0.79 ± 0.12	0.40 ± 0.06	1.08 ± 0.08	0.84 ± 0.05	1.36 ± 0.16
Thalamus	0.82 ± 0.10	0.28 ± 0.03	1.09 ± 0.14	0.94 ± 0.09	1.21 ± 0.18
TWM	0.73 ± 0.09	0.62 ± 0.06	1.21 ± 0.13	0.67 ± 0.03	1.79 ± 0.37

Table .4.: Resulting atlases respectively for the the 30YG

30YG	MD $[\mu m^2/ms]$	FA	MK	K_{AX}	K_{RAD}
ALIC	0.71 ± 0.02	0.46 ± 0.05	1.04 ± 0.12	1.03 ± 0.13	1.39 ± 0.15
Basal Ganglia	0.72 ± 0.08	0.32 ± 0.06	1.18 ± 0.23	1.17 ± 0.23	1.37 ± 0.29
Caudate	0.81 ± 0.08	0.14 ± 0.04	0.75 ± 0.22	0.75 ± 0.22	0.76 ± 0.26
CCb	0.96 ± 0.14	0.63 ± 0.03	1.19 ± 0.17	1.12 ± 0.23	2.02 ± 0.29
CCg	0.84 ± 0.06	0.73 ± 0.05	1.54 ± 0.18	1.46 ± 0.34	2.46 ± 0.29
CCs	0.75 ± 0.06	0.81 ± 0.04	1.81 ± 0.26	1.69 ± 0.44	2.64 ± 0.23
Cent. Sem.	0.72 ± 0.01	0.49 ± 0.05	1.13 ± 0.05	1.10 ± 0.08	1.55 ± 0.20
Cereb. ped.	0.72 ± 0.04	0.69 ± 0.03	1.56 ± 0.21	1.45 ± 0.32	2.30 ± 0.27
Cing. temp.	0.73 ± 0.04	0.47 ± 0.06	1.19 ± 0.09	1.13 ± 0.16	1.90 ± 0.36
Cingulate	0.69 ± 0.02	0.35 ± 0.04	1.07 ± 0.15	1.07 ± 0.15	1.06 ± 0.28
Corona Rad.	0.68 ± 0.01	0.58 ± 0.05	1.30 ± 0.06	1.24 ± 0.20	1.82 ± 0.11
Cortex	0.85 ± 0.16	0.24 ± 0.09	0.88 ± 0.12	0.87 ± 0.14	1.01 ± 0.19
Ext. caps.	0.71 ± 0.02	0.54 ± 0.04	1.02 ± 0.15	1.01 ± 0.16	1.55 ± 0.23
Fornix	1.49 ± 0.20	0.24 ± 0.06	0.71 ± 0.05	0.70 ± 0.06	0.78 ± 0.10
FWM	0.73 ± 0.02	0.40 ± 0.04	1.03 ± 0.08	1.02 ± 0.09	1.26 ± 0.12
Mesenc.	0.78 ± 0.07	0.40 ± 0.02	1.30 ± 0.07	1.24 ± 0.15	1.60 ± 0.11
Pallidium	0.74 ± 0.04	0.23 ± 0.05	1.04 ± 0.25	1.06 ± 0.24	0.99 ± 0.30
PLIC	0.71 ± 0.01	0.61 ± 0.03	1.21 ± 0.11	1.16 ± 0.19	1.72 ± 0.25
Pons	0.74 ± 0.03	0.39 ± 0.03	1.29 ± 0.13	1.24 ± 0.16	1.64 ± 0.18
Putamen	0.71 ± 0.01	0.15 ± 0.01	0.92 ± 0.24	0.94 ± 0.24	0.88 ± 0.28
PWM	0.74 ± 0.03	0.40 ± 0.06	1.07 ± 0.06	1.05 ± 0.08	1.27 ± 0.21
Thalamus	0.78 ± 0.02	0.29 ± 0.02	1.00 ± 0.13	0.99 ± 0.13	1.11 ± 0.17
TWM	0.70 ± 0.02	0.63 ± 0.03	1.27 ± 0.08	1.21 ± 0.20	1.86 ± 0.20

Table .5.: Resulting atlases respectively for the the 40YG

40YG	MD $[\mu m^2/ms]$	FA	MK	K_{AX}	K_{RAD}
ALIC	0.76 ± 0.08	0.52 ± 0.17	0.98 ± 0.06	0.87 ± 0.03	1.20 ± 0.17
Basal Ganglia	0.76 ± 0.16	0.43 ± 0.28	1.14 ± 0.13	1.00 ± 0.15	1.29 ± 0.31
Caudate	0.98 ± 0.29	0.16 ± 0.15	0.72 ± 0.10	0.73 ± 0.11	0.72 ± 0.10
CCb	1.02 ± 0.37	0.78 ± 0.43	1.21 ± 0.33	0.79 ± 0.45	1.89 ± 0.36
CCg	0.98 ± 0.32	0.81 ± 0.38	1.39 ± 0.23	0.79 ± 0.38	2.12 ± 0.32
CCs	0.96 ± 0.49	0.92 ± 0.50	1.68 ± 0.33	0.81 ± 0.54	2.52 ± 0.28
Cent. Sem.	0.79 ± 0.22	0.57 ± 0.29	1.14 ± 0.10	0.96 ± 0.16	1.47 ± 0.08
Cereb. ped.	0.77 ± 0.15	0.74 ± 0.16	1.41 ± 0.24	0.81 ± 0.15	1.86 ± 0.40
Cing. temp.	0.84 ± 0.35	0.59 ± 0.43	1.29 ± 0.20	1.01 ± 0.30	1.78 ± 0.32
Cingulate	0.74 ± 0.03	0.36 ± 0.16	1.04 ± 0.11	1.00 ± 0.09	1.04 ± 0.17
Corona Rad.	0.76 ± 0.24	0.62 ± 0.31	1.31 ± 0.12	0.80 ± 0.23	1.78 ± 0.29
Cortex	0.86 ± 0.09	0.39 ± 0.24	0.92 ± 0.13	0.85 ± 0.13	1.01 ± 0.24
Ext. caps.	0.74 ± 0.11	0.54 ± 0.21	0.96 ± 0.15	0.88 ± 0.07	1.31 ± 0.31
Fornix	1.56 ± 0.37	0.31 ± 0.15	0.68 ± 0.04	0.60 ± 0.07	0.74 ± 0.06
FWM	0.80 ± 0.19	0.49 ± 0.30	1.09 ± 0.15	0.94 ± 0.15	1.23 ± 0.22
Mesenc.	0.86 ± 0.11	0.45 ± 0.23	1.23 ± 0.14	0.89 ± 0.10	1.45 ± 0.25
Pallidium	0.74 ± 0.04	0.25 ± 0.16	0.84 ± 0.18	0.93 ± 0.14	0.77 ± 0.23
PLIC	0.77 ± 0.19	0.67 ± 0.24	1.19 ± 0.12	0.77 ± 0.19	1.56 ± 0.29
Pons	0.86 ± 0.20	0.45 ± 0.34	1.27 ± 0.19	0.97 ± 0.16	1.53 ± 0.29
Putamen	0.72 ± 0.02	0.26 ± 0.21	0.84 ± 0.12	0.93 ± 0.11	0.78 ± 0.17
PWM	0.80 ± 0.18	0.47 ± 0.31	1.09 ± 0.11	0.95 ± 0.14	1.22 ± 0.14
Thalamus	0.87 ± 0.11	0.33 ± 0.18	0.98 ± 0.12	0.85 ± 0.11	1.04 ± 0.16
TWM	0.76 ± 0.18	0.67 ± 0.24	1.19 ± 0.13	0.73 ± 0.19	1.65 ± 0.32

Table .6.: Resulting atlases respectively for the the 50YG

50YG	MD $[\mu m^2/ms]$	FA	MK	K_{AX}	Krad
ALIC	0.79 ± 0.17	0.48 ± 0.05	0.93 ± 0.10	0.87 ± 0.05	1.06 ± 0.24
Basal Ganglia	0.72 ± 0.07	0.35 ± 0.08	1.40 ± 0.32	1.12 ± 0.21	1.61 ± 0.44
Caudate	1.01 ± 0.23	0.11 ± 0.02	0.72 ± 0.15	0.78 ± 0.13	0.68 ± 0.17
CCb	0.85 ± 0.09	0.65 ± 0.07	1.11 ± 0.23	0.65 ± 0.12	1.80 ± 0.33
CCg	0.93 ± 0.19	0.71 ± 0.07	1.23 ± 0.16	0.67 ± 0.13	2.00 ± 0.37
CCs	0.98 ± 0.64	0.78 ± 0.05	1.53 ± 0.13	0.66 ± 0.04	2.39 ± 0.23
Cent. Sem.	0.73 ± 0.03	0.48 ± 0.04	1.11 ± 0.07	0.91 ± 0.03	1.40 ± 0.18
Cereb. ped.	0.73 ± 0.06	0.66 ± 0.03	1.34 ± 0.24	0.78 ± 0.06	1.75 ± 0.35
Cing. temp.	0.76 ± 0.06	0.42 ± 0.10	1.18 ± 0.10	0.89 ± 0.10	1.70 ± 0.35
Cingulate	0.76 ± 0.13	0.30 ± 0.05	1.02 ± 0.13	1.08 ± 0.09	0.93 ± 0.22
Corona Rad.	0.69 ± 0.03	0.55 ± 0.04	1.24 ± 0.11	0.72 ± 0.06	1.73 ± 0.22
Cortex	0.91 ± 0.26	0.28 ± 0.06	0.96 ± 0.13	0.87 ± 0.12	1.04 ± 0.20
Ext. caps.	0.86 ± 0.40	0.58 ± 0.05	0.96 ± 0.18	0.84 ± 0.05	1.33 ± 0.50
Fornix	1.56 ± 0.20	0.24 ± 0.05	0.67 ± 0.09	0.60 ± 0.07	0.69 ± 0.14
FWM	0.77 ± 0.03	0.39 ± 0.04	1.12 ± 0.11	0.94 ± 0.07	1.27 ± 0.18
Mesenc.	0.94 ± 0.46	0.40 ± 0.03	1.22 ± 0.14	0.90 ± 0.05	1.35 ± 0.29
Pallidium	0.79 ± 0.04	0.20 ± 0.04	0.97 ± 0.21	1.02 ± 0.11	0.92 ± 0.28
PLIC	0.71 ± 0.03	0.60 ± 0.02	1.06 ± 0.13	0.69 ± 0.05	1.37 ± 0.29
Pons	0.79 ± 0.14	0.39 ± 0.04	1.35 ± 0.11	0.97 ± 0.06	1.65 ± 0.16
Putamen	0.85 ± 0.35	0.17 ± 0.02	0.89 ± 0.13	1.03 ± 0.10	0.81 ± 0.17
PWM	0.77 ± 0.05	0.41 ± 0.05	1.05 ± 0.06	0.91 ± 0.09	1.20 ± 0.11
Thalamus	0.89 ± 0.08	0.27 ± 0.02	0.97 ± 0.10	0.89 ± 0.08	1.03 ± 0.15
TWM	0.70 ± 0.02	0.61 ± 0.03	1.11 ± 0.13	0.69 ± 0.04	1.48 ± 0.30

Table .7.: Resulting atlases respectively for the the 60YG

60YG	MD $[\mu m^2/ms]$	FA	MK	K_{AX}	Krad
ALIC	0.74 ± 0.05	0.47 ± 0.03	0.97 ± 0.11	0.88 ± 0.04	1.11 ± 0.26
Basal Ganglia	0.70 ± 0.04	0.38 ± 0.05	1.30 ± 0.21	1.14 ± 0.12	1.45 ± 0.30
Caudate	2.25 ± 0.57	0.08 ± 0.03	0.55 ± 0.08	0.52 ± 0.09	0.56 ± 0.07
CCb	1.13 ± 0.17	0.61 ± 0.06	1.09 ± 0.12	0.61 ± 0.06	1.70 ± 0.29
CCg	0.91 ± 0.10	0.69 ± 0.05	1.37 ± 0.23	0.66 ± 0.07	2.12 ± 0.42
CCs	0.79 ± 0.11	0.76 ± 0.08	1.59 ± 0.32	0.69 ± 0.06	2.33 ± 0.36
Cent. Sem.	0.74 ± 0.03	0.48 ± 0.05	1.13 ± 0.10	0.95 ± 0.04	1.40 ± 0.31
Cereb. ped.	0.74 ± 0.03	0.66 ± 0.03	1.35 ± 0.30	0.77 ± 0.06	1.78 ± 0.41
Cing. temp.	0.79 ± 0.08	0.51 ± 0.08	1.24 ± 0.12	0.87 ± 0.18	1.83 ± 0.29
Cingulate	0.70 ± 0.02	0.32 ± 0.05	1.04 ± 0.17	1.07 ± 0.06	0.89 ± 0.28
Corona Rad.	0.70 ± 0.02	0.59 ± 0.07	1.22 ± 0.16	0.72 ± 0.07	1.65 ± 0.37
Cortex	0.91 ± 0.21	0.25 ± 0.10	1.00 ± 0.15	0.87 ± 0.12	1.12 ± 0.27
Ext. caps.	0.73 ± 0.03	0.56 ± 0.05	0.91 ± 0.22	0.85 ± 0.04	1.16 ± 0.45
Fornix	1.84 ± 0.18	0.21 ± 0.05	0.65 ± 0.06	0.55 ± 0.04	0.72 ± 0.09
FWM	0.76 ± 0.03	0.37 ± 0.04	1.13 ± 0.11	0.97 ± 0.08	1.25 ± 0.16
Mesenc.	0.76 ± 0.09	0.43 ± 0.04	1.19 ± 0.14	0.93 ± 0.06	1.29 ± 0.26
Pallidium	0.78 ± 0.08	0.22 ± 0.05	1.07 ± 0.11	1.07 ± 0.08	1.05 ± 0.19
PLIC	0.70 ± 0.02	0.62 ± 0.04	1.08 ± 0.13	0.69 ± 0.06	1.36 ± 0.31
Pons	0.77 ± 0.07	0.38 ± 0.05	1.33 ± 0.11	1.00 ± 0.04	1.64 ± 0.18
Putamen	0.74 ± 0.03	0.17 ± 0.03	0.89 ± 0.10	0.97 ± 0.07	0.82 ± 0.14
PWM	0.75 ± 0.04	0.42 ± 0.06	1.15 ± 0.14	0.94 ± 0.06	1.29 ± 0.28
Thalamus	0.92 ± 0.15	0.27 ± 0.03	1.02 ± 0.11	0.88 ± 0.06	1.02 ± 0.11
TWM	0.70 ± 0.02	0.64 ± 0.04	1.10 ± 0.14	0.69 ± 0.05	1.10 ± 0.14

C. Ethics of voting

The institutional review board of the medical faculty at the Heinrich-Heine university in Dusseldorf approved all the protocols used during this thesis and written informed consent was obtained from all volunteers. The studies number were 3001, 3017 and 3826.

D. MR-Protocols

Table .8.: DTI acquisition protocol used in chapter 4.

SIEMENS MAGNETOM Trio Tim syngo MR B17			
Slices	50	***FoV Phase***	100 %
Distance factor	0 %	***Slice thickness***	2.0 mm
Position	Isocentre	***TR***	7700 ms
Orientation	Transversal	***TE***	112 ms
Phase encoding direction	A >>P	***Number of averages***	3
Rotation	0.00 Grad	***Diffusion mode***	MDDW
Phase -Oversampling	0	***Diffusion-weighting***	2
FoV Readout	256 mm	b***-value 1***	0 s/mm^2
Bandwidth	1502 Hx/Px	b***-value 2***	1000 s/mm^2
Echo distance	0.75 ms	***Diffusion directions***	20

Table .9.: DKI acquisition protocol used in chapter 7.

SIEMENS MAGNETOM Trio Tim syngo MR B17			
Slices	10	***TE***	98 ms
Distance factor	0%	***Number of averages***	2
Position	L15.6 A69.4 F47.8	***Diffusion mode***	MDDW
Orientation	C >T5.3 >S.1.3	***Diffusion-weighting***	7
Phase encoding direction	R >>L	b***-value 1***	0 s/mm^2
Rotation	0.00 Grad	b***-value 2***	250 s/mm^2
Phase -Oversampling	0%	b***-value 3***	500 s/mm^2
FoV Readout	400 mm	b***-value 4***	750 s/mm^2
Bandwidth	1532 Hx/Px	b***-value 5***	1000 s/mm^2
Echo distance	0.74 ms	b***-value 6***	1250 s/mm^2
FoV Phase	100%	b***-value 7***	1500 s/mm^2
Slice thickness	6.0 mm	***Diffusion directions***	30
TR	1500 ms		

Table .10.: DKI acquisition protocol used in chapter 7.

SIEMENS MAGNETOM Trio Tim syngo MR B17			
Slices	10	***TE***	98 ms
Distance factor	0%	***Number of averages***	2
Position	L15.6 A69.4 F47.8	***Diffusion mode***	MDDW
Orientation	C >T5.3 >S.1.3	***Diffusion-weighting***	7
Phase encoding direction	R >>L	b***-value 1***	0 s/mm^2
Rotation	0.00 Grad	b***-value 2***	250 s/mm^2
Phase -Oversampling	0%	b***-value 3***	500 s/mm^2
FoV Readout	400 mm	b***-value 4***	750 s/mm^2
Bandwidth	1532 Hx/Px	b***-value 5***	1000 s/mm^2
Echo distance	0.74 ms	b***-value 6***	1250 s/mm^2
FoV Phase	100%	b***-value 7***	1500 s/mm^2
Slice thickness	6.0 mm	***Diffusion directions***	20
TR	1500 ms		

Table .11.: DKI acquisition protocol used in chapter 6.

SIEMENS MAGNETOM Trio Tim syngo MR B17			
Slices	10	***Slice thickness***	5.0 mm
Distance factor	0%	***TR***	1500 ms
Position	L15.6 A69.4 F47.8	***TE***	90 ms
Orientation	C >T5.3 >S.1.3	***Number of averages***	4
Phase encoding direction	R >>L	***Diffusion mode***	MDDW
Rotation	0.00 Grad	***Diffusion-weighting***	3
Phase -Oversampling	0%	b***-value 1***	0 s/mm^2
FoV Readout	400 mm	b***-value 2***	300 s/mm^2
Bandwidth	2170 Hx/Px	b***-value 3***	600 s/mm^2
Echo distance	0.77 ms	***Diffusion directions***	
FoV Phase	100%		

Table .12.: DKI acquisition protocol used in chapter 6.

SIEMENS MAGNETOM Trio Tim syngo MR B17			
Slices	10	***Slice thickness***	5.0 mm
Distance factor	0%	***TR***	1500 ms
Position	L15.6 A69.4 F47.8	***TE***	90 ms
Orientation	C >T5.3 >S.1.3	***Number of averages***	8
Phase encoding direction	R >>L	***Diffusion mode***	MDDW
Rotation	0.00 Grad	***Diffusion-weighting***	3
Phase -Oversampling	0%	b***-value 1***	0 s/mm^2
FoV Readout	400 mm	b***-value 2***	300 s/mm^2
Bandwidth	2170 Hx/Px	b***-value 3***	600 s/mm^2
Echo distance	0.77 ms	***Diffusion directions***	
FoV Phase	100%		

Table .13.: DKI acquisition protocol used in chapter 5.

SIEMENS MAGNETOM Trio Tim syngo MR B17			
Slices	60	***Slice thickness***	2.5 mm
Distance factor	0%	***TR***	8100 ms
Position	Isocentre	***TE***	101 ms
Orientation	Transversal	***Number of averages***	2
Phase encoding direction	A >>P	***Diffusion mode***	MDDW
Rotation	0.00 Grad	***Diffusion-weighting***	3
Phase -Oversampling	0%	b***-value 1***	0 s/mm^2
FoV Readout	230 mm	b***-value 2***	1000 s/mm^2
Bandwidth	1552 Hx/Px	b***-value 3***	2000 s/mm^2
Echo distance	0.73 ms	***Diffusion directions***	30
FoV Phase	100%		

List of Figures

List of Tables

List of Abbreviations

1D	One dimensional
2D	Two dimensional
3D	Three dimensional
ADC	Apparent diffusion coefficient
ADF	Anisotropic diffusion filtering
K_{AX}	Axial Kurtosis
BG	Basal ganglia
C	Cortex
CC	Corpus callosum
CC	Cross correlation
c-χ	Centered distribution
CLLS	Constrained linear least squared
CNLS	Constrained nonlinear least squared
CNS	Central Nervous System
CSF	Cerebrospinal fluid
D_{AX}	Axial diffusivity
D_{RAD}	Radial diffusivity
DBM	Deformation-based morphometry
DKI	Diffusion Kurtosis Imaging
DTI	Diffusion Tensor Imaging
DT-MRI	Diffusion Tensor Magnetic Resonance imaging
DWI	Diffusion-Weighted Imaging
DW-MRI	Diffusion-Weighted Magnetic Resonance imaging
EPI	Echo Planar Imaging
FA	Fractional anisotropy
FWM	Frontal white matter
FOV	Field of view
GRAPPA	Generalised autocalibrating partially parallel acquisition
GM	Gray matter
HF	High frequency
ICBM	International Consortium for Brain Mapping
JaLMMSE	Joint information Linear Minimum Mean Square Error
K_{AX}	Axial kurtosis

K_{RAD}	Radial kurtosis
LM	Landmark
MD	Mean diffusivity
MI	Mutual information
MNI	Montreal Neurological Institute
MPG	Motion Probing Gradient
MPRAGE	magnetisation Prepared Rapid Acquisition Gradient Echo
MK	Mean kurtosis
MRI	Magnetic Resonance Imaging
MSQ	Mean squared intensity difference
nc-χ	Non-centered distribution
NMR	Nuclear Magnetic Resonance
ODE	ordinary differential equation
P	Pons
PDE	Partial differential equation
PDF	Probability density function
PGSE	Pulsed field gradient spin echo
PNS	Peripheral nervous system
RF	Radio frequency
ROI	Region-of-interest
SD	Standard deviation
SNR	Signal-to-noise ratio
SS-DWEPI	Single Shot Diffusion-Weighted Echo Planar Imaging
T	Tesla
TE	Echo time
TR	Repetition time
ULLS	Unconstrained linear least squared
WM	White matter

Bibliography

[1] Hartwig, Valentina ; Giovannetti, Giulio ; Vanello, Nicola ; Lombardi, Massimo ; Landini, Luigi ; Simi, Silvana: Biological Effects and Safety in Magnetic Resonance Imaging: A Review. 6 (2009), Nr. 6, S. 1778--1798

[2] Zhuo, Jiachen: *Diffusion kurtosis magnetic resonance imaging and its application to traumatic brain injury*, University of Maryland, dissertation, 2011

[3] Tuch, David S. ; Reese, Timothy G. ; Wiegell, Mette R. ; Makris, Nikos ; Belliveau, John W. ; Wedeen, Van J.: High angular resolution diffusion imaging reveals intravoxel white matter fiber heterogeneity. In: *Magnetic Resonance in Medicine: Official Journal of the Society of Magnetic Resonance in Medicine / Society of Magnetic Resonance in Medicine* 48 (2002), Oktober, Nr. 4, S. 577--582

[4] Wedeen, Van J. ; Hagmann, Patric ; Tseng, Wen-Yih I. ; Reese, Timothy G. ; Weisskoff, Robert M.: Mapping complex tissue architecture with diffusion spectrum magnetic resonance imaging. In: *Magnetic Resonance in Medicine: Official Journal of the Society of Magnetic Resonance in Medicine / Society of Magnetic Resonance in Medicine* 54 (2005), Dezember, Nr. 6, S. 1377--1386

[5] Kuo, Li-Wei ; Chen, Jyh-Horng ; Wedeen, Van J. ; Tseng, Wen-Yih I.: Optimization of diffusion spectrum imaging and q-ball imaging on clinical MRI system. In: *NeuroImage* 41 (2008), Mai, Nr. 1, S. 7--18

[6] Jensen, Jens H. ; Helpern, Joseph A. ; Ramani, Anita ; Lu, Hanzhang ; Kaczynski, Kyle: Diffusional kurtosis imaging: The quantification of non-gaussian water diffusion by means of magnetic resonance imaging. In: *Magnetic Resonance in Medicine* 53 (2005), Nr. 6, S. 1432--1440

[7] Le Bihan, D ; Breton, E ; Lallemand, D ; Grenier, P ; Cabanis, E ; Laval-Jeantet, M: MR imaging of intravoxel incoherent motions: application to diffusion and perfusion in neurologic disorders. In: *Radiology* 161 (1986), Nr. 2, S. 401--407

[8] Yablonskiy, Dmitriy A. ; Bretthorst, G L. ; Ackerman, Joseph J H.: Statistical model for diffusion attenuated MR signal. In: *Magnetic resonance in medicine: official journal of the Society of Magnetic Resonance in Medicine / Society of Magnetic Resonance in Medicine* 50 (2003), Oktober, Nr. 4, S. 664--669

[9] Jensen, Jens H. ; Helpern, Joseph A.: MRI quantification of non-Gaussian water diffusion by kurtosis analysis. In: *NMR in Biomedicine* 23 (2010), Nr. 7, S. 698--710

[10] Falangola, Maria F. ; Jensen, Jens H. ; Babb, James S. ; Hu, Caixia ; Castellanos, Francisco X. ; Di Martino, Adriana ; Ferris, Steven H. ; Helpern, Joseph A.: Age-Related Non-Gaussian Diffusion Patterns in the Prefrontal Brain. In: *Journal of magnetic resonance imaging : JMRI* 28 (2008), Dezember, Nr. 6, S. 1345--1350

[11] Raab, Peter ; Hattingen, Elke ; Franz, Kea ; Zanella, Friedhelm E. ; Lanfermann, Heinrich: Cerebral Gliomas: Diffusional Kurtosis Imaging Analysis of Microstructural Differences1. In: *Radiology* 254 (2010), Januar, Nr. 3, S. 876--881

[12] Cauter, Sofie V. ; Veraart, Jelle ; Sijbers, Jan ; Peeters, Ronald R. ; Himmelreich, Uwe ; Keyzer, Frederik D. ; Gool, Stefaan W. V. ; Calenbergh, Frank V. ; Vleeschouwer, Steven D. ; Hecke, Wim V. ; Sunaert, Stefan: Gliomas: Diffusion Kurtosis MR Imaging in Grading. In: *Radiology* 263 (2012), Januar, Nr. 2, S. 492--501

[13] Gray, Henry: *Anatomy of the Human Body*. Lea & Febiger, 1918

[14] Descoteaux, Maxime: *IRM de Diffusion à Haute Résolution Angulaire: Estimation Locale, Segmentation et Suivi de Fibres*, University of Nice-Sophia Antipolis, dissertation, 2008. https://tel.archives-ouvertes.fr/tel-00457458/document

[15] Valenzuela, C. F. ; Puglia, Michael P. ; Zucca, Stefano: Focus On: Neurotransmitter Systems. In: *Alcohol Research & Health* 34 (2011), Nr. 1, S. 106--120

[16] Hines, Tonya: *Anatomy of the brain*. Version: 2013. http://www.mayfieldclinic.com/PE-AnatBrain.htm, Abruf: 30.12.2015

[17] CNX, OpenStax: *OpenStax Anatomy and Physiology*. Version: 2013. http://cnx.org/contents/14fb4ad7-39a1-4eee-ab6e-3ef2482e3e22@6.27, Abruf: 31.12.2015

[18] Bhise, Dr S. B.: *Anatomy Physiology And Health Education*. Pragati Books Pvt. Ltd., 2008. -- ISBN 978--81--85790--43--5

[19] Patestas, Maria ; Gartner, Leslie P.: *A Textbook of Neuroanatomy*. Wiley, 2006

[20] Johansen-Berg, Heidi ; Behrens, Timothy E. J.: *Diffusion MRI: From Quantitative Measurement to In vivo Neuroanatomy*. Academic Press, 2013. -- ISBN 978--0--12--405509--4

[21] Weishaupt, Dominik ; Köchli, Victor D. ; Marincek, Borut: *Wie funktioniert MRI?: Eine Einführung in Physik und Funktionsweise der Magnetresonanzbildgebung*. Springer Science & Business Media, 2009

[22] Laun, F.B. ; Fritzsche, K.H. ; Kuder, T.A. ; Stieltjes, B.: Einführung in die Grundlagen und Techniken der Diffusionsbildgebung. 51 (2011), Nr. 3, 170--179. http://dx.doi.org/10.1007/s00117-010-2057-y. -- DOI 10.1007/s00117--010--2057--y. -- ISSN 0033--832X, 1432--2102

[23] Moseley, M. E. ; Kucharczyk, J. ; Mintorovitch, J. ; Cohen, Y. ; Kurhanewicz, J. ; Derugin, N. ; Asgari, H. ; Norman, D.: Diffusion-weighted MR imaging of acute stroke: correlation with T2-weighted and magnetic susceptibility-enhanced MR imaging in cats. In: *AJNR. American journal of neuroradiology* 11 (1990), Mai, Nr. 3, S. 423--429

[24] Rovaris, M. ; Gass, A. ; Bammer, R. ; Hickman, S. J. ; Ciccarelli, O. ; Miller, D. H. ; Filippi, M.: Diffusion MRI in multiple sclerosis. In: *Neurology* 65 (2005), November, Nr. 10, S. 1526--1532

[25] Maier, Stephan E. ; Sun, Yanping ; Mulkern, Robert V.: Diffusion Imaging of Brain Tumors. In: *NMR in biomedicine* 23 (2010), August, Nr. 7, S. 849--864

[26] Müller, M. F. ; Prasad, P. V. ; Bimmler, D. ; Kaiser, A. ; Edelman, R. R.: Functional imaging of the kidney by means of measurement of the apparent diffusion coefficient. In: *Radiology* 193 (1994), Januar, Nr. 3, S. 711--715

[27] Hagmann, Patric ; Jonasson, Lisa ; Maeder, Philippe ; Thiran, Jean-Philippe ; Weeden, Van J. ; Meuli, Reto: Understanding Diffusion MR Imaging Techniques: From Scalar Diffusion-weighted Imaging to Diffusion Tensor Imaging and Beyond. In: *Radiographics* 26 (2006), S. 205--223

[28] Mori, S ; Barker, B: Diffusion Magnetic Resonance Imaging: Its Principle and Applications. The Anatomical Record 2. In: *Anatomical Record* 257 (1999), S. 102--109

[29] Derek, K. J.: *Diffusion MRI: Theory, Methods, and Applications - PhD*. Oxford University Press, 2010. -- ISBN 978--0--19--970870--3

[30] Fick, Adolf E.: On liquid diffusion. In: *Poggendorff's Annalen der Physik und Chemie* 94 (1855), S. 59--86

[31] Brown, Robert: A brief account of microscopical observations made in the months of June, July and August 1827, on the particles contained in the pollen of plants; and on the general existence of active molecules in organic and inorganic bodies. In: *Philosophical Magazine Series* 2 4 (1828), S. 161--173

[32] Einstein, Albert: Investigations on the theory of the brownian movement. In: *Dover Publications, Inc.* (1956)

[33] Stejskal, E. O. ; Tanner, J. E.: Spin Diffusion Measurements: Spin Echoes in the Presence of a Time-Dependent Field Gradient. In: *The Journal of Chemical Physics* 42 (1965), Nr. 1, S. 288

[34] Uluğ, A. M. ; Beauchamp, N. ; Bryan, R. N. ; Zijl, P. C.: Absolute quantitation of diffusion constants in human stroke. In: *Stroke; a Journal of Cerebral Circulation* 28 (1997), März, Nr. 3, S. 483--490

[35] Basser, P.J. ; Mattiello, J. ; Le Bihan, D: MR diffusion tensor spectroscopy and imaging. In: *Biophysical Journal* 66 (1994), Januar, Nr. 1, S. 259--267

[36] Melhem, Elias R. ; Mori, Susumu ; Mukundan, Govind ; Kraut, Michael A. ; Pomper, Martin G. ; Zijl, Peter C. M.: Diffusion Tensor MR Imaging of the Brain and White Matter Tractography. In: *American Journal of Roentgenology* 178 (2002), Januar, Nr. 1, S. 3--16

[37] Moseley, Michael: Diffusion tensor imaging and aging - a review. In: *NMR in biomedicine* 15 (2002), Dezember, Nr. 7-8, S. 553--560

[38] Mori, Susumu ; Zijl, Peter C. M.: Fiber tracking: principles and strategies - a technical review. In: *NMR in biomedicine* 15 (2002), Dezember, Nr. 7-8, S. 468--480

[39] Maier, Stephan E. ; Shenton, Martha E. ; Jolesz, Ferenc A.: Diffusion MRI explores new indications. In: *Advanced MR* (2001)

[40] De Santis, Silvia ; Gabrielli, Andrea ; Palombo, Marco ; Maraviglia, Bruno ; Capuani, Silvia: Non-Gaussian diffusion imaging: a brief practical review. In: *Magnetic Resonance Imaging* 29 (2011), Dezember, Nr. 10, S. 1410--1416

[41] Assaf, Y. ; Cohen, Y.: Assignment of the water slow-diffusing component in the central nervous system using q-space diffusion MRS: implications for fiber tract imaging. In: *Magnetic Resonance in Medicine: Official Journal of the Society of Magnetic Resonance in Medicine / Society of Magnetic Resonance in Medicine* 43 (2000), Februar, Nr. 2, S. 191--199

[42] Clark, Chris A. ; Hedehus, Maj ; Moseley, Michael E.: In vivo mapping of the fast and slow diffusion tensors in human brain. In: *Magnetic resonance in medicine: official journal of the Society of Magnetic Resonance in Medicine / Society of Magnetic Resonance in Medicine* 47 (2002), Nr. 4, S. 623--628

[43] Minati, Ludovico ; Aquino, Domenico ; Rampoldi, Stefano ; Papa, Sergio ; Grisoli, Marina ; Bruzzone, Maria G. ; Maccagnano, Elio: Biexponential and diffusional kurtosis imaging, and generalised diffusion-tensor imaging (GDTI) with rank-4 tensors: a study in a group of healthy subjects. In: *Magnetic Resonance Materials in Physics, Biology and Medicine* 20 (2007), Dezember, Nr. 5-6, S. 241--253

[44] Milne, Michelle L. ; Conradi, Mark S.: Multi-exponential signal decay from diffusion in a single compartment. In: *Journal of magnetic resonance (San Diego, Calif. : 1997)* 197 (2009), März, Nr. 1, S. 87--90

[45] Alexander, D. C. ; Barker, G. J. ; Arridge, S. R.: Detection and modeling of non-Gaussian apparent diffusion coefficient profiles in human brain data. In: *Magnetic Resonance in Medicine* 48 (2002), August, Nr. 2, S. 331--340

[46] Van, Anh T. ; Granziera, Cristina ; Bammer, Roland: An Introduction to Model-Independent Diffusion MRI. In: *Topics in magnetic resonance imaging : TMRI* 21 (2010), Dezember, Nr. 6, S. 339--354

[47] Basser, Peter J.: Relationships between diffusion tensor and q-space MRI†. In: *Magnetic Resonance in Medicine* 47 (2002), Februar, Nr. 2, S. 392--397

[48] Wedeen, V. J. ; Wang, R. P. ; Schmahmann, J. D. ; Benner, T. ; Tseng, W. Y. I. ; Dai, G. ; Pandya, D. N. ; Hagmann, P. ; D'Arceuil, H. ; Crespigny, A. J.: Diffusion spectrum magnetic resonance imaging (DSI) tractography of crossing fibers. In: *NeuroImage* 41 (2008), Juli, Nr. 4, S. 1267--1277

[49] Bennett, Kevin M. ; Schmainda, Kathleen M. ; Bennett, Raoqiong T. ; Rowe, Daniel B. ; Lu, Hanbing ; Hyde, James S.: Characterization of continuously distributed cortical water diffusion rates with a stretched-exponential model. In: *Magnetic resonance in medicine: official journal of the Society of Magnetic Resonance in Medicine / Society of Magnetic Resonance in Medicine* 50 (2003), Oktober, Nr. 4, S. 727--734

[50] Cheung, Matthew M. ; Hui, Edward S. ; Chan, Kevin C. ; Helpern, Joseph A. ; Qi, Liqun ; Wu, Ed X.: Does diffusion kurtosis imaging lead to better neural tissue characterization? A rodent brain maturation study. In: *NeuroImage* 45 (2009), April, Nr. 2, S. 386--392

[51] Tabesh, Ali ; Jensen, Jens H. ; Ardekani, Babak A. ; Helpern, Joseph A.: Estimation of tensors and tensor-derived measures in diffusional kurtosis imaging. In: *Magnetic Resonance in Medicine* 65 (2011), Nr. 3, S. 823--836

[52] Hui, Edward S. ; Cheung, Matthew M. ; Qi, Liqun ; Wu, Ed X.: Towards better MR characterization of neural tissues using directional diffusion kurtosis analysis. In: *NeuroImage* 42 (2008), August, Nr. 1, S. 122--134

[53] Basser, Peter J. ; Jones, Derek K.: Diffusion-tensor MRI: theory, experimental design and data analysis – a technical review. In: *NMR in Biomedicine* 15 (2002), November, Nr. 7-8, S. 456--467

[54] Hoa, Denis ; SAS, IMAIOS (Hrsg.): *Signal-to-noise ratio*. Version: 2015. https://www.imaios.com/de/e-Kurs/e-MRI/Image-quality-and-artifacts/Signal-to-noise-ratio, Abruf: 30.12.2015

[55] Bihan, Denis L.: Apparent Diffusion Coefficient and Beyond: What Diffusion MR Imaging Can Tell Us about Tissue Structure. 268 (2013), Nr. 2, S. 318--322

[56] Chuck, Natalie C. ; Steidle, Gunther ; Blume, Iris ; Fischer, Michael A. ; Nanz, Daniel ; Boss, Andreas: Diffusion Tensor Imaging of the Kidneys: Influence of b-Value and Number of Encoding Directions on Image Quality and Diffusion Tensor Parameters. In: *Journal of Clinical Imaging Science* 3 (2013), November

[57] Gurses, Bengi ; Kilickesmez, Ozgur ; Tasdelen, Neslihan ; Firat, Zeynep ; Gurmen, Nevzat: Diffusion tensor imaging of the kidney at 3 tesla: normative values and repeatability of measurements in healthy volunteers. In: *Diagnostic and Interventional Radiology* (2010)

[58] Le Bihan, D ; Mangin, Jean-Francois ; Poupon, Cyril ; Clark, Chris A. ; Pappata, Sabina ; Molko, Nicolas ; Chabriat, Hughes: Diffusion Tensor Imaging: Concepts and Applications. In: *journal of magnetic resonance imaging* (2001)

[59] Bozzali, M ; Falini, A ; Franceschi, M ; Cercignani, M ; Zuffi, M ; Scotti, G ; Comi, G ; Filippi, M: White matter damage in Alzheimer's disease assessed in vivo using diffusion tensor magnetic resonance imaging. In: *Journal of Neurology, Neurosurgery, and Psychiatry* 72 (2002), Juni, Nr. 6, S. 742--746

[60] Karagulle Kendi, A T. ; Lehericy, S ; Luciana, M ; Ugurbil, K ; Tuite, P: Altered diffusion in the frontal lobe in Parkinson disease. In: *AJNR. American journal of neuroradiology* 29 (2008), März, Nr. 3, S. 501--505

[61] Ries, Mario ; Jones, Richard A. ; Basseau, Fabrice ; Moonen, Chrit T. ; Grenier, Nicolas: Diffusion tensor MRI of the human kidney. In: *Journal of Magnetic Resonance Imaging* 14 (2001), Nr. 1, S. 42--49

[62] Nikken, J. J. ; Krestin, G. P.: MRI of the kidney--state of the art. In: *European Radiology* 17 (2007), November, Nr. 11, S. 2780--2793

[63] Kataoka, Masako ; Kido, Aki ; Yamamoto, Akira ; Nakamoto, Yuji ; Koyama, Takashi ; Isoda, Hiroyoshi ; Maetani, Yoji ; Umeoka, Shigeaki ; Tamai, Ken ; Saga, Tsuneo ; Morisawa, Nobuko ; Mori, Susumu ; Togashi, Kaori: Diffusion tensor imaging of kidneys with

respiratory triggering: Optimization of parameters to demonstrate anisotropic structures on fraction anisotropy maps. In: *Journal of Magnetic Resonance Imaging* 29 (2009), Nr. 3, S. 736--744

[64] Hans-Jörg, Wittsack ; Lanzman, Rotem S. ; Quentin, Michael ; Kuhlemann, Julia ; Klasen, Janina ; Pentang, Gael ; Riegger, Caroline ; Antoch, Gerald ; Blondin, Dirk: Temporally Resolved Electrocardiogram-Triggered Diffusion-Weighted Imaging of the Human Kidney. In: *Investigative Radiology* 47 (2012), April, Nr. 4, S. 226--230

[65] Thoeny, Harriet C. ; Keyzer, Frederik D. ; Oyen, Raymond H. ; Peeters, Ronald R.: Diffusion-weighted MR Imaging of Kidneys in Healthy Volunteers and Patients with Parenchymal Diseases: Initial Experience1. In: *Radiology* 235 (2005), Januar, Nr. 3, S. 911--917

[66] Setsompop, Kawin ; Gagoski, Borjan A. ; Polimeni, Jonathan R. ; Witzel, Thomas ; Wedeen, Van J. ; Wald, Lawrence L.: Blipped-Controlled Aliasing in Parallel Imaging (blipped-CAIPI) for simultaneous multi-slice EPI with reduced g-factor penalty. In: *Magnetic Resonance in Medicine* 67 (2012), Mai, Nr. 5, S. 1210--1224

[67] Pipe, J. G.: Motion correction with PROPELLER MRI: application to head motion and free-breathing cardiac imaging. In: *Magnetic Resonance in Medicine: Official Journal of the Society of Magnetic Resonance in Medicine / Society of Magnetic Resonance in Medicine* 42 (1999), November, Nr. 5, S. 963--969

[68] Papadakis, N G. ; Martin, K M. ; Pickard, J D. ; Hall, L D. ; Carpenter, T A. ; Huang, C L.: Gradient preemphasis calibration in diffusion-weighted echo-planar imaging. In: *Magnetic resonance in medicine: official journal of the Society of Magnetic Resonance in Medicine / Society of Magnetic Resonance in Medicine* 44 (2000), Oktober, Nr. 4, S. 616--624

[69] Prasad, P V. ; Nalcioglu, O: A modified pulse sequence for in vivo diffusion imaging with reduced motion artifacts. In: *Magnetic resonance in medicine: official journal of the Society of Magnetic Resonance in Medicine / Society of Magnetic Resonance in Medicine* 18 (1991), März, Nr. 1, S. 116--131

[70] Rohde, G K. ; Barnett, A S. ; Basser, P J. ; Marenco, S ; Pierpaoli, C: Comprehensive approach for correction of motion and distortion in diffusion-weighted MRI. In: *Magnetic resonance in medicine: official journal of the Society of Magnetic Resonance in Medicine / Society of Magnetic Resonance in Medicine* 51 (2004), Januar, Nr. 1, S. 103--114

[71] Holdsworth, Samantha J. ; Aksoy, Murat ; Newbould, Rexford D. ; Yeom, Kristen ; Van, Anh T. ; Ooi, Melvyn B. ; Barnes, Patrick D. ; Bammer, Roland ; Skare, Stefan: Diffusion tensor imaging (DTI) with retrospective motion correction for large-scale pediatric imaging. 36 (2012), Nr. 4, 961--971. http://dx.doi.org/10.1002/jmri.23710. -- DOI 10.1002/jmri.23710. -- ISSN 1522--2586

[72] Crum, W. R. ; Hartkens, T. ; Hill, D. L. G.: Non-rigid image registration: theory and practice. In: *The British Journal of Radiology* 77 Spec No 2 (2004), S. S140--153

[73] Avants, Brian B. ; Tustison, Nicholas J. ; Song, Gang ; Cook, Philip A. ; Klein, Arno ; Gee, James C.: A reproducible evaluation of ANTs similarity metric performance in brain image registration. In: *NeuroImage* 54 (2011), Februar, Nr. 3, S. 2033--2044

[74] HAJNAL, Joseph V. ; HILL, Derek L. G.: *Medical Image Registration*. CRC Press, 2001. -- ISBN 978--1--4200--4247--4

[75] DAI, Liming ; JAZAR, Reza N.: *Nonlinear Approaches in Engineering Applications: Applied Mechanics, Vibration Control, and Numerical Analysis*. Springer, 2014. -- ISBN 978--3--319--09462--5

[76] RUECKERT, D. ; ALJABAR, P.: Nonrigid Registration of Medical Images: Theory, Methods, and Applications [Applications Corner]. In: *IEEE Signal Processing Magazine* 27 (2010), Juli, Nr. 4, S. 113--119

[77] STUDHOLME, C. ; HILL, D. L. G. ; HAWKES, D. J.: An overlap invariant entropy measure of 3D medical image alignment. In: *Pattern Recognition* 32 (1999), Januar, Nr. 1, S. 71--86

[78] NOCEDAL, Jorge ; WRIGHT, Stephen: *Numerical Optimization*. Springer New York, 2006 (Springer Series in Operations Research and Financial Engineering). -- ISBN 978--0--387--30303--1

[79] DAI, Yu-Hong: A Family of Hybrid Conjugate Gradient Methods for Unconstrained Optimization. In: *Math. Comput.* 72 (2003), Juli, Nr. 243, S. 1317--1328

[80] DENNIS, Jr. J. ; MORÉ, J.: Quasi-Newton Methods, Motivation and Theory. In: *SIAM Review* 19 (1977), Januar, Nr. 1, S. 46--89

[81] HANSEN, Nikolaus ; OSTERMEIER, Andreas: Completely Derandomized Self-Adaptation in Evolution Strategies. In: *Evol. Comput.* 9 (2001), Juni, Nr. 2, S. 159--195

[82] HASELGROVE, J C. ; MOORE, J R.: Correction for distortion of echo-planar images used to calculate the apparent diffusion coefficient. In: *Magnetic resonance in medicine: official journal of the Society of Magnetic Resonance in Medicine / Society of Magnetic Resonance in Medicine* 36 (1996), Dezember, Nr. 6, S. 960--964

[83] ASHBURNER, John ; FRISTON, Karl J.: Voxel-Based Morphometry—The Methods. In: *NeuroImage* 11 (2000), Juni, Nr. 6, S. 805--821

[84] APICELLA, Anthony ; KIPPENHAN, J. S. ; NAGEL, Joachim H.: Fast Multi-Modality Image Matching. In: *Medical Imaging III: Image Processing, SPIE Vol. 1092* Bd. 1092, 1989, S. 252--263

[85] BASTIN, Mark E.: Correction of eddy current-induced artefacts in diffusion tensor imaging using iterative cross-correlation. In: *Magnetic Resonance Imaging* 17 (1999), September, Nr. 7, S. 1011--1024

[86] MATTES, David ; HAYNOR, David R. ; VESSELLE, Hubert ; LEWELLYN, Thomas K. ; EUBANK, William: Nonrigid multimodality image registration. In: *Medical Imaging 2001: Image Processing* Bd. 4322, 2001, S. 1609

[87] VIOLA, Paul ; WELLS, William M. W.: Alignment by Maximization of Mutual Information. In: *International Journal of Computer Vision* 24 (1997), September, Nr. 2, S. 137--154

[88] BAMMER, R. ; AUER, M.: Correction of eddy-current induced image warping in diffusion-weighted single-shot EPI using constrained nonrigid mutual information image registration. In: *Proceedings of the 9th Annual Meeting of ISMRM, Glasgow, Scotland, 2001*, 2001, S. 508

[89] Wittsack, H. J. ; Ritzl, A. ; Mödder, U.: User friendly analysis of MR investigations of the cerebral perfusion: Windows(R)-based image processing. In: *RöFo: Fortschritte Auf Dem Gebiete Der Röntgenstrahlen Und Der Nuklearmedizin* 174 (2002), Juni, Nr. 6, S. 742--746

[90] Ibanez, L. ; Schroeder, W. ; Ng, L. ; Cates, J. ; Consortium the Insight s.: *The ITK Software Guide - Second Edition*. 2005

[91] Tremblay, Marleine ; Tam, Fred ; Graham, Simon J.: Retrospective coregistration of functional magnetic resonance imaging data using external monitoring. In: *Magnetic Resonance in Medicine: Official Journal of the Society of Magnetic Resonance in Medicine / Society of Magnetic Resonance in Medicine* 53 (2005), Januar, Nr. 1, S. 141--149

[92] Friston, K. J. ; Holmes, A. P. ; Worsley, K. J. ; Poline, J.-P. ; Frith, C. D. ; Frackowiak, R. S. J.: Statistical parametric maps in functional imaging: A general linear approach. In: *Human Brain Mapping* 2 (1994), Januar, Nr. 4, S. 189--210

[93] Wang, Ruopeng ; Van J., Weeden: Diffusion Toolkit: A Software Package for Diffusion Imaging Data Processing and Tractography. In: *ISMRM abstract Proceedings International Society of Magnetic Resonance in Medicine* (2007), S. 3720

[94] Borius, Pierre-Yves ; Roux, Franck-Emmanuel ; Valton, Luc ; Sol, Jean-Christophe ; Lotterie, Jean-Albert ; Berry, Isabelle: Can DTI fiber tracking of the optic radiations predict visual deficit after surgery? In: *Clinical Neurology and Neurosurgery* 122 (2014), Juli, S. 87--91

[95] Yasmin, Hasina ; Kabasawa, Hiroyuki ; Aoki, Shigeki ; Abe, Osamu ; Masutani, Yoshitaka ; Hayashi, Naoto ; Ohtomo, Kuni: Motion-robust diffusion tensor acquisition at routine 3T magnetic resonance imaging. In: *Japanese journal of radiology* 28 (2010), Januar, Nr. 1, S. 27--33

[96] Klooster, R. van '. ; Staring, M. ; Klein, S. ; Kwee, R. M. ; Kooi, M. E. ; Reiber, J. H. C. ; Lelieveldt, B. P. F. ; Geest, R. J. d.: Automated registration of multispectral MR vessel wall images of the carotid artery. In: *Medical Physics* 40 (2013), Dezember, Nr. 12, S. 121904

[97] Tang, Yuchun ; Hojatkashani, Cornelius ; Dinov, Ivo D. ; Sun, Bo ; Fan, Lingzhong ; Lin, Xiangtao ; Qi, Hengtao ; Hua, Xue ; Liu, Shuwei ; Toga, Arthur W.: The construction of a Chinese MRI brain atlas: a morphometric comparison study between Chinese and Caucasian cohorts. In: *NeuroImage* 51 (2010), Mai, Nr. 1, S. 33--41

[98] Pentang, Gael ; Lanzman, Rotem S. ; Heusch, Philpp ; Müller-Lutz, Anja ; Blondin, Dirk ; Antoch, Gerald ; Wittsack, Hans-Jörg: Diffusion kurtosis imaging of the human kidney: A feasibility study. In: *Magnetic Resonance Imaging* 32 (2014), Nr. 5, S. 413--20

[99] Aja-Fernandez, Santiago ; Niethammer, Marc ; Kubicki, Marek ; Shenton, Martha E. ; Westin, Carl-Fredrik: Restoration of DWI Data Using a Rician LMMSE Estimator. In: *IEEE transactions on medical imaging* 27 (2008), Oktober, Nr. 10, S. 1389--1403

[100] Coulon, O. ; Alexander, D. C. ; Arridge, S.: Diffusion tensor magnetic resonance image regularization. In: *Medical Image Analysis* 8 (2004), Nr. 1

[101] Castaño-Moraga, C. A. ; Lenglet, C. ; Deriche, R. ; Ruiz-Alzola, J.: A Riemannian approach to anisotropic filtering of tensor fields. In: *Signal Processing* 87 (2007), Nr. 2

[102] Clarke, R.A ; Scifo, P. ; Rizzo, G. ; Dell'Acqua, F. ; Scotti, G. ; Fazio, F.: Noise Correction on Rician Distributed Data for Fibre Orientation Estimators. In: *IEEE Transactions on Medical Imaging* 27 (2008), September, Nr. 9, S. 1242--1251. http://dx.doi.org/10.1109/TMI.2008.920615. -- DOI 10.1109/TMI.2008.920615. -- ISSN 0278--0062

[103] Fillard, Pierre ; Pennec, Xavier ; Arsigny, Vincent ; Ayache, Nicholas: Clinical DT-MRI estimation, smoothing, and fiber tracking with log-Euclidean metrics. In: *IEEE transactions on medical imaging* 26 (2007), November, Nr. 11, S. 1472--1482. http://dx.doi.org/10.1109/TMI.2007.899173. -- DOI 10.1109/TMI.2007.899173. -- ISSN 0278--0062

[104] Perona, P. ; Malik, J.: Scale-space and edge detection using anisotropic diffusion. In: *IEEE Transactions on Pattern Analysis and Machine Intelligence* 12 (1990), Juli, Nr. 7, S. 629--639

[105] Tristán-Vega, Antonio ; Aja-Fernández, Santiago: DWI filtering using joint information for DTI and HARDI. In: *Medical image analysis* 14 (2010), April, Nr. 2, S. 205--218

[106] Gerig, G. ; Kubler, O. ; Kikinis, R. ; Jolesz, F.A.: Nonlinear anisotropic filtering of MRI data. In: *IEEE Transactions on Medical Imaging* 11 (1992), Juni, Nr. 2, S. 221--232

[107] Tristan-Vega, A. ; Brion, V. ; Vegas-Sanchez-Ferrero, G. ; Aja-Fernandez, S.: Merging squared-magnitude approaches to DWI denoising: An adaptive Wiener filter tuned to the anatomical contents of the image. In: *2013 35th Annual International Conference of the IEEE Engineering in Medicine and Biology Society (EMBC)*, 2013, S. 507--510

[108] Ferrari, Ricardo J.: Off-line determination of the optimal number of iterations of the robust anisotropic diffusion filter applied to denoising of brain MR images. In: *Medical & biological engineering & computing* 51 (2013), Februar, Nr. 1-2, S. 71--88

[109] Wilkins, Bryce ; Lee, Namgyun ; Gajawelli, Niharika ; Law, Meng ; Leporé, Natasha: Simulated DW-MRI Brain Data Sets for Quantitative Evaluation of Estimated Fiber Orientations. In: *22 nd Annual Meeting of the International Society for Magnetic Resonance in Medicine*, 2014, S. 2591

[110] Wang, Zhou ; Bovik, A.C. ; Sheikh, H.R. ; Simoncelli, E.P.: Image quality assessment: from error visibility to structural similarity. In: *IEEE Transactions on Image Processing* 13 (2004), April, Nr. 4, S. 600--612

[111] Jiang, Yi ; Johnson, G. A.: Microscopic diffusion tensor atlas of the mouse brain. In: *NeuroImage* 56 (2011), Juni, Nr. 3, S. 1235--1243

[112] Talairach, J ; Tournoux, P: Co-Planar Stereotaxic Atlas of the Human Brain. 3-Dimensional Proportional System: An Approach to Cerebral Imaging. In: *Thieme Medical* (1988)

[113] Lancaster, Jack L. ; Woldorff, Marty G. ; Parsons, Lawrence M. ; Liotti, Mario ; Freitas, Catarina S. ; Rainey, Lacy ; Kochunov, Peter V. ; Nickerson, Dan ; Mikiten, Shawn A. ; Fox, Peter T.: Automated Talairach Atlas labels for functional brain mapping. In: *Human Brain Mapping* 10 (2000), Nr. 3, S. 120--131

[114] Evans, A. C. ; Collins, D. L. ; Milner, B.: An MRI-based stereotactic atlas from 250 young normal subjects. In: *Society for Neuroscience* (1992), S. 408

[115] Collins, D. L. ; Neeling, Peter ; Peters, Terrence M. ; Evans, Alan C.: *Automatic 3D Intersubject Registration of MR Volumetric Data... : Journal of Computer Assisted Tomography*. 1994

[116] Mazziotta, John C. ; Toga, Arthur W. ; Evans, Alan ; Fox, Peter ; Lancaster, Jack: A Probabilistic Atlas of the Human Brain: Theory and Rationale for Its Development: The International Consortium for Brain Mapping (ICBM). In: *NeuroImage* 2 (1995), Juni, Nr. 2, Part A, S. 89--101

[117] Toga, Arthur W. ; Thompson, Paul M. ; Mori, Susumu ; Amunts, Katrin ; Zilles, Karl: Towards multimodal atlases of the human brain. In: *Nature reviews. Neuroscience* 7 (2006), Dezember, Nr. 12, S. 952--966

[118] Lätt, Jimmy ; Nilsson, Markus ; Wirestam, Ronnie ; Ståhlberg, Freddy ; Karlsson, Nils ; Johansson, Mikael ; Sundgren, Pia C. ; Westen, Danielle van: Regional values of diffusional kurtosis estimates in the healthy brain. In: *Journal of Magnetic Resonance Imaging* 37 (2013), Nr. 3, S. 610--618

[119] Helenius, Johanna ; Soinne, Lauri ; Perkiö, Jussi ; Salonen, Oili ; Kangasmäki, Aki ; Kaste, Markku ; Carano, Richard A. D. ; Aronen, Hannu J. ; Tatlisumak, Turgut: Diffusion-weighted MR imaging in normal human brains in various age groups. In: *AJNR. American journal of neuroradiology* 23 (2002), Februar, Nr. 2, S. 194--199

[120] Pentang, Gael ; Mathys, Christian ; Turowski, Bernd ; Antoch, Gerald ; Wittsack, Hans-Jörg: Evaluation of mutual information based motion correction techniques in DTI. In: *European Society of Magnetic Resonance in Medicine and Biology* In Proceeding of the 28th scientific meeting (2011)

[121] Klein, Arno ; Andersson, Jesper ; Ardekani, Babak A. ; Ashburner, John ; Avants, Brian ; Chiang, Ming-Chang ; Christensen, Gary E. ; Collins, D. L. ; Gee, James ; Hellier, Pierre ; Song, Joo H. ; Jenkinson, Mark ; Lepage, Claude ; Rueckert, Daniel ; Thompson, Paul ; Vercauteren, Tom ; Woods, Roger P. ; Mann, J. J. ; Parsey, Ramin V.: Evaluation of 14 nonlinear deformation algorithms applied to human brain MRI registration. In: *NeuroImage* 46 (2009), Juli, Nr. 3, S. 786--802

[122] Peng, Huiling ; Orlichenko, Anton ; Dawe, Robert J. ; Agam, Gady ; Zhang, Shengwei ; Arfanakis, Konstantinos: Development of a Human Brain Diffusion Tensor Template. In: *NeuroImage* 46 (2009), Juli, Nr. 4, S. 967--980

[123] Mori, Susumu ; Oishi, Kenichi ; Jiang, Hangyi ; Jiang, Li ; Li, Xin ; Akhter, Kazi ; Hua, Kegang ; Faria, Andreia V. ; Mahmood, Asif ; Woods, Roger ; Toga, Arthur W. ; Pike, G. B. ; Neto, Pedro R. ; Evans, Alan ; Zhang, Jiangyang ; Huang, Hao ; Miller, Michael I. ; Zijl, Peter van ; Mazziotta, John: Stereotaxic white matter atlas based on diffusion tensor imaging in an ICBM template. In: *NeuroImage* 40 (2008), April, Nr. 2, S. 570--582

[124] Wu, Yu-Chien ; Field, Aaron S. ; Whalen, Paul J. ; Alexander, Andrew L.: Age and Gender Related Changes in the Normal Human Brain using Hybrid Diffusion Imaging (HYDI). In: *NeuroImage* 54 (2011), Februar, Nr. 3, S. 1840--1853

[125] Poot, D. H J. ; Dekker, A.J. den ; Achten, E. ; Verhoye, M. ; Sijbers, J.: Optimal Experimental Design for Diffusion Kurtosis Imaging. In: *IEEE Transactions on Medical Imaging* 29 (2010), Nr. 3, S. 819--829

[126] Sullivan, Edith V. ; Pfefferbaum, Adolf: Diffusion tensor imaging and aging. In: *Neuroscience and biobehavioral reviews* 30 (2006), Nr. 6, S. 749--761

[127] Ardekani, Siamak ; Sinha, Usha: Statistical representation of mean diffusivity and fractional anisotropy brain maps of normal subjects. In: *Journal of magnetic resonance imaging: JMRI* 24 (2006), Dezember, Nr. 6, S. 1243--1251

[128] Van Hecke, Wim ; Sijbers, Jan ; D'Agostino, Emiliano ; Maes, Frederik ; De Backer, Steve ; Vandervliet, Evert ; Parizel, Paul M. ; Leemans, Alexander: On the construction of an inter-subject diffusion tensor magnetic resonance atlas of the healthy human brain. In: *NeuroImage* 43 (2008), Oktober, Nr. 1, S. 69--80

[129] Jones, Derek K.: The effect of gradient sampling schemes on measures derived from diffusion tensor MRI: a Monte Carlo study. In: *Magnetic resonance in medicine: official journal of the Society of Magnetic Resonance in Medicine / Society of Magnetic Resonance in Medicine* 51 (2004), April, Nr. 4, S. 807--815

[130] Müller, H-P ; Unrath, A ; Ludolph, A C. ; Kassubek, J: Preservation of diffusion tensor properties during spatial normalization by use of tensor imaging and fibre tracking on a normal brain database. In: *Physics in medicine and biology* 52 (2007), März, Nr. 6, S. N99--109

[131] Zhang, Hui ; Yushkevich, Paul A. ; Rueckert, Daniel ; Gee, James C.: A Computational White Matter Atlas for Aging with Surface-Based Representation of Fasciculi. In: Fischer, Bernd (Hrsg.) ; Dawant, Benoît M. (Hrsg.) ; Lorenz, Cristian (Hrsg.): *Biomedical Image Registration*. Springer Berlin Heidelberg, Januar 2010 (Lecture Notes in Computer Science 6204). -- ISBN 978--3--642--14365--6 978--3--642--14366--3, S. 83--90

[132] Liu, Zhexing ; Goodlett, Casey ; Gerig, Guido ; Styner, Martin: Evaluation of DTI Property Maps as Basis of DTI Atlas Building. In: *Proceedings - Society of Photo-Optical Instrumentation Engineers* 7623 (2010), März

[133] Powell, J.L. ; Parkes, L. ; Kemp, G.J. ; Sluming, V. ; Barrick, T.R. ; García-Fiñana, M.: The effect of sex and handedness on white matter anisotropy: a diffusion tensor magnetic resonance imaging study. In: *Neuroscience* 207 (2012), April, S. 227--242

[134] Lazar, Nicole: *The Statistical Analysis of Functional MRI Data*. Springer, 2008. -- ISBN 978--0--387--78191--4

[135] Porter, David A. ; Heidemann, Robin M.: High resolution diffusion-weighted imaging using readout-segmented echo-planar imaging, parallel imaging and a two-dimensional navigator-based reacquisition. In: *Magnetic Resonance in Medicine: Official Journal of the Society of Magnetic Resonance in Medicine / Society of Magnetic Resonance in Medicine* 62 (2009), August, Nr. 2, S. 468--475

[136] Notohamiprodjo, Mike ; Dietrich, Olaf ; Horger, Wihelm ; Horng, Annie ; Helck, Andreas D. ; Herrmann, Karin A. ; Reiser, Maximilian F. ; Glaser, Christian: Diffusion Tensor Imaging (DTI) of the Kidney at 3 Tesla–Feasibility, Protocol Evaluation and Comparison to 1.5 Tesla. In: *Investigative Radiology* 45 (2010), Mai, Nr. 5, S. 245--254

[137] Lagana, M ; Rovaris, M ; Ceccarelli, A ; Venturelli, C ; Marini, S ; Baselli, G: DTI Parameter Optimisation for Acquisition at 1.5T: SNR Analysis and Clinical Application. In: *Computational Intelligence and Neuroscience* 2010 (2010), Januar

[138] Kido, Aki ; Kataoka, Masako ; Yamamoto, Akira ; Nakamoto, Yuji ; Umeoka, Shigeaki ; Koyama, Takashi ; Maetani, Yoji ; Isoda, Hiroyuki ; Tamai, Ken ; Morisawa, Nobuko ; Saga, Tsuneo ; Mori, Susumu ; Togashi, Kaori: Diffusion tensor MRI of the kidney at 3.0 and 1.5 Tesla. In: *Acta radiologica (Stockholm, Sweden: 1987)* 51 (2010), November, Nr. 9, S. 1059--1063

[139] The MathWorks, Inc.: *Evaluating Goodness of Fit*. Version: 2016. `http://de.mathworks.com/help/curvefit/evaluating-goodness-of-fit.html?requestedDomain=se.mathworks.com`, Abruf: 05.10.2016

[140] Wittsack, Hans-Jörg ; Lanzman, Rotem S. ; Mathys, Christian ; Janssen, Hendrik ; Mödder, Ulrich ; Blondin, Dirk: Statistical evaluation of diffusion-weighted imaging of the human kidney. In: *Magnetic resonance in medicine: official journal of the Society of Magnetic Resonance in Medicine / Society of Magnetic Resonance in Medicine* 64 (2010), August, Nr. 2, S. 616--622

[141] Rosenkrantz, Andrew B. ; Sigmund, Eric E. ; Johnson, Glyn ; Babb, James S. ; Mussi, Thais C. ; Melamed, Jonathan ; Taneja, Samir S. ; Lee, Vivian S. ; Jensen, Jens H.: Prostate cancer: feasibility and preliminary experience of a diffusional kurtosis model for detection and assessment of aggressiveness of peripheral zone cancer. In: *Radiology* 264 (2012), Juli, Nr. 1, S. 126--135

[142] Yoshikawa, Takeshi ; Kawamitsu, Hideaki ; Mitchell, Donald G. ; Ohno, Yoshiharu ; Ku, Yonson ; Seo, Yasushi ; Fujii, Masahiko ; Sugimura, Kazuro: ADC measurement of abdominal organs and lesions using parallel imaging technique. In: *AJR. American journal of roentgenology* 187 (2006), Dezember, Nr. 6, S. 1521--1530

[143] Heusch, Philipp ; Wittsack, Hans-Jörg ; Kröpil, Patric ; Blondin, Dirk ; Quentin, Michael ; Klasen, Janina ; Pentang, Gael ; Antoch, Gerald ; Lanzman, Rotem S.: Impact of blood flow on diffusion coefficients of the human kidney: A time-resolved ECG-triggered diffusion-tensor imaging (DTI) study at 3T. In: *Journal of Magnetic Resonance Imaging* 37 (2013), Nr. 1, S. 233--236

[144] Tabesh, Ali ; Jensen, Jens H. ; Ardekani, Babak A. ; Helpern, Joseph A.: Erratum: Estimation of tensors and tensor-derived measures in diffusional kurtosis imaging. In: *Magnetic Resonance in Medicine* 65 (2011), Nr. 5, S. 1507--1507

[145] Jansen, J. F. A. ; Stambuk, H. E. ; Koutcher, J. A. ; Shukla-Dave, A.: Non-Gaussian Analysis of Diffusion-Weighted MR Imaging in Head and Neck Squamous Cell Carcinoma: A Feasibility Study. In: *American Journal of Neuroradiology* 31 (2010), Januar, Nr. 4, S. 741--748

[146] Grinberg, Farida ; Farrher, Ezequiel ; Kaffanke, Joachim ; Oros-Peusquens, Ana-Maria ; Shah, N. J.: Non-Gaussian diffusion in human brain tissue at high b-factors as examined by a combined diffusion kurtosis and biexponential diffusion tensor analysis. In: *NeuroImage* 57 (2011), August, Nr. 3, S. 1087--1102

[147] Lanzman, Rotem S. ; Ljimani, Alexandra ; Pentang, Gael ; Zgoura, Panagiota ; Zenginli, Hakan ; Kröpil, Patric ; Heusch, Philipp ; Schek, Julia ; Miese, Falk R. ; Blondin, Dirk ; Antoch, Gerald ; Wittsack, Hans-Jörg: Kidney Transplant: Functional Assessment with Diffusion-Tensor MR Imaging at 3T. In: *Radiology* 266 (2013), Januar, Nr. 1, S. 218--225

[148] Fukunaga, Issei ; Hori, Masaaki ; Masutani, Yoshitaka ; Hamasaki, Nozomi ; Sato, Shuji ; Suzuki, Yuriko ; Kumagai, Fumitaka ; Kosuge, Masatsugu ; Hoshito, Haruyoshi ; Kamagata, Koji ; Shimoji, Keigo ; Nakanishi, Atsushi ; Aoki, Shigeki ; Senoo, Atsushi: Effects of diffusional kurtosis imaging parameters on diffusion quantification. In: *Radiological Physics and Technology* 6 (2013), Juli, Nr. 2, S. 343--348

[149] Correia, Marta M. ; Carpenter, Thomas A. ; Williams, Guy B.: Looking for the optimal DTI acquisition scheme given a maximum scan time: are more b-values a waste of time? In: *Magnetic Resonance Imaging* 27 (2009), Februar, Nr. 2, S. 163--175

[150] Ni, H. ; Kavcic, V. ; Zhu, T. ; Ekholm, S. ; Zhong, J.: Effects of Number of Diffusion Gradient Directions on Derived Diffusion Tensor Imaging Indices in Human Brain. In: *American Journal of Neuroradiology* 27 (2006), Januar, Nr. 8, S. 1776--1781

[151] Chefd'hotel, C. ; Hermosillo, G. ; Faugeras, O.: A variational approach to multi-modal image matching. In: *IEEE Workshop on Variational and Level Set Methods in Computer Vision, 2001. Proceedings*, 2001, S. 21--28

[152] Hermosillo, Gerardo ; Chefd'Hotel, Christophe ; Faugeras, Olivier: Variational Methods for Multimodal Image Matching. In: *International Journal of Computer Vision* 50 (2002), Dezember, Nr. 3, S. 329--343

[153] Huang, Yanqi ; Chen, Xin ; Zhang, Zhongping ; Yan, Lifen ; Pan, Dan ; Liang, Changhong ; Liu, Zaiyi: MRI quantification of non-Gaussian water diffusion in normal human kidney: a diffusional kurtosis imaging study. In: *NMR in Biomedicine* 28 (2015), Nr. 2, S. 154--161

[154] Veraart, Jelle ; Poot, Dirk H. J. ; Van Hecke, Wim ; Blockx, Ines ; Linden, Annemie Van d. ; Verhoye, Marleen ; Sijbers, Jan: More accurate estimation of diffusion tensor parameters using diffusion kurtosis imaging. In: *Magnetic Resonance in Medicine* 65 (2011), Nr. 1, S. 138--145

[155] Quentin, Michael ; Pentang, Gael ; Schimmöller, Lars ; Kott, Olga ; Müller-Lutz, Anja ; Blondin, Dirk ; Arsov, Christian ; Hiester, Andreas ; Rabenalt, Robert ; Wittsack, Hans-Jörg: Feasibility of diffusional kurtosis tensor imaging in prostate MRI for the assessment of prostate cancer: preliminary results. In: *Magnetic Resonance Imaging* 32 (2014), September, Nr. 7, S. 880--885

[156] Raz, E. ; Bester, M. ; Sigmund, E. E. ; Tabesh, A. ; Babb, J. S. ; Jaggi, H. ; Helpern, J. ; Mitnick, R. J. ; Inglese, M.: A Better Characterization of Spinal Cord Damage in Multiple Sclerosis: A Diffusional Kurtosis Imaging Study. In: *American Journal of Neuroradiology* 34 (2013), September, Nr. 9, S. 1846--1852

[157] Zhang, Wei ; Ma, Xiaohui ; Wang, Yan ; Zhao, Jian ; Zhang, Xujing ; Gao, Yu ; Li, Shiling: Assessment of apparent diffusion coefficient in lumbar intervertebral disc degeneration. In: *European Spine Journal: Official Publication of the European Spine Society, the European*

Spinal Deformity Society, and the European Section of the Cervical Spine Research Society 23 (2014), September, Nr. 9, S. 1830--1836

[158] Sinkus, R. ; Lorenzen, J. ; Schrader, D. ; Lorenzen, M. ; Dargatz, M. ; Holz, D.: High-resolution tensor MR elastography for breast tumour detection. In: *Physics in Medicine and Biology* 45 (2000), Juni, Nr. 6, S. 1649